University of Naples Federico II
Polytechnic and Basic Sciences School

Department of Chemical Sciences

neapōlis

Ph.D. in Chemical Sciences

New "bio–inspired" devices: synthetic peroxidases for chemical and biotechnological applications

Gerardo Zambrano

Advisors:
prof. Vincenzo Pavone
dott. Ornella Maglio

Examiner:
prof. Angela Amoresano

This thesis was granted by Avantech Group s. r. l.

This page was intentionally left blank

Chapter 3: Synthetic peroxidases in electrochemistry and amperometric biosensors

Chapter 4: Synthetic peroxidases in bio-nanomaterals construction

Chapter 5: Conclusions

Chapter 6: Supplementary Materials

A: Absorbance
ABTS: 2,2'–azino–bis(3–ethylbenzthiazoline–6–sulphonic acid)
Ac: Acetyl
ACN: Acetonitrile
Aib:α–amino–isobutyrric acid
Arg: Arginine
Asn: Asparagine
Asp: Aspartic acid
AuNPs: Gold nanoparticles
CD: Circular dichroism
CDL: Curve Desolvation Line
CTM: c–type Cytochrome Maquette
CV: Cyclic Voltammetry
Cys: Cysteine
D: Decapeptide
DBQ: 2,6-dichlorobenzoquinone
DCM: Dichloromethane
DHP: Dehaloperoxidase
DIEA: Diisopropylethylamine
DMF: N,N–Dimethylformamide
DMSO: Dimethylsulfoxide
DPIX: Deuteroporphyrin IX
DPV: Differential pulse voltammetry
EDT: 1,2–Ethanedithiol
ESI–MS: Electrospray ionization mass spectrometry
Fmoc: 9–Fluorenylmethoxycarbonyl
GC–MS: Gas chromatography–mass spectrometry
GCE: Glassy carbon electrode
Gln: Glutamine
Glu: Glutamic acid
HATU: N–[(Dimethylamino)–1H–1,2,3–triazolo–[4,5–b] pyridin– 1–ylmethylene]–N–methylmethanaminium hexafluorophosphate N–oxide
HFIP: 1,1,1,3,3,3–Hexafluoro–2–propanol
His: Histidine
HOBt: N–hydroxybenzotriazole
HPs: Halophenols
HPLC: High Performance Liquid Chromatography
HRP: Horseradish peroxidase
ICP–MS: Inductively coupled plasma–mass spectrometry
Ile: Isoleucine
K_d: dissociation constant
K_m: Michaelis–Menten costant

Leu: Leucine
LOD: Limit of detection
Lys: Lysine
Mb: Myoglobin
MC: Mimochrome
Met: Methionine
Mmt: (4–methoxyphenyl)diphenylmethyl
MP: Microperoxidase
MTBE: Methyl–tert–butylether
Mtt: (4–methylphenyl)diphenylmethyl
NMP: N–Methyl–2–pyrrolidone
NMR: Nuclear magnetic resonance
Pbf: 2,2,4,6,7–Pentamethyldihydrobenzofuran–5–sulfonyl
PDB: Protein Data Bank
Pro: Proline
R_f: Retention factor
RP–HPLC: Reverse Phase – High Performance Liquid Chromatography
R_t: Retention time
RT: Room Temperature
Ser: Serine
T.O.N.: Turnover number
tBu: *tert*–butyl
TCE: 2,2,2–trichloroethanol
TCP: 2,4,6-trichlorophenol
TD: Tetradecapeptide
TFA: Trifluoroacetic acid
TFE: 2,2,2–trifluoroethanol
Thr: Threonine
TIS: Triisopropylsilane
TLC: Thin Layer Chromatography
Trt: Trityl
Tyr: Tyrosine

This page was intentionally left blank

Peroxidases are a large family of house–keeping enzymes expressed in all living kingdoms. These enzymes are involved in many life–sustaining processes that ensure homeostasis of intra– and extra–cellular environment. Among all, plant peroxidases are the most widely studied. They show common structural features such as a Fe^{3+}–protoporphyrin IX (heme) as prosthetic group. In the enzyme resting state, the iron ion is invariantly penta–coordinated: four ligands are provided by the porphyrin ring, while a His residue is coordinated as the fifth axial ligand (namely, the proximal His). The sixth coordination position is occupied by solvent. From a catalytic point of view, peroxidases are peroxide–activated enzymes that couple H_2O_2 decomposition with oxidation of an organic (phenols, anilines, organic sulfides, etc.) or inorganic substrate (chloride ions, etc.). The great functional versatility makes peroxidases very attractive for practical applications in chemistry, biotechnology and medicine. Among all peroxidases, the peroxidase from horseradish (HRP) is one of the most used reporter enzyme in enzyme linked immunosorbent assays (ELISA), electrochemical and optical biosensors.

The present PhD project, granted by Avantech Group s.r.l., is aimed to find and develop possible applications for synthetic peroxidases designed by a miniaturization approach. To this purpose, Fe(III)–Mimochrome VI*a (FeMC6*a) was used (Figure 1).
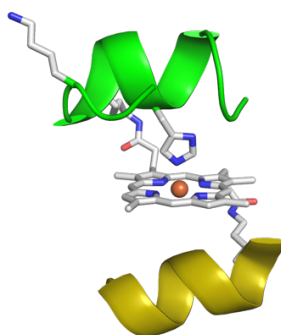
Figure 1. Model structure of FeMC6*a

Previous experiments, carried out on this synthetic peroxidase, demonstrated its higher performances under optimal conditions, compared to those of natural HRP, particularly in ABTS (a common chromogenic substrate used for peroxidases) oxidation.

The synthetic FeMC6*a is provided with high catalytic versatility and enhanced performances despite its miniaturized scaffold (3.5 kDa), which encouraged investigations for many practical applications.

In this project, FeMC6*a was successfully investigated in the fields of: *i)* bioremediation (chapter 2); *ii)* sensing (chapter 3); *iii)* bionanomaterials construction (chapter 4).

i) FeMC6*a proved to be an efficient catalyst in the transformation of several halophenols, and the catalytic characterization using 2,4,6–trichlorophenol as model substrate confirmed its remarkable activity in oxidative dehalogenation reactions. This function was used to lay the basis for a new bioremediation strategy based on synthetic peroxidases. in which FeMC6*a was able to deplete 2,4,6–trichlorophenol from solution in nanomolar catalyst concentrations.

ii) FeMC6*a was efficiently entrapped onto glassy carbon electrodes and the peculiarity of its redox behavior was exploited for the development of a synthetic peroxidase based halogenated alcohol sensor, in collaboration with Prof. Wing Cheung Mak from Linköping University. The sensing principle relies on the increase of catalytic currents upon addition of halogenated solvents.

iii) FeMC6*a was immobilized onto gold nanoparticles and the catalytic performances of the obtained nano–bioconjugate were evaluated. The immobilization was achieved by means of a bio–orthogonal approach.

Chapter 1

Natural and synthetic heme proteins

1.1 Introduction

1.1.1 Heme proteins in Nature

Nature uses metal ions to carry out a plethora of functions. Across evolution, Nature has developed and optimized metalloproteins, which hold and tune metal ions properties through interactions with the protein matrix. This is an extremely fine ability, allowing metalloproteins to play a pivotal role in fundamental biological functions, such as nitrogen fixation, photosynthesis, respiration, electron transfer, water oxidation, oxygen transport, storage and activation [R. Crichton (2019)]. Defined ligands composing the first coordination sphere, and their interactions (such as hydrogen bonds, hydrophobic and ionic) with the surrounding protein environment, the second coordination sphere, influence the properties of metal ions [O. Maglio et al. (2012)]. Altogether these interactions are crucial for the activity of metalloproteins, and functional diversities can be obtained by precise changes in the first and second coordination sphere [Y. Valasatava et al. (2018)].

Among metal cofactors, heme is one of the most represented in Nature [T. L. Poulos (2014)] and is involved in a wide variety of indispensable life–sustaining tasks [E. N. Mirts et al. (2018)]. Heme chemically refers to iron, usually in the +2 or +3 oxidation states, enclosed in the center of the porphyrin, an organic macrocycle. When embedded into different protein matrices, it shows diversity of functions, such as dioxygen transport in the case of hemoglobin, electron transfer for cytochrome b_5, and H_2O_2 and O_2–activated oxidative catalysis for horseradish peroxidase (HRP) and cytochrome P450, respectively (Figure 1.1).
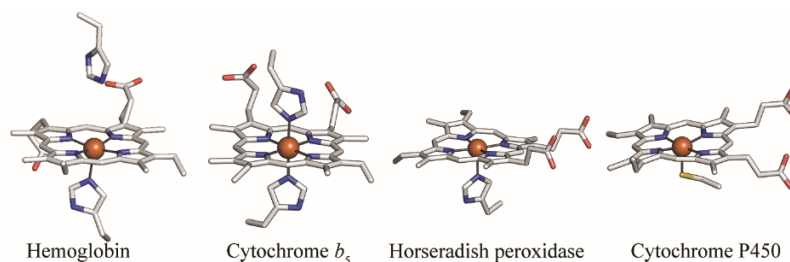
Figure 1.1. First coordination sphere of most common heme proteins in the resting state.

Different amino acids can serve as axial ligands to the heme. Histidine is the most common, but other residues such as methionine, cysteine and tyrosine can be found [J. Smith et al. (2010)]. The protein matrix can offer one or two extra–ligands to the heme. Penta–coordination is observed in globins and peroxidases, in which the protein scaffold provides only one histidine as the fifth strong axial ligand, while the sixth coordination position may contain a labile water molecule or is left empty to accommodate exogenous molecules. Among globins, Fe^{2+}–containing hemoglobin binds dioxygen with high affinity and transports it to tissues. In peroxidases, Fe^{3+}–heme is able to bind small organic substrates and oxidize them upon reaction with hydrogen peroxide. Another example of penta–coordination is found in cytochrome P450 in which a Fe^{2+}–heme is coordinated by a cysteine residue and is able to oxidize organic substrates by using dioxygen as electron acceptor [D. Werk–Reichart and R. Feyereisen (2000); J. Liu et al. (2014)]. Six–coordinated motifs are observed mainly as bis–histidine heme proteins, since two His residues bind the metal ion from the opposite faces of the porphyrin ring. This coordination geometry is found in electron transfer proteins (e.g. cytochrome b_5). Nonetheless, hexacoordinated heme with different axial ligands are also observed (e.g.cytochrome c_2) [H. L. Axelrod and M. Y. Okamura (2005)].

1.1.2 **Heme properties**

Although the tuning of metal ion properties mainly relies on the protein matrix, structural differences in the heme cofactor also play an important role [R. Vitale, PhD thesis].

As already mentioned, hemes are chemically referred to iron ion enclosed in the center of the porphyrin, in which four pyrrolic groups are linked together by methine bridges (Figure 1.2).
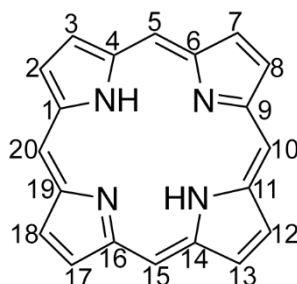
Figure 1.2. Chemical structure and numbering scheme, of the porphyrin macrocycle according to IUPAC nomenclature. The 2, 3, 7, 8, 12, 13, 17 and 18 positions are defined β positions, whereas 5, 10, 15 and 20 are *meso* positions.

Chemically, heme–proteins are classified in different subcategories depending on the structural features of the porphyrin macrocycle and how it is anchored to the protein matrix (Figure 1.3).
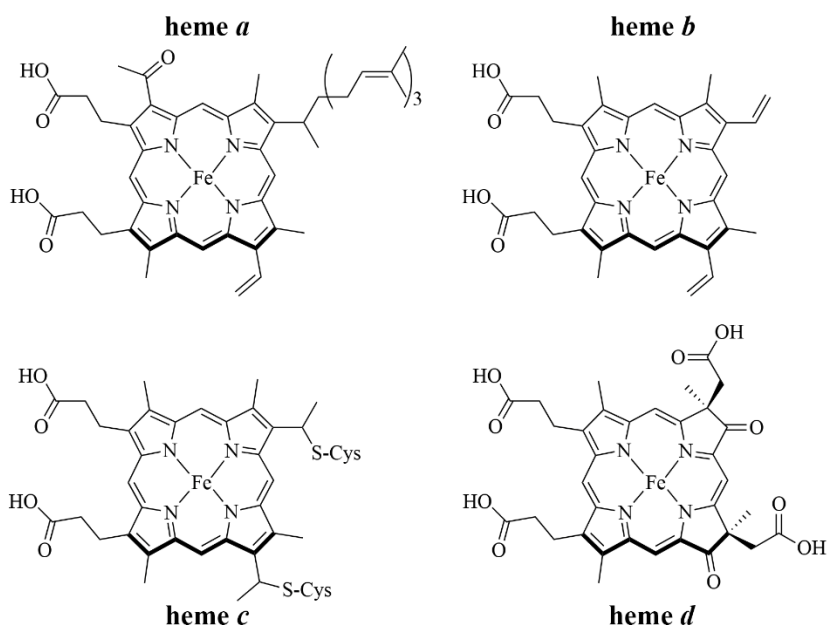
Figure 1.3. Chemical structures of naturally occurring heme *a*, *b*, *c* and *d*. Adapted from [C. J. Reedy and B. R. Gibney (2004)].

The most commonly found heme is iron (II/III) protoporphyrin IX, known as heme *b* or "protoheme". Structurally, it presents vinyl groups at positions 8 and 13, methyl groups at positions 3, 7, 12 and 17, and propionates at positions 2 and 18 of the macrocycle. Heme *b* is housed in the protein scaffold by non–covalent hydrophilic and hydrophobic interactions. More specifically, the coordinating residues to the iron ion ensure a tight binding of the cofactor while hydrophobic interactions with the heme macrocycle and polar interactions with the porphyrin propionic groups strengthen the binding [C. J. Reedy and B. R. Gibney (2004)].

Heme *c* is anchored to proteins via covalent bonds between cysteine residues and the heme vinyl groups. Heme *c* proteins usually contains a CXXCH sequence motif, as found in cytochromes *c* and *f*. In these proteins, the terminal thiol of the cysteine residues form thioether bonds to the porphyrin, while the histidine coordinates the iron [C. J. Reedy and B. R. Gibney (2004), S. E. Martinez et al. (1996)].

Heme *a* derives from heme *b* by conversion of the vinyl group at position 8 into a hydroxy–ethylfarnesyl group, followed by oxidation of the methyl at position 3 to formyl group. Heme *a* is more hydrophobic and more electron–withdrawing with respect to its precursor. It is found only in terminal oxidases, such as mammalian cytochrome *c* oxidase [C. J. Reedy and B. R. Gibney (2004), T. Mogi et al. (1994)].

Less common heme architectures include heme *d* [B. K. Vainshtein et al. (1986)], heme P–460 [N. Igarashi et al. (1997)] and siroheme [B. C. Tripathy et al. (2010)].

1.1.3 **Heme peroxidases**

Peroxidases belong to a large family of house–keeping enzymes expressed by prokariota, fungi, secretory plants and animals [M. Zamocky et al. (2008)]. These enzymes are involved in many life–sustaining processes that ensure homeostasis of intra– and extra–cellular environment. Indeed, in animals, heme peroxidases such as myeloperoxidase, salivary peroxidase (SPO) and thyroid peroxidase (TPO) are essential in host–defense mechanisms and hormone synthesis by producing hypohalous acids that are either used to neutralize pathogenic microorganisms and for iodination reactions in thyroidal hormone synthesis [S. J. Klebanoff (2005); G. Cheng et al. (2008); A. A. Khan et al. (2014)]. In plants, heme peroxidases play a pivotal role in the lignification process [A. R. Barceló and F. Pomer (2001)], wound healing [S. D. Allison and J. Schultz (2004)], suberization [M. A. Bernards et al. (1999)], reactive oxygen species (ROS) and reactive nitrogen species (RNS) metabolism [A. Liszkay et al. (2003); S. M. Mc Innis et al. (2006)].

All plant peroxidases show common structural features such as a Fe^{3+}– protoporphyrin IX as the prosthetic group and a His on the proximal site [S. S. Sibbett and J. K. Hurst (1984)]. In the enzyme resting state, the iron ion is

invariantly penta–coordinated: four ligands are provided by the porphyrin (four nitrogen of the heme in equatorial positions), whereas His is coordinated as the fifth axial ligand (namely, the proximal His) [A. M. Azevedo et al. (2004)]. The sixth coordination position is occupied by a solvent molecule, thus iron is in a high spin state (S = 5/2).

From a catalytic point of view, peroxidases are peroxide–dependent enzymes that couple H_2O_2 decomposition with oxidation of an organic or inorganic substrate. Common substrates for these enzymes are aromatic compounds (amine, phenols, organic sulfides) which are converted either into their oxidized forms or polymers, and inorganic anions (mainly chloride and bromide) are converted into hypohalous acids. Peroxidases are very attractive for practical applications in chemistry, biotechnology and medicine, thanks to their great versatility, and to their production capacity in large amounts at competitive costs. Among all peroxidases, the peroxidase from horseradish is one of the most used reporter enzyme in ELISA, electrochemical and optical biosensors [A. M. Azevedo et al. (2004)].

1.1.4 **Peroxidase from horseradish**

The peroxidase from horseradish (HRP), produced by *Armoracia rusticana* belongs to a large family of different isoenzymes, which differ slightly in amino acid sequences and glycosylation.
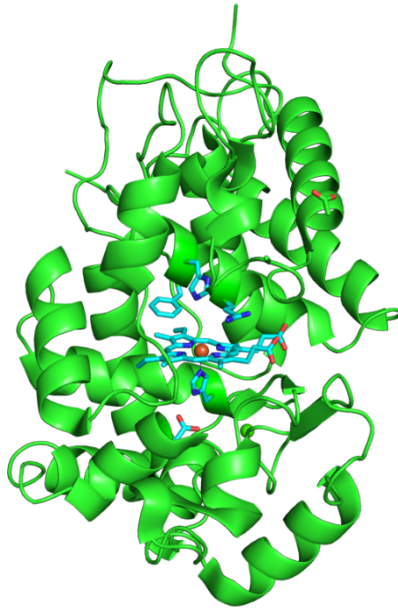
Figure 1.4. X–ray structure of HRP C1A (PDB ID: 1ATJ).

In 1954, it was already known that the *Armoracia rusticana* root extract was composed by several isoforms of HRP [Jeremyn, M. A. and Thomas, R. (1954)]. By ion exchange chromatography onto carboxymethyl cellulose, Paul identified five different forms of HRP (A, B, C, D and E) [Paul, K. G. (1958)]. Further purifications by Aibara and Shannon, made possible to isolate HRP as three acidic fractions (A1–3), five neutral fractions (B1–3, C1–2) and six basic fractions (E1–6) [Aibara, S. et al. (1981); Shannon, L. M. et al. (1996)]. Among all isoenzymes, isoenzyme C (HRP C) is the most abundant (Figure 1.4) [Krainer, F. W. and Glieder, A. (2015).].

HRP C comprises a single polypeptide chain of 308 amino acid residues, with the N–terminal blocked by pyroglutamate and a heterogeneous C–terminus [Krainer, F. W. and Glieder, A. (2015)].

In the sequence, nine potential N–glycosylation sites can be recognized with N–X–S/T motif and of these, eight are usually occupied. HRP C is variably

glycosylated and the carbohydrate content varies between 18 and 22% on the molecular weight [Veitch, N. C. (2004)].

Glycan composition is instead very well conserved and comprises a heptasaccharide chain represented in Figure 1.5.

Man(α1→6)

Man(α1→3) ——— Man(β1→4)GlcNAc(α1→6)GlcNAc(α1→N)Asn

Man(β1→2)

Fuc(α1→3)
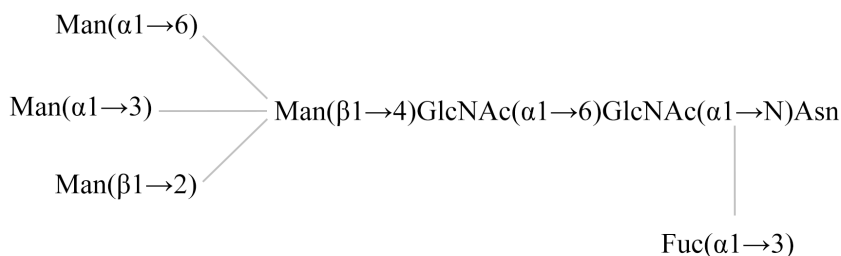
Figure 1.5. Glycan structure found in HRP C1A

HRP C tertiary structure is composed by 13 α–helices and three β–sheets. Structural details around the heme are reported in Figure 1.6. The heme *b* is housed in a heme binding pocket comprising phenylalanine residues (Phe41 and Phe221) for hydrophobic interactions and polar residues such as Gln176, Ser73, Ser 35 and Arg31 which create a hydrogen–bonding network to the propionate groups of the heme, thus reinforcing the binding. Protein conformation is stabilized by four disulfide bonds (Cys 11–91, Cys 44–49, Cys 97–301, and Cys 177–209) and 2 calcium ions, indispensable for correct folding [K. G. Welinder (1976)].

The N_{ε} of His170 (proximal His) directly coordinates the iron on the proximal face of the heme *b*, whether the second axial coordination position on the heme distal side is unoccupied and represents the hydrogen peroxide binding site during catalysis (Figure 1.7) [Poulos, T. L. and Kraut, J. (1980)].
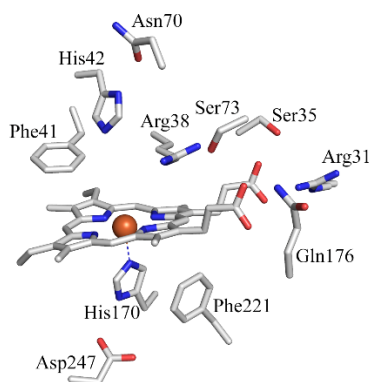
Figure 1.6. Three–dimensional representation of the residues interacting with the heme *b* of HRP C1A.

HRP C and other horseradish peroxidase isoenzymes reactions can be expressed by the scheme depicted below (Figure 1.7).

$$2AH + H_2O_2 \xrightarrow{\quad HRP \quad} 2A^\bullet + 2H_2O$$

Figure 1.7. Substrate oxidation catalyzed by HRP

HRP converts the substrate "AH" (such as phenols, anilines, organic thiols and thioethers) to its 1–electron deficient form while hydrogen peroxide is converted to water.

The catalysis occurs in a three–step process, in which the enzyme is first oxidized by H_2O_2 to high valent oxoferryl species (Compound I; $Fe^{4+}=O^{+\bullet}$) and then reduced back to the resting state (Fe^{3+}) by two sequential single–electron steps, passing through Compound II intermediate ($Fe^{4+}=O$) (Figure 1.8) [Veitch, N. C. and Smith, A. T. (2000)].
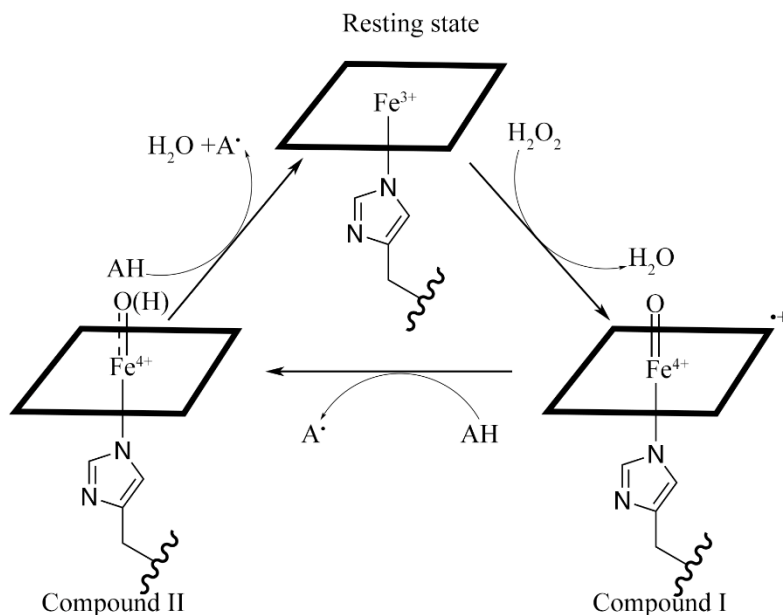
Figure 1.8. Catalytic cycle of HRP

The first step consists in the cleavage of the peroxide bond with the simultaneous release of water. The iron center catalyzes this reaction by providing two electrons to the oxygens. The reaction with H_2O_2 yields a 2–electron deficient heme cofactor, namely Compound I, which contains an oxoferryl group, with the iron in the +4 oxidation state, and a porphyrin in π–radical cation.

Compound–I is able to oxidize a wide range of reducing substrates. By a single–electron transfer mechanism, the compound I π–radical cation is reduced, leading the second enzyme intermediate, called Compound II. This still contains an oxoferryl group and the iron in the +4 oxidation state. A second oxidation reaction, provides the cofactor with a second electron, thus restoring the enzyme in its resting state ferric (+3). During these double one–electron reductions, the oxygen accepts two protons to form water molecules.

The presence of a strong hydrogen bond between the N_δ atom of the proximal histidine and an aspartate side chain (Asp247) represents a key factor in the modulation of redox potential of the penta–coordinated complex. This hydrogen bond increases the basicity of the coordinating histidine, stabilizing the high oxidation state of the intermediates, such as the high valent oxoferryl center [J. Everse, (1998)].

The binding of H_2O_2 occurs in the distal site, which is characterized by the presence of Arg38, Phe41 and His42 (Figure 1.9a). Two of these amino acids (Arg38 and His42) are invariantly found in all plant peroxidases and play a role in the acid–base catalytic cleavage of the O–O bond (Figure 1.9b).
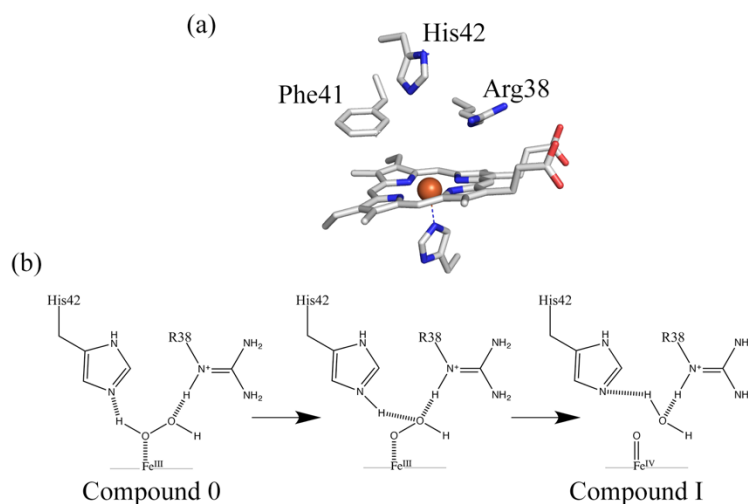
Figure 1.9. Distal site and role of His42 and Arg38 in H_2O_2 deprotonation and Compound I formation.

His42 in the distal site acts mainly as a general acid–base catalyst: it assists the hydrogen peroxide deprotonation and the subsequent heterolytic cleavage of the peroxide bond during Compound I formation [Rodríguez–López, J. N. et al. (1996)]. Distal Arg38 is involved in charge stabilization, mediated by its positively charged guanidinium group. Furthermore, once the O–O bond is

cleaved, Arg contributes to stabilize the oxoferryl species via hydrogen bond formation [Savenkova, M. I. et al. (1998)].

Site specific mutation of His42 residue with non–polar residues such as Ala (H42A), Leu (H42L) and Val (H42V) yields to drastic loss of activity due to reduction in compound I formation rate (from 1 to 5 order of magnitude) [Rodríguez–López, J. N. et al. (1996)]. A partial loss of activity is also observed when mutating Arg38 residue [Newmyer, S. L. and Ortiz de Motellano P. R. (1995); Rodríguez–López, J. N. et al. (1996); Veitch, N. C. and Smith, A. T. (2001)].

1.1.5 **Applications of peroxidases**

The versatility of HRP allows for its application as active sensing component in commercial devices. In particular, HRP is the most widely used peroxidase for analytical purposes [Gajhede, M. et al (1997)], and finds application in the development of biosensors [Sekretaryova, A. N. et al. (2016); Nakamura, H. and Karube, I. (2003)] and diagnostics [Azevedo, A. M. et al. (2003)]. The ability of HRP to reduce H_2O_2 and organic peroxides is exploited in biosensors for peroxides detection [Schubert, F. et al. (1991); El Kaoutit, M. et al. (2008)]. HRP based biosensors can be used to control and monitor peroxides in pharmaceutical industries, in bleaching operations, in the texile and paper industries and in food products [Azevedo, A. M. et al. (2003)]. Also, HRP can be directly wired onto electrodes. The enzyme, upon reaction with H_2O_2, yields a 2–electron deficient intermediate, which, in the absence of a reducing substrate, can be brought back to the resting state by suppling electrons from the electrode surface, thus restoring the native enzyme without the need of any mediator (figure 1.10).
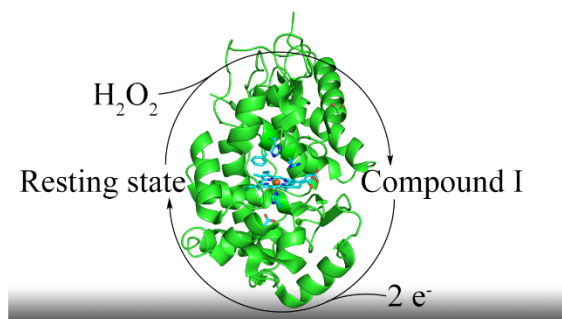
Figure 1.10. Mechanism of direct electroenzymatic reduction of a peroxide molecule at HRP - modified electrode.

When HRP–modified electrode, operated at a sufficiently negative potential, is placed in a peroxide containing solution, a reduction current proportional to the peroxide concentration is observed [Ahammad, A. J. S. (2012)].

Furthermore, if HRP is coupled with a hydrogen peroxide producing oxidase, the system becomes sensitive to the oxidase substrate, enabling the control and monitoring of a wide range of analytes such as glucose, ethanol, cholesterol (depending on the oxidase specificity). The main advantage of the combination with peroxidases is the low operating potential at which the oxidized mediator is reduced, avoiding undesirable reduction or oxidation of electroactive interferents (Figure 1.11) [Wilson, R. and Turner, A. P. F. (1992)]. Glucose sensors based on this mechanism have been widely reported in literature. A recent example is provided by [Yang, H. et al. (2017)], in which glucose oxidase and HRP were immobilized with carbon nanotubes onto a glassy carbon electrode. The proposed sensor is linear over the 0.022-7.0 mM range, with a sensitivity of 5.14 μA mM^{-1} cm^{-2}. In another example, glucose oxidase and HRP were immobilized by dispersion in a carbon paste material, together with ferrocene acting as mediator for HRP. The whole membrane was coated with Nafion, which entrapped and prevented losses of the immobilized proteins [Blanco-López, M.

C. et al. (2020)]. This sensor was able to measure glucose in food beverages. Furthermore, the high sensitivity of the bienzymatic glucose oxidase-HRP system allowed for miniaturization and use of cheap substrates, thus increasing the attractivity of these systems for commercial purposes, as reported by [Amor-Gutiérrez, O. et al. (2020)].
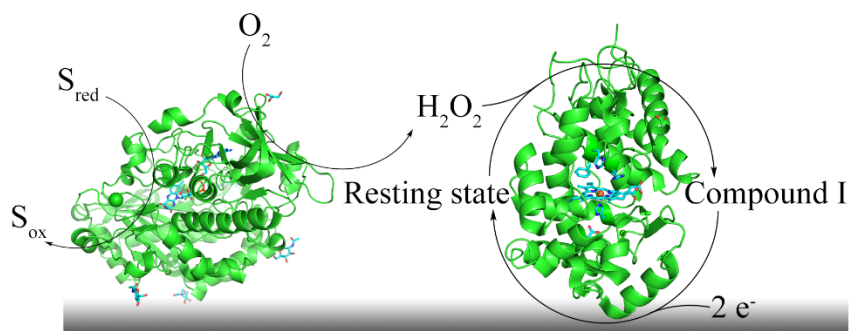
Figure 1.11. General scheme of a bi–enzymatic electrochemical biosensor.

HRP is also widely used as enzyme label in histochemical stainings and diagnostic assays. It is well suited for the preparation of enzyme–conjugated antibodies and antigens in immunoassays, such as enzyme linked immunosorbent assays (ELISA) (Fig. 1.12), due to its good stability and especially for its ability to yield chromomeric products with high turnover number [Azevedo, A. M. et al. (2003); Hermanson, G. T. (2008)]. ELISA represents nowadays the most routinely used immunochemical assay in the diagnostic field, for the detection of different compounds of both natural and synthetic origin.
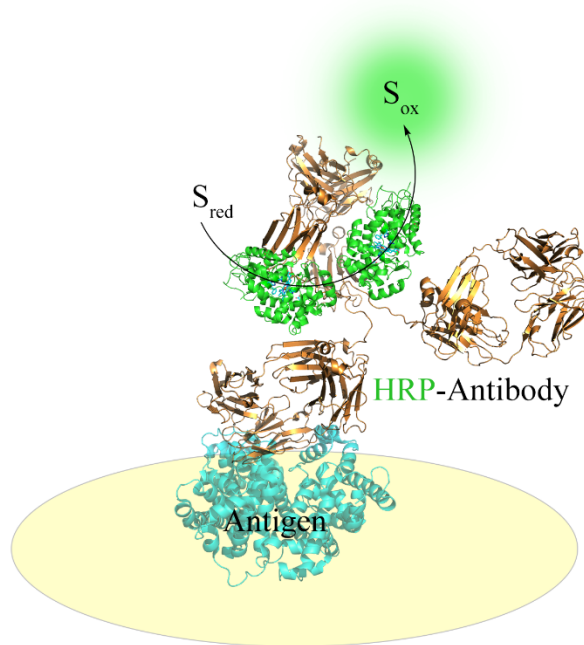
Figure 1.12. Representation of direct ELISA assay

Commercially available HRP–conjugates are characterized by a ratio of one to three HRP molecules per antibody molecule. This value is mainly due to steric hindrance of HRP during the conjugation reactions and represents the limit for maintaining functionality of the conjugate. Immunochemical assays research field is still widely expanding, in order to increase sensitivity of the responses for already existing assays and face the new coming requests for the development of new assays. ELISA assay works as a powerful tool to detect not only biological entities, but also small molecules in complex matrices, as reported for an ELISA assay targeting enrofloxacin (a fluoroquinolone which acts as a urinary antiseptic) with extremely low interference from other fluoroquinolone analogues [Watanabe, H. et al. (2000)]. Recently, a nanobody-HRP fusion protein was reported as ultrasensitive probe against Newcastle desease virus [Sheng, Y. et al. (2019)]. The proposed approach allows to

produce HRP-conjugated antibodies in a straightforward manner, reducing time and cost for antibody production. Analogously to HRP-ELISA, recent approaches profit of DNAzymes-aptasensor for the detection of antigens, as recently reported for a HRP-mimiking DNAzymes for breast cancer-derived exosomes [Zhou, Y. et al. (2020)].

Less diffused, but still noteworthy applications of HRP comprise dye bleaching, phenol degradation and polymer synthesis.

Downstream wastewaters from the textile and paper/printing industry often contain large amounts of colored organic molecules. They have synthetic origin and have capacity to act as xenobiotics for plants and animals causing environmental pollution [Husain, Q. and Fahad Ullah, M. (2019)]. Peroxidases are able to oxidize dyes leading to bleaching, polymerization, or degradation, facilitating downstream treatments [Matto, M. and Husain, Q. (2009); Ali, M. et al. (2016); Ali, M. et al. (2017); Ali, M. et al. (2018)]. Strategies involving HRP as treating enzyme have been proposed. The outstanding versatility of HRP in dye bleaching has been recently reported [Husain, Q. and Fahad Ullah, M. (2019)]. HRP proved to be capable of degrading dyes of different nature both in freely–diffusing and immobilized state, such as bromophenol blue [Liu, J. Z. et al. (2006)], direct yellow–11, methyl orange, crystal violet II [Maki, F. et al. (2006)] and many azo–dyes [Arslan, M. (2011)].

Textiles industries, together with wood industry, use and discharge in the environment large amounts of phenolic compounds. These substances contaminate waters and because of their resistance to biodegradation, they accumulate in the environment. This gave rise to concerns for human health because of toxicity and suspected of carcinogenicity [Xu, T. et al. (2014); Li, Z. et al. (2015); Fernandez Freire, P. et al. (2005); Huff, J. (2012)]. Catalytic investigation over the activity of HRP towards different phenols shows that the enzyme is able to convert phenols at low substrate concentration, but with

limited efficiency [Zhao, J. et al., (2015)]. Moreover, in the case of phenol and low monosubstituted phenols, HRP is able to trigger polymerization reactions with the formation of products with low solubility [Vasudevan, P. T. and Li, L. O. (1996)]. This last feature is particularly important as polymerized phenols can be then removed by simple filtration. Further details over HRP–based phenols bioremediation will be given in Chapter 2.

HRP has been lately proposed as an efficient catalyst for synthesis of conductive polymers. In the field of organic electronics and conductive polymer based biosensors, materials with high conductivity are often required to enhance responses and obtain systems with high sensitivity [Meng, L. et al, (2018)]. HRP has been used to synthesize a variety of polymers such as polypyrrole [Cruz– Silva, R. et al. (2008)], polyaniline [Rumbau, V. and Marcilla, R. et al. (2006)] and polyethylenedioxythiophene (PEDOT) [Rumbau, V. and Pomposo, A. et al. (2006)]. In this last example, HRP has been used as catalyst for the synthesis of PEDOT over 16 h reaction with EDOT monomer and hydrogen peroxide. The produced PEDOT did not require post–processing steps to increase conductivity, as usually done for the polymer synthesized with conventional protocols. The new synthetic protocol allowed to obtain PEDOT with high conductivity due to the high content of bipolarons in the polymer chains.

1.1.6 **Towards synthetic peroxidases**

The wide range of applicability of heme proteins and in particular peroxidases, have encouraged scientists to reproduce these enzymes in nature–derived and synthetic models with the aim to improve performances or install new functions compared to their natural counterparts. [Nastri, F. et al. (2019); Chino, M. et al. (2018); Nastri, F. et al. (2016); Yu, F. et al. (2014); Zastrow, M. L. et al. (2013); Mocny, C. S. et al. (2015); Grayson, K. J. et al. (2018); Bhagi-Damodaran, A. et al. (2016); Petrick, I. D. et al. (2014); Lin, Y.-W. et al. (2017); Lewis, J. C. et al.

(2013); Jeschek, M. et al. (2016); Hyster, T. K. et al. (2016); Schwizer, F. et al. (2018); Oohora, K. et al. (2019)].

The extensive investigation on natural proteins have provided bioinorganic chemists with many tools for developing peptide/protein based artificial systems, which represent a benchmark for understanding the structural-functional relationships in heme proteins.

These systems can be not only capable of simulating and even overcoming the features of natural heme proteins but also help in clarifying the mechanism that allows protein matrix to modulate the catalytic activity of the heme [Chino, M. et al. (2018); Yu, F. et al. (2014); Schwizer, F. et al. (2018); Friedle, S. et al. (2011); Lichtenstein, B. R. et al. (2012); Oloo, W. N. et al. (2013); Lewis, J. C. (2013); Lee, S. C. (2014); Oloo, W. N. et al. (2013); Chino, M. et al. (2015); Caserta, G. et al. (2015); Itoh, S. (2015); Bhagi–Damodaran, A. et al. (2017); Bren, K. L. (2017); Reig, A. J. et al. (2012); Zastrow, M.L. and Pecoraro, V.L. (2013); Grayson, K. J. and Anderson, J. R. (2018); Mocny, C. S. and Pecoraro, V. L. (2015); Lombardi, A. et al. (2019); Nastri, F. et al. (2016); Lin, Y.–W. (2017); Petrik, I. D. et al. (2014); Dürrenberger, M. and Ward, T. R. (2014); Hyster, T. K. and Ward, T. R. (2016); Yu, Y. et al. (2018); Jeschek, M. et al. (2018); Schwizer, F. et al. (2018); Oohora, K. et al. (2019)].

Although many ground–points in reproducing metalloenzyme activity in artificial systems are very–well established, satisfying all requirements simultaneously is often non trivial. Indeed, one of the most difficult requirement to comply relies in the delicate balance between the protein conformational stability and the flexibility of the metal ion site. The exchange of substrates and products often requires flexibility within the active site, while the metal ion requires the fulfillment of its coordination demands in all catalysis steps [Nastri, F. et al. (2019)].

Several strategies have been employed to construct peptide/protein–based artificial metalloenzymes, such as *de novo* design [Yu, F. et al. (2014); Zastrow, M. L. and Pecoraro, V. L. (2013); Grayson, K.J. and Anderson, J. R. (2018); Mocny, C. S. and Pecoraro, V. L. (2015); Lombardi, A. et al. (2019); Nastri, F. et al. (2016)], design through miniaturization processes [Chino, M. et al. (2018); Nastri, F. et al. (2016)]. and protein redesign of native scaffold [Chino, M. et al. (2018); Petrik, I. D. et al. (2014). In addition, supramolecular metalloprotein design and directed evolution have been used to develop artificial metalloproteins [Churchfield, L. A. et al. (2019); Arnold, F. H. et al. (2018)].

Using computational tools, *de novo* design allows to build polypeptide sequences, unrelated to any natural protein. These sequences fold into a well-defined three-dimensional structure and are able to incorporate a metal cofactor into a precise geometry, allowing to reproduce natural metal binding sites within artificial systems [Lombardi, A. et al. (2019)]. Also, *de novo* designed sequences allow to introduce non-natural metal binding sites into protein scaffolds, installing new functions, unknown to natural systems [Roy, A. et al. (2014); Zhang, S.-Q. et al. (2018); Koebke, K. J. et al. (2018), Chino, M. et al. (2018); Lin, Y.-W. et al. (2019)]. In this frame, Zhang and coworkers reported the design of homotetrameric four-helix bundles that bind tetranuclear clusters, consisting of four Zn^{2+} and four carboxylate oxygens tetra-clusters [Zhang, S.-Q. et al. (2018)]. The crystal structures of the helical proteins were in good agreement with the overall design, with the Zn^{2+} ions and the carboxylate oxygens situated at the vertices of a distorted cube-like structure. Furthermore, the metal ion clusters are assembled in a vast hydrogen-bonded network of 16 polar amino acids, all involved in predetermined metal ion-ligand and hydrogen-bonded interactions.

Design by miniaturization also represents a powerful tool to rationally design functional artificial metalloenzymes, starting from the structure of natural

proteins. Miniaturization allows to build the minimal peptide sequence, which contains sufficient information for proper folding and for an accurate reconstruction of the active site structure [Lombardi, A. et al. (2000); Xing, G. et al. (2001)]. In this field, Mimochromes represent a great example of heme-enzymes afforded by miniaturization. Further details over mimochromes activity and evolution is provided in Paragraph 1.1.7.

The functional properties of natural metalloproteins can be enhanced or repurposed through protein redesign [Nastri, F. et al. (2019); Lin, Y.-W. et al. (2017); Yin, L. et al. (2018); Mirts, E. N. et al. (2018)]. By this approach, carefully chosen scaffolds are mutated to obtain new metal binding sites. This strategy has been also employed to insert catalytically competent metal cofactors within natural protein scaffolds, thus yielding hybrid catalysts [Schwizer, F. et al. (2018); Liang, A. D. et al. (2019)].

An example of repurposing the function of a native enzyme in a rationally designed metalloprotein is provided by Yin and coworkers that created an effective artificial dehaloperoxidase (DHP) [Yin, L. et al. (2018)]. They combined the structural features of chloroperoxidase (a distal Asp) with DHP (a distal Tyr) in the same heme active center of Myoglobin (Mb). The rationally designed metalloprotein F43Y/H64D Mb efficiently carried out oxidative dehalogenation of 2,4,6-trichlorophenol, with a catalytic efficiency 1000-fold higher than that of native dehaloperoxidase (See Chapter 2, Paragraph. 2.1.2).

Beyond modification of the protein matrix, the activity of metalloprotein can be tuned and/or repurposed by incorporating or modifying the metal cofactor within a protein scaffold. [Davis, H. J. and Ward, T. R. (2019); Natoli, S. N. and Hartwig, J. F. (2019); Oohora, K. et al. 2019]

In the fiels of hemoproteins the alteration of natural cofactor to achieve novel reactivity has been utilized by Hayashi and coworkers. Through this approach, Hayashi et al. were successful in endowing Mb with new functions, by

introducing different aryl substituents on the propionate groups of protoheme IX, thus giving the unnatural cofactor [Hayashi T. et al. (1999); Hayashi, T. and Hisaeda, Y. (2002)] or by replacing the heme cofactor with the the iron porphycene in HRP and Mb, originating rHRP and rMb [Hayashi, T. et al. (2002)]; Oohora, K. et al. (2017); Matsuo, T. et al. (2007)].

Catalytic evaluation over the reconstituted enzymes confirmed that cofactor substitution caused a 10-fold increase in performances for rHRP in thioanisole oxidation and made Mb catalytically competent in cyclopropanation reactions.

Groundbreaking results have been obtained by non–covalent incorporation of metal cofactors into non–metal containing proteins [Kariyawasam, K. et al. (2019); Heinisch, T. and T. R. Ward (2016)]. Contributions in this field were provided by Mahy's group through the "Trojan horse" strategy. This strategy involves the introduction of metalloporphyrins into chiral environments, thus allowing for enantioselective catalysis. Remarkable results were obtained using antibodies as protein scaffold [Raffy, Q. et al. (2010)]. Furthermore, by raising antibodies against metalloporphyrins and microperoxidases, the same group developed "hemoabzymes", which bound Fe^{3+}–*meso*–tetrakis–*ortho*–carboxyphenyl porphyrin (FeT*o*CCP) with nanomolar K_d. The investigation over the catalytic performances of these antibody–metalloporphyrin complexes confirmed a 5–fold enhancement of catalytic efficiency in ABTS oxidation compared to free FeT*o*CCP [Ricoux, R. et al. (2002); Mahy, J. –P. et al. (2015)].

In contrast, among covalent heme conjugates, microperoxidases (MPs) confirm that peroxidase activity can be retained within extremely simplified scaffold. MPs are a class of covalent peptide–porphyrin systems, obtained by proteolytic digestion of cytochromes *c* [Marques, H. M. (2007)]. They consist of a short 6– to 11–mer peptide chain, covalently bound to heme *c* through two Cys residues of a Cys–Xxx–Xxx– Cys motif and are characterized by a mono–His coordination.
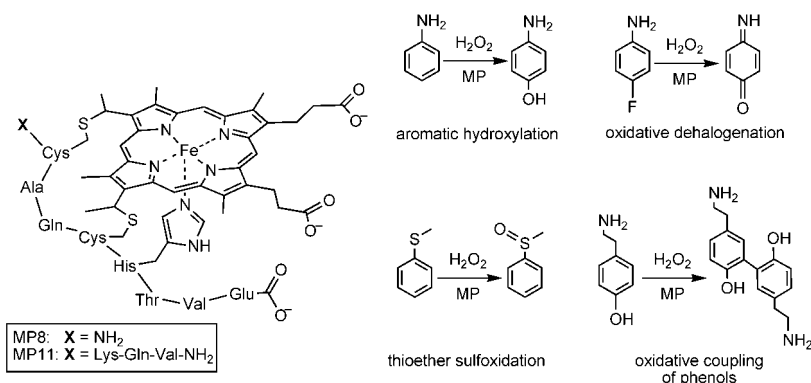
Figure 1.13. MPs structures and functions. Reproduced with permission from [Chino, M. et al. (2018)]

MPs fulfill the basic requirement for the first coordination sphere interactions through the His residue, acting as an axial ligand to the heme iron (Figure 1.13). The extremely reduced scaffold originates an open distal site.

Indeed, several MPs catalyze common oxidation and oxygenation reactions, such as aromatic hydroxylation, oxidative dehalogenation, thioether sulfoxidation and the oxidative coupling of phenolic substrates [Boersma, M. G. et al. (2000); Kadnikova, E. N. et al. (2003); Dallacosta, C. et al. (2004)]. However, all MPs suffer of prompt heme bleaching. Accessibility of the distal site determines degradation of the porphyrin ring during catalysis, thus limiting any practical application of these catalysts [Chino, M. et al. (2018)].

A possible solution to this issue, is the MPs immobilization in solid matrices, that could preserve maximal enzymatic activity, *i.e.* maximal loading and minimal leaching, while not hindering the diffusion of reactants/products to and from the enzyme's active site [Gkaniatsou, E. et al. (2019)]. In particular, considering the relatively small size, the pore inclusion of MPs into Metal-Organic Frameworks appeared to be more adequate compared to other immobilization methods that have been widely investigated for decades. Several groups have immobilized MP8 or MP11 into MOFs to develop efficient

biocatalysts. This strategy led to MP11- or MP8@MOF hybrid materials that displayed good activit, with remarkable recyclability due to the stabilization of the MPs inside the MOF cavities [Gkaniatsou, E. et al. (2019)]. An example is the work reported by Mahy and co-workers [Gkaniatsou, E. et al. (2018)] that immobilized MP-8 within the mesopores (2.9 and 3.4 nm in diameter) of an ultra-stable MOF MIL-101(Cr). Susprisingly, upon immobilization MP8 retained a full catalytic activity and showed an enhanced resistance to acidic and oxidative conditions.

1.1.7 **Mimochromes**

Through a process of miniaturization the Artificial Metallo–Enzymes group (AMEG), Naples, where this work was carried out, has developed a whole class of heme protein models named Mimochromes. The first model, Mimochrome I is constituted by two identical nonapeptides covalently linked to the propionic groups of the deuteroporphyrin IX through the ε–amino group of lysine residues. Taking into account the F–helix of hemoglobin β–chain, a nine–residue sequence was identified as the smallest sequence, required for a complete coating of one face of the heme. In the center, this sequence contained a histidine residue able to coordinate the iron. As each peptide bears a histidine axial ligand to the heme iron, Mimochrome I shows a bis–His coordination with a helix–heme–helix sandwiched structure. Hydrophobic residues were placed facing the porphyrin to tighten the interaction between the peptide and the cofactor. Finally, deuteroporphyrin was preferred over the common protoporphyrin IX to avoid the possibility of degradation of the sensitive vinyl groups during the synthesis [Nastri, F. et al. (1997)]. CD and NMR characterization of this first model revealed that the overall structure conformed well to the design, however, in solution, two diastereomers (Δ and Λ) were found. The flexibility of the linker between the peptide and the deuteroporphyrin

ring allowed each peptide chain to be positioned either above or below the porphyrin plane. Starting from Mimochrome I, structural optimization led to a new bis–His heme protein model, Mimochrome IV, in which, with respect to its predecessor, inter–helical interactions were introduced (Figure 1.14) [Lombardi, A. et al. (2003); Di Costanzo, L. et al. (2004)].
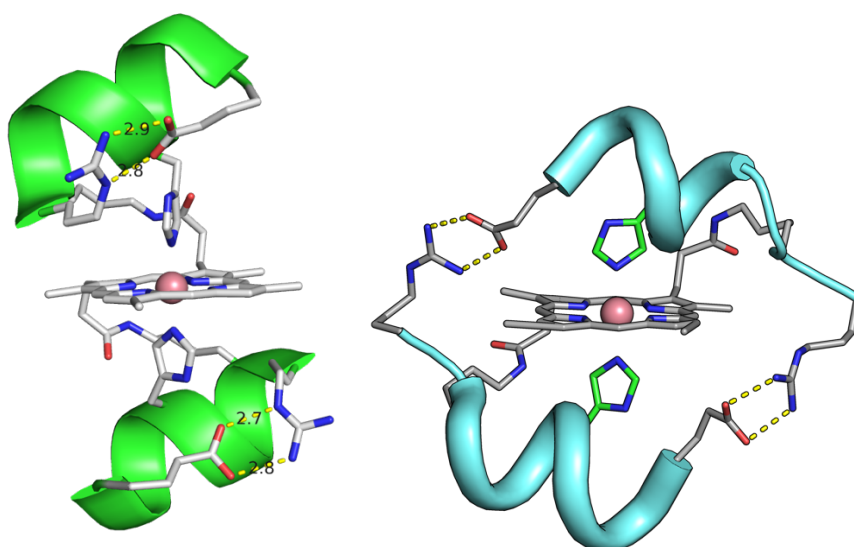
Figure 1.14. Co^{3+}–MC4 X–ray structure (PDB ID: 1PYZ,) (left) and NMR structure (PDB ID: 1VL3,) (right)

Interestingly, a unique diastereoisomer was stabilized. Both solution NMR and X–ray structures of Co^{3+}–MC4 showed the presence of the Λ isomer as a unique form [Di Costanzo, L. et al. (2004)].

In the frame of obtaining catalytically active heme protein models, starting from the bis–His structurally defined Mimochrome IV several rounds of redesign allowed shaping both the primary and secondary coordination spheres for functions (Figure 1.15).

The first round of redesign afforded the first catalytically active model, Mimochrome VI (MC6). MC6 comprises a tetradecapeptide (TD) bearing a His residue as axial ligand and a decapeptide (D), lacking of the coordinating residue and creating a substrate–binding pocket (Figure 1.15B) [Nastri, F. et al. (2011)].

MC4	Ac-E-S-Q-L-H-S-N-K-R-NH$_2$	
MC6	Ac-D-E-Q-Q-L-H-S-Q-K-R-K-I-T-L-NH$_2$ Ac-D-E-Q-Q-L-S-S-Q-R-K-NH$_2$	(TD) chain (D) chain
MC6*	Ac-D-L-Q-Q-L-H-S-Q-K-R-K-I-T-L-NH$_2$ Ac-D-E-Q-Q-L-S-S-Q-R-K-NH$_2$	(TD) chain (D) chain
MC6*a	Ac-D-L-Q-Q-L-H-S-Q-K-R-K-I-T-L-NH$_2$ Ac-D-E-U-Q-L-S-U-Q-R-K-NH$_2$	(TD) chain (D) chain
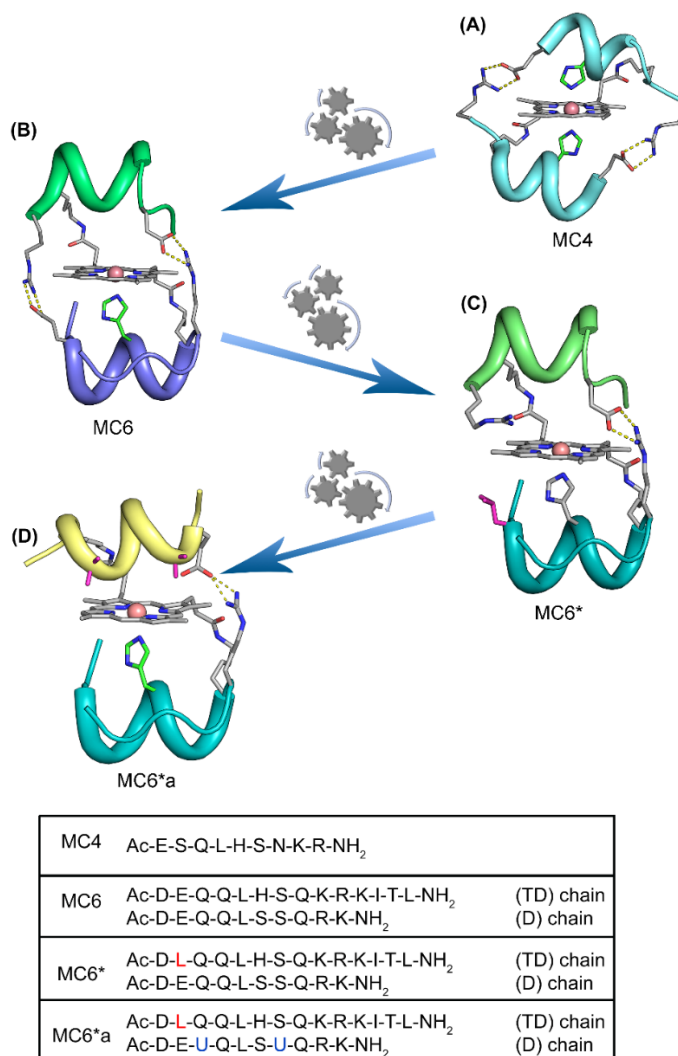
Figure 1.15. Evolution of mimochrome from hexacoordinated to catalytically active pentacoordinated models. Adapted with permission from [Nastri, F. et al. (2019)]

Compared to the previous MCs, the metal center is pentacoordinated, with the sixth position vacant for substrate binding. The iron analogue, FeMC6, indeed showed peroxidase–like activity. Next, the effects of second–shell interactions [Vitale, R. et al. (2015)] and of conformational constraints [Caserta, G. et al. (2018)] in tuning catalysis were evaluated. One of the two interhelical ion couple was removed by E2L mutation on the TD chain, which afforded MC6* (Figure 1.15C). The enhanced flexibility achieved in the Fe^{3+} derivative, positively impacted on its catalytic efficiency, being fourfold increased with respect to FeMC6 in the ABTS oxidation. Lastly, the insertion of two helix–inducing α–aminoisoburyrric acid (Aib) residues in positions 3 and 7 of the D peptide yielded MC6*a, the latest analogue in mimochrome family (Figure 1.15D). The catalytic parameters obtained for the iron complexes of the different catalytically active mimochrome analogues are listed in Table 1.1 in comparison with those obtained for HRP.

Table 1.1 Comparison of the kinetic parameters obtained for the different Mimochromes analogues in ABTS oxidation ([1]:[Vitale, R. et al. (2015)]; [2]:[Caserta, G. et al. (2018)])

	K_m^{ABTS} (mM) 10^2	K_m^{H2O2} (mM)	k_{cat} (s^{-1}) 10^3	k_{cat}/K_m^{ABTS} (mM^{-1}s^{-1}) 10^{-3}	k_{cat}/K_m^{H2O2} (mM^{-1}s^{-1})	TON 10^{-3}
FeMC6[1]	8.4 ± 0.2	(4.4±0.2)·10^1	0.37±0.01	4.4 ± 0.3	8.4 ± 0.6	4.0
FeMC6*[2]	5.0±0.6	(1.3±0.2)·10^2	2.3±0.2	46±7	1.8±0.3·10^1	5.9
FeMC6*a[2]	9±1	(4.4±0.5)·10^2	5.8±0.3	64±8	1.3±0.2·10^1	14
HRP[2]	70±8	(9.3±0.5)·10^{-1}	2.7±0.03	3.8±0.5	2.9±0.2·10^3	50

FeMC6*a catalyst in ABTS oxidation is to date the most robust and better performing catalyst among mimochromes with more than two–fold increase in turnover number, compared to FeMC6*. Moreover, FeMC6*a displays a 2–fold higher k_{cat} and a 20–fold higher catalytic efficiency than that of natural HRP in the ABTS oxidation.

NMR data (acquired on the diamagnetic cobalt analogue) suggest the interaction of the Aib methyl groups with the porphyrin ring. This interaction stabilizes the helix–heme–helix sandwich structure, which protects FeMC6*a from self–oxidative damage [Caserta, G. et al. (2018)].

MC6*a (Figure 1.16) is a versatile scaffold that may accommodate different metal ions, giving rise to a plethora of different catalytic properties.
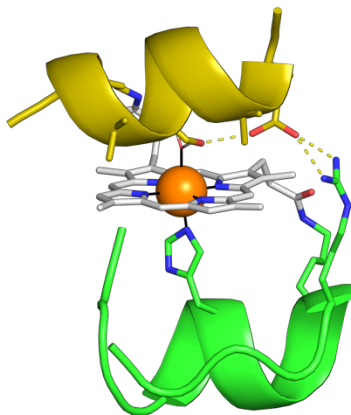
Figure 1.16. FeMC6*a model structure.

The cobalt derivative, CoMC6*a is able to catalyze hydrogen evolution reactions in which protons are electrochemically reduced to hydrogen (H_2) in water at neutral pH under aerobic conditions. In a recent paper, the activity of CoMC6*a was compared to the activity of cobalt microperoxidase–11 (CoMP11–Ac). The study revealed that CoMC6*a has significantly enhanced turnover number of over 230 000 cycles, in comparison to only 25 000 for CoMP11–Ac. Furthermore, comparison of cyclic voltammograms of CoMC6*a and CoMP11–

Ac indicates that addition of 2,2,2–trifluoroethanol lowers the overpotential for catalytic H_2 evolution by up to 100 mV for CoMC6*a while no effect was observed for CoMP11–Ac, demonstrating that the peptide structure actively drives the catalysis [Firpo, V. et al. (2018)].

Catalytic performances of manganese derivative were also investigated [Leone, L. et al. (2018)]. MnMC6*a represents also an efficient catalyst in sulfoxidation of thioethers with notable catalytic performances in terms of turnover number and chemoselectivity. Comparison of the spectroscopic and catalytic performances of MnMC6*a with Mn–reconstituted HRP (Mn–HRP) highlighted that, although MnMC6*a resembles Mn–HRP spectroscopically both in resting state and high–valent oxidation states. It overcomes the catalytic performances of its natural counterpart: it is able to perform thioethers oxidation following a direct oxygen transfer pathway, with higher yields and chemoselectivity.

1.1.8 **Aim of the thesis**

The thorough investigation over the structural and functional properties of heme proteins has allowed bioinorganic chemists to design, engineer or recreate heme proteins, structuraly and/or functionally resembling natural counterparts. In particular, through design by miniaturization catalysts with enhanced performances can be obtained.

Within this PhD project, the activity and application range of FeMC6*a, a synthetic peroxidase designed by miniaturization approach, was explored in bioremediation, electrochemical sensor development and as building block in the construction of gold based bionanomaterials.

In particular, the catalytic activity of FeMC6*a was explored in the field of halophenols oxidation, using 2,4,6-trichlorophenol as model substrate (Chapter 2). The excellent catalytic properties of FeMC6*a encouraged us to expand the activity towards a library of halophenols, differing both in halogen and degree of substitution (Chapter 6). Furthermore, preliminary investigation over the application of FeMC6*a as tool in a synthetic peroxidase-based bioremediation strategy were also performed (Chapter 2).

FeMC6*a redox properties were electrochemically investigated. Interestingly, the study highlighted a strong effect of halogenated alcohols over the electrochemical behavior of the synthetic peroxidase. The peculiarity of FeMC6*a electrochemical features, was applied in the development of an amperometric sensor for the detection of halogenated alcohols in water mixtures. Moreover, preliminary investigation over the operational principle highlighted a relationship between helix content and observed currents (Chapter 3).

Lastly, FeMC6*a was used as building block in the construction of gold based bionanomaterials. Gold nanoparticles were chosen as solid matrix. The immobilization was achieved either by direct chemisorption (Chapter 6) or by applying a bio-orthogonal chemistry approach (Chapter 4). Both approaches

afforded functional nano-bioconjugates which partially maintained the peroxidase activity.

1.2 Synthesis of FeMC6*a: overview

The synthesis of FeMC6*a (Figure 1.17) consisted of three steps. The first one involved the solid–phase synthesis of the peptide chains; the second one involved the solution–phase conjugation of the protected peptides to the porphyrin. Finally, after side chain deprotection, insertion of the metal into the porphyrin–peptide conjugate was performed to provide the metal complex.
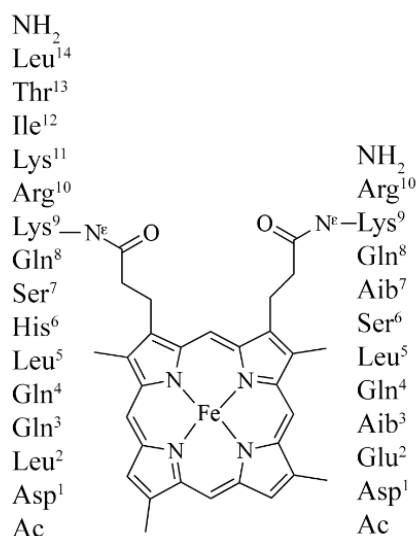
Figure 1.17. FeMC6*a sequence

The two peptide chains were synthesized manually on a medium 20 mmol scale by 9–fluorenylmethoxycarbonyl (Fmoc) chemistry approach. A super acid labile resin was used in order to obtain protected peptides after cleavage from the solid support. In both peptides, a monomethyltrityl (Mtt) protecting group was used for Lys9 side chain. After the selective removal of Mtt protecting group, the peptides were cleaved from the resin without removing the other side chain protecting groups. The simultaneous deprotection of Lys9 side chain and cleavage of the peptide from the resin was performed by thoroughly washing the

resin with 1%(v/v) TFA in dichloromethane.

With this strategy, it was possible to avoid the interference of other residues sidechains and selectively couple deuteroporphyrin IX (DPIX) onto Lys9 of both peptides, following the scheme reported below (Figure 1.18).
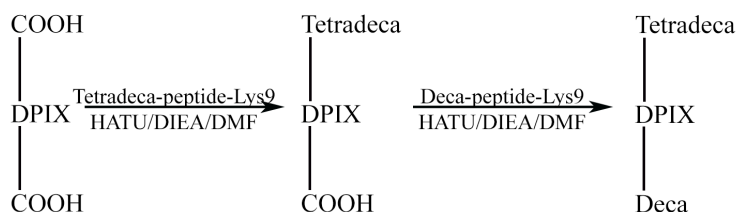
Figure 1.18. Schematic representation of the peptide–porphyrin conjugation strategy.

1.2.1 Peptide synthesis

1.2.1.1 Assembly of the decapeptide chain

The amino acid sequence of the fully protected decapeptide is:

Ac–Asp(OtBu)–Glu(OtBu)–Aib–Gln(Trt)–Leu–Ser(tBu)–Aib–Gln(Trt)–
Lys(Mtt)–Arg(Pbf)–NH$_2$.
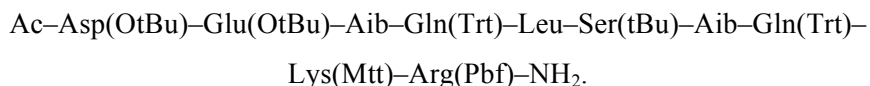
The decapeptide chain was synthesized in solid phase with Fmoc chemistry on 20.0 mmol scale, using a "stepwise chain elongation" approach. The synthetic details are reported in section 1.3.3. After completion of the sequence, a small amount of resin was withdrawn and fully deprotected to check for purity and sequence identity.

The peptide purity was assessed by analytical RP– HPLC, using a C18 column and a linear elution gradient of water/acetonitrile 0.1%(v/v) TFA. The HPLC chromatogram of the crude decapeptide chain and the corresponding mass spectrum are reported in Figures 1.19 and 1.20.
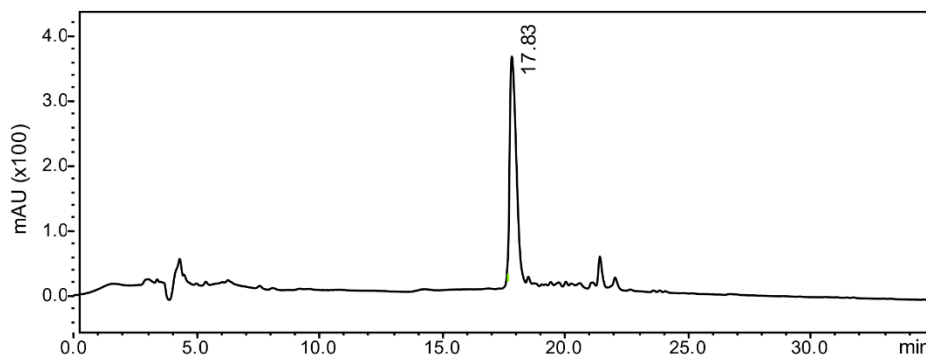
Figure 1.19. LC chromatogram of the decapeptide chain, R_t= 17.83 min.
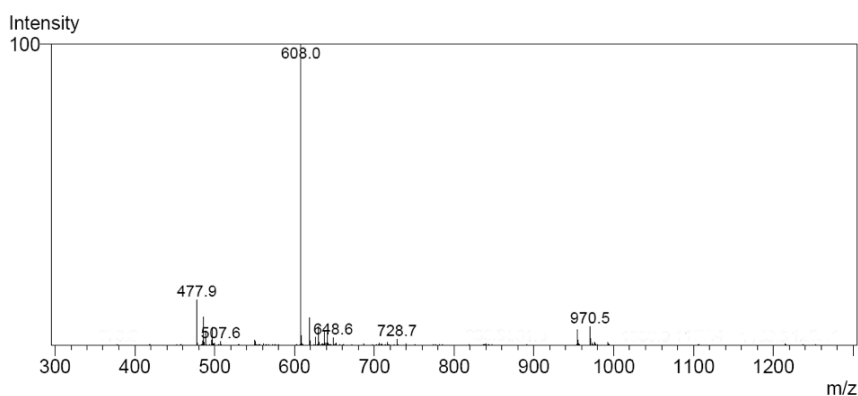
Figure 1.20. MS spectrum of the peak at R_t= 17.83 min.

ESI–MS analysis of the product at R_t= 17.83 min corresponds to the mass of the expected peptide chain (theoretical mass 1213.640 Da, deconvoluted mass 1213.9±0.1 Da, 84% yield.);

Furthermore, to address sequence identity, a MSMS analysis of the peak at 17.83 min was performed. The peptide was analyzed by LC–TANDEM mass spectrometry. The fragmentation profile corresponds to the desired peptide and its product ion scan showed mass peaks consistent with the theoretical expected transitions (Table 1.2).

#	Immon.	b	b^{++}	b^{+++}	Seq.	y	y^{++}	y^{+++}	#
1	88.10				D	1215.34	**608.17**	405.78	10
2	102.13	**287.25**	144.13	96.42	E	1058.21	529.61	**353.41**	9
3	58.12	*372.32*	186.68	124.79	U	**929.10**	465.05	310.37	8
4	101.14	*500.48*	250.74	167.50	Q	**843.99**	422.50	282.00	7
5	86.17	**613.64**	**307.32**	205.22	L	**715.86**	358.44	239.29	6
6	60.09	700.71	350.86	234.24	S	**602.71**	**301.86**	201.57	5
7	58.12	785.82	393.41	262.61	U	515.63	258.32	172.55	4
8	101.14	913.95	457.48	305.32	Q	*430.52*	215.77	144.18	3
9	101.19	1042.12	521.56	348.05	K	**302.40**	151.70	101.47	2
10	129.20				R				1

Table 1.2. Fragmentation profile of decapeptide. Green boxes indicate the experimentally found fragments as main peaks, yellow boxes indicate fragments found as shoulders.

1.2.1.2 **Assembly of the tetradecapeptide chain**

The amino acid sequence of the fully protected tetradecapeptide is:

Ac–Asp(OtBu)–Leu–Gln(Trt)–Gln(Trt)–Leu–His(Trt)–Ser(tBu)–Gln(Trt)–Lys(Mtt)–Arg(Pbf)–Lys(Boc)–Ile–Thr(tBu)–Leu–NH$_2$.

The synthetic strategy was similar to that above reported for the decapeptide chain. The synthetic details are reported in Section 1.3.3.

After completion of the sequence, a small amount of resin was withdrawn and fully deprotected to check for purity and sequence identity.

The peptide purity was assessed by analytical RP–HPLC, using a C18 column and a linear elution gradient of water/acetonitrile 0.1% (*v/v*) TFA. The HPLC chromatogram of the crude tetradecapeptide chain and the corresponding mass spectrum are reported in Figures 1.21 and 1.22.
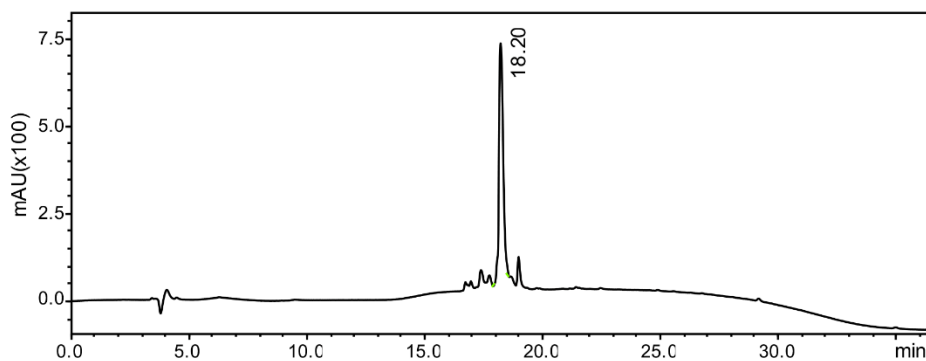
Figure 1.21. RP–HPLC chromatogram of the tetradecapeptide chain, R_t= 18.20 min.
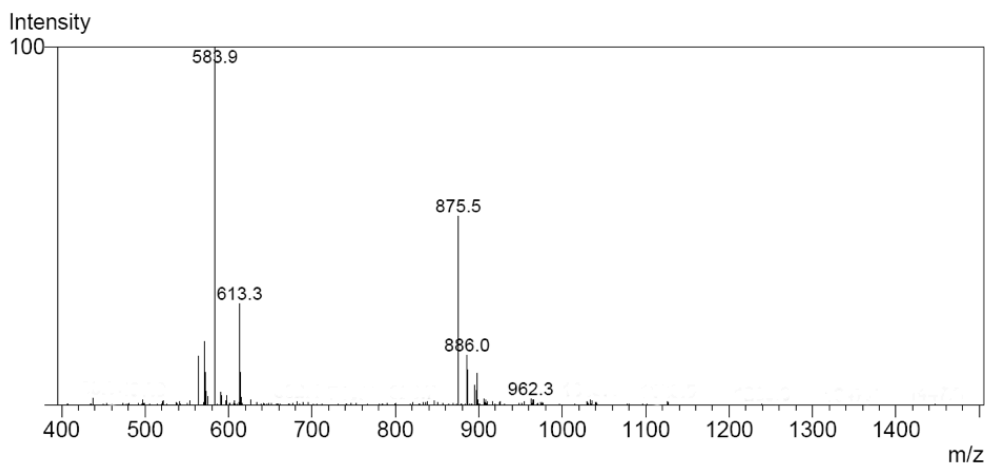
Figure 1.22. Mass spectrum of the tetradecapeptide chain, R_t=18.20 min.

ESI–MS analysis (Figure 1.22) of the main product (R_t= 18.20 min) indicated the formation of the desired tetradecapeptide chain molecular mass (theoretical mass 1749.028 Da, deconvoluted mass 1748.8±0.2 Da, 86% yield). As before, sequence identity was ascertained by MSMS analysis. Table 1.3 reports the comparison between theoretical and experimentally observed peptide fragments at retention time 18.20 min.

#	Immon.	b	b^{++}	b^{+++}	Seq.	y	y^{++}	y^{+++}	#
1	88.04				D	1749.01	875.01	583.68	14
2	86.10	271.13	136.07	91.05	L	1591.97	796.49	531.33	13
3	101.07	399.19	200.10	133.73	Q	1478.89	739.95	493.64	12
4	101.07	527.25	264.13	176.42	Q	1350.83	675.92	450.95	11
5	86.10	640.33	320.67	214.12	L	1222.77	611.89	408.26	10
6	110.07	777.39	389.20	259.80	H	1109.69	555.35	370.57	9
7	60.04	864.42	432.71	288.81	S	972.63	486.82	324.88	8
8	101.07	992.48	496.74	331.50	Q	885.60	443.30	295.87	7
9	101.11	1120.58	560.79	374.20	K	757.54	379.27	253.18	6
10	129.11	1276.68	638.84	426.23	R	629.45	315.23	210.49	5
11	101.11	1404.77	702.89	468.93	K	473.34	237.18	158.45	4
12	86.10	1517.86	759.43	506.62	I	345.25	173.13	115.75	3
13	74.06	1618.90	809.96	540.31	T	232.17	116.59	78.06	2
14	86.10				L	131.12			1

Table 1.3. Fragmentation profile of tetradecapeptide. Green boxes indicate the experimentally found fragments as main peaks, yellow boxes indicate fragments found as shoulders.

1.2.2 Synthesis of the FeMC6*a
1.2.2.1 Conjugation of the peptide chains to deuteroporphyrin IX

The mono–conjugated intermediate was obtained by coupling the tetradecapeptide to the DPIX. A solution containing protected TD peptide was added slowly over 1 hour to a solution containing DPIX in the presence of HATU activating agent. The slow additions ensure a single peptide–porphyrin coupling, avoiding formation of double conjugation products. After 3 h from end of additions of TD peptide the mixture was dried and purified by direct phase chromatography to remove unreacted porphyrin.

After purification, the tetradeca–DPIX monoadduct was coupled with decapeptide using HATU as activating agent yielding D–DPIX–TD protected diadduct. After 16 hours, the reaction was evaporated and deprotected with a mixture of TFA and scavengers, yielding MC6*a free base. The crude product was precipitated and washed three times in diethylether. After drying, the precipitate was dissolved in H_2O 0.1% (*v/v*) TFA and lyophilized. After lyophilization, ~9 grams of product were obtained.

The crude product was purified by preparative RP–HPLC and fractions containing MC6*a with purity >90% were pooled together.

The purity and identity of the product was ascertained by LC–MS analysis (R_t = 21.31 min; theoretical mass 3438.201 Da, deconvoluted mass 3438.17±0.27 Da). (Figure 1.23 and 1.24)
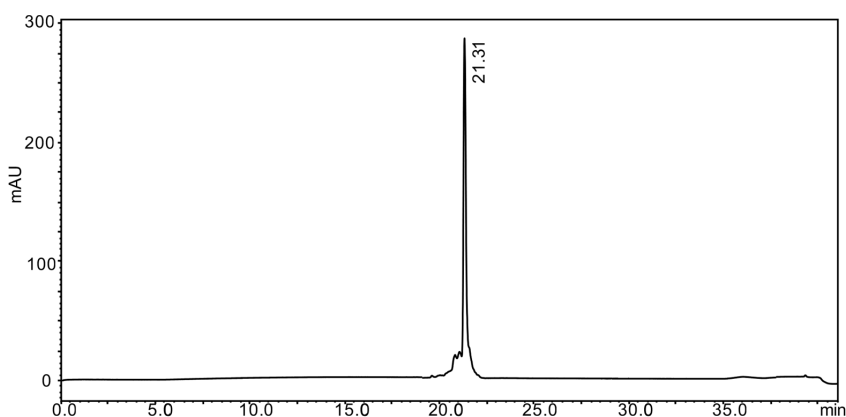
Figure 1.23. HPLC profile of purified MC6*a free base
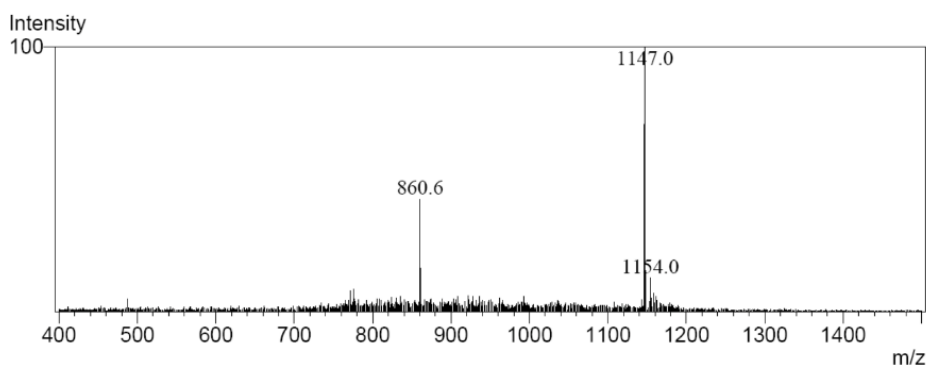
Figure 1.24. MS of MC6*a free base.

1.2.2.2 Iron insertion

Iron was inserted MC6*a free base. Metal insertion was carried out by using a slightly modified acetate method [Caserta, G. et al. (2018)], in which MC6*a free base was dissolved in a 3:2 (v/v) mixture of glacial acetic acid and TFE in

the presence of 20 equivalents of Fe(OAc)$_2$. To prevent oxidation of Fe(II) to Fe(III), during the insertion, the reaction was carried out under nitrogen. The insertion reaction was followed by RP–HPLC–ESI–MS, on a C18 column, using a linear gradient elution of water/acetonitrile 0.1% TFA. After completion, the reaction was purified from the excess of iron. Figures 1.25 and 1.26 report the RP–HPLC profile and the mass spectrum of the purified FeMC6*a.
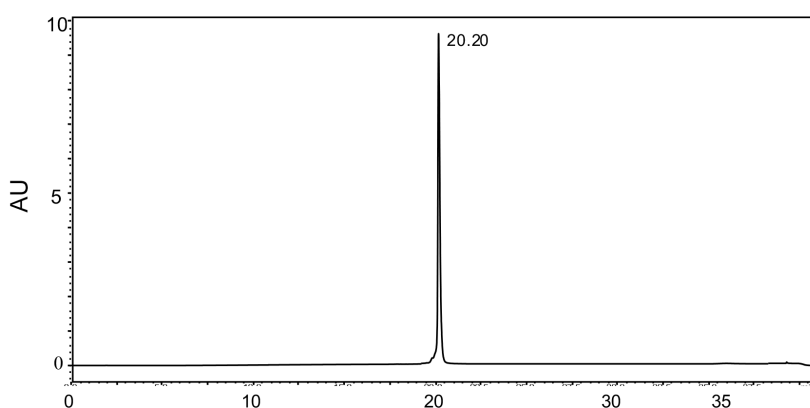
Figure 1.25. HPLC chromatogram (λ=387 nm) of pure FeMC6*a.
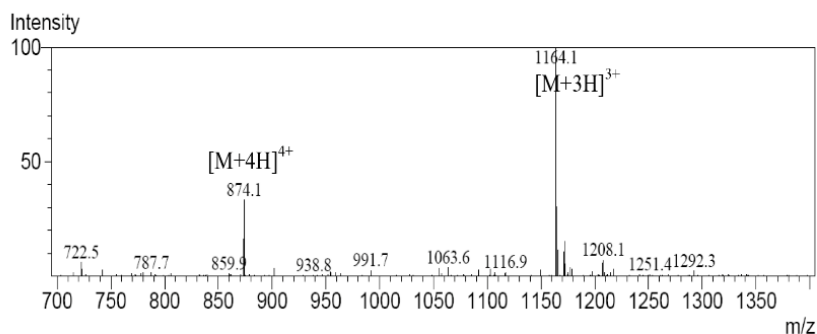
Figure 1.26. ESI–MS spectrum of FeMC6*

1.3 **Materials and Methods**

1.3.1 **Materials**

Peptide synthesis was carried out using reagent grade anhydrous solvents. Solvents with a higher degree of purity were used in the preparation of samples for LC–MS investigations and were provided by Romil. Scavengers such as, ethanedithiol (EDT); triisopropylsilane (TIS), and TFE were supplied by Sigma Aldrich; trifluoroacetic acid (TFA) and diisopropylethylamine (DIEA) were from Applied Biosystem; acetic anhydride was from Fluka and piperidine was from Merck. N,N–dimethylformamide (DMF) and dichloromethane (DCM) were supplied by Romil. All reagents were used without further purification.

All 9–fluorenylmethoxycarbonyl (Fmoc) protected amino acids and NovaSyn® TG Sieber resin (substitution level 0.61 mmol/g) were purchased from NovaBiochem; coupling reagents HOBt, HATU and COMU were provided by LC Sciences, Anaspec and Merck, respectively. Deuteroporphyrin IX was from Porphyrin Products. Iron (II) acetate was purchased from Aldrich. Precoated silica G–60 plates were purchased from Merck.

Solvent mixtures are indicated in the respective sections.

1.3.2 **Instrumentation**

HPLC and LC–MS analysis were performed by a Shimadzu LC–10ADvp system equipped with an SPDM10Avp diode–array detector. ESI–MS spectra were recorded on a Shimadzu LC–MS–2010EV system with ESI interface and Shimadzu LC–MS solution Workstation software for data processing. A Q–array–octapole–quadrupole mass analyzer was used as detector. The optimized MS parameters were selected as followed: curved desolvation line (CDL) temperature 250°C; heat block temperature 250°C; probe temperature 250°C; detector gain 1.6 kV; probe voltage +4.5 kV; CDL voltage –15 V. Nitrogen (>98%) served as nebulizer gas (flow rate: 1.5 L/min). Tandem mass experiments were recorded on Shimadzu LC–MS–8040 triple quadrupole

equipped with ESI ionization source. Argon was used as ion gas in the CID cell. Fragmentation was operated at –70 eV and data were analyzed by Shimadzu LC–MS solution Workstation software.

Purifications were accomplished by preparative RP–HPLC with Shimadzu LC–8A connected to a SPD–20A Shimadzu UV–Vis spectrophotometric detector. The molecular graphics pictures were generated with PyMOL software (DeLano Scientific ltd).

1.3.3 **Solid phase peptide synthesis**

Two peptide chains of FeMC6*a (decapeptide and tetradecapeptide chains) were synthesized on a 20 mmol scale using Fmoc solid phase peptide synthesis (SPPS) manually in a 3 L glass flask equipped with mechanical stirring and sintered glass frit. The super acid labile Nova Syn TG Sieber resin (substitution level 0.61 mmol/g) was used for peptide synthesis. For the synthesis of the two peptides the following amino acids were used:

– Tetradecapeptide (TD):

  Ac–Asp–Leu–Gln–Gln–Leu–His–Ser–Gln–Lys–Arg–Lys–Ile–Thr–Leu–NH$_2$;

– Decapeptide (D):

        Ac–Asp–Glu–Aib–Gln–Leu–Ser–Aib–Gln–Lys–Arg–NH$_2$.
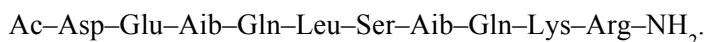
For the synthesis of the peptides, the amino acids used are reported as follows: Fmoc–Asp(OtBu)–OH; Fmoc–Leu–OH; Fmoc–Gln(Trt)–OH; Fmoc–His(Trt)–OH; Fmoc–Ser(tBu)–OH; Fmoc–Lys(Mtt)–OH; Fmoc–Arg(Pbf)–OH; Fmoc–Lys(Boc)–OH; Fmoc–Ile–(OH); Fmoc–Thr(tBu)–OH; Fmoc–Glu(OtBu)–OH; Fmoc–Aib–OH.

(tBu: tertbuthyl; Trt: trityl; Mtt: monomethyltrityl; Pbf: pentamethylbenzofuranyl; Boc: tertbutyloxycarbonyl).

The synthetic procedure is the same for all the peptides and can be summarized as follows.

1. Deprotection: α–Fmoc group was removed at the beginning of every cycle with a 20% piperidine solution in DMF. After deprotection, the resin was washed 6 times with DMF to remove the piperidine. The peptide resin was then ready for coupling.
2. Activation: Prior addition of the protected aminoacid to the resin, 1 equivalent of HATU (COMU was used for difficult couplings) was added to Fmoc–amino acid DMF solution in the presence of 3 equivalents of diisopropylethylamine (DIEA).
3. Coupling: in the coupling step, the HATU activated Fmoc–amino acid reacts with the amino–terminal group of the growing peptide chain, in DMF, to form a peptide bond. Single coupling was conducted for all amino acid excepts for Aib residues, which were instead double–coupled with COMU.
4. Capping reaction was performed after each coupling step, using Ac_2O/DIEA solution in DMF.

Deprotection, coupling and capping steps were repeated with each subsequent amino acid, until the chain assembly was completed. When the coupling was complete, the resin was washed with DMF. Peptides N–terminal amino groups were acetylated with Ac_2O/DIEA solution in DMF. At completion of the synthesis, the resin was washed several times with DCM, isopropanol methanol and diethylether and finally dried.

1.3.4 **Mtt deprotection and cleavage of peptides**

Simultaneous cleavage of peptide from resin and Mtt (4–methyltrityl) deprotection from the ε–amino group of Lys9 (TD) and Lys9 (D) was performed. Four resin volumes of a freshly prepared cleavage mixture (1 %(v/v) TFA, 2 %(v/v) triisopropylsilane in DCM were added. The acidic mixture was incubated for 2 min, under mixing, and the solution was filtered with a vacuum pump into an ice–cold flask containing 2 mL of 10 %(v/v) pyridine/methanol. The peptides elution was controlled by TLC analysis, by using as eluent the mixture chloroform/methanol 90/10 %(v/v); each step was repeated until no

product was detected in the collected fractions. The neutralized fractions containing the product were pooled and then evaporated under reduced pressure up to 5% of the volume. The protected peptide was extracted in chloroform/water three times, then the organic phase was anhydrified over sodium sulfate and dried under vacuum.

Peptide homogeneity and identity were assessed by analytical RP–HPLC–ESI mass spectrometry. For protected peptides, a Vydac C8 column (4.6 mm·150 mm; 5 μm), was used in the LC–MS analysis, eluted with H_2O 0.1% TFA (*v/v*) (solvent A) and acetonitrile 0.1%(*v/v*) TFA (solvent B) linear gradient, from 50% to 90% B over 40 min, at 0.5 mL/min flow rate.

1.3.5 Coupling between peptides and deuteroporphyrin

1.3.5.1 Synthesis of the TD–DPIX monoadduct

DPIX (1.23 g; 2.8 mmol) was dissolved in a solution of anhydrous DMF containing 20 %(*v/v*) pyridine, 200 mL) under flushing nitrogen while vigorous stirring. Then, HATU (1.17 g, 3.1 mmol) was added to the solution. A solution of *(TD)* peptide (4.45 g, 2.1 mmol) in anhydrous DMF (100 mL) was finally added in aliquots of 5 mL over 1 hour. The peptide solution was slowly added to the deuteroporphyrin solution, in order to avoid the formation of the undesired di–substituted porphyrin (TD–DPIX–TD). The reaction mixture was stirred for 2 h at room temperature, and the pH was checked every 20 min and adjusted with DIEA (pH ≈ 8.0), if necessary. The reaction was monitored by analytical HPLC (Vydac C8 column, using a gradient of acetonitrile in 0.1% aqueous TFA, 50% to 90%B over 20 min), and by TLC (solvent system chloroform/methanol 90:10, R_f = 0.49). The reaction mixture was then evaporated and the residue dried under reduced pressure. The crude products were purified by flash chromatography on a silica column using a chloroform/methanol gradient from 7 to 12% methanol over 6 column volumes. This purification allowed removing the excess of

deuteroporphyirin IX, the product of double conjugation of deuteroporphyirin IX (D–DPIX–D) and, if present, excess decapeptide.

1.3.5.2 **Synthesis of bis–conjugated peptide–porphyrin**

(TD)–DPIX mono–adduct was dissolved in a solution of anhydrous DMF containing 20%(v/v) pyridine (300 mL) under nitrogen while vigorous stirring. Then, a solution of the (D) peptide (2.8 g, 2 mmol) in anhydrous DMF (100 mL) was added in one portion. HATU (1.17 g, 3.1 mmol) was finally added to the mixture. The reaction was allowed to proceed at room temperature for a total of 16 h. The pH was checked during the reaction time and adjusted to ≈ 8, when necessary. The coupling progress was followed by TLC (chloroform/methanol 90:10, R_f = 0.65). Afterwards, the reaction mixture was evaporated under reduced pressure and dried.

Side chain deprotection was achieved by addition of the cleavage mixture (94% TFA, 2.5% EDT, 1% TIS, 2.5% H_2O, ($v/v/v/v$)). The reaction was performed at 0 °C for 1h and at room temperature for further 2 hours, while stirring. The final mixture was concentrated on a rotary evaporator and the crude product was precipitated by adding cold diethyl ether. The mixture was centrifuged (room temperature, at 3300 g), the supernatant was removed and the precipitate was washed twice with three volumes of cold diethyl ether. The crude product was dried, dissolved in H_2O 0.1% TFA (v/v) and lyophilized. The lyophilization yielded 9 grams of crude product. A Vydac C18 column (4.6 mm·150 mm; 5 µm) was used during LC–MS analyses, eluted with H_2O 0.1% TFA (v/v) (solvent A) and acetonitrile 0.1% TFA (v/v) (solvent B) linear gradient, from 10% to 50% B over 60 min, at 0.5 mL/min flow rate. The crude material was then purified by preparative RP–HPLC. A Vydac C18 column (250 mm·50 mm; 10 µm) was used, eluted with H_2O 0.1% TFA (v/v) (solvent A) and acetonitrile 0.1% TFA (v/v) (solvent B) with a linear gradient, from 10% to 50% B over 50

min, at 100.0 mL/min flow rate. This purification step yielded MC6*a free base (purity> 90%).

1.3.5.3 **Iron insertion**

Iron was inserted into two isomers using a slightly modified acetate method. Iron (II) acetate (20 molar excess) was added to a solution of free base in 3:2 (v/v) AcOH/TFE mixture (MC6*a concentration: $2.0 \bullet 10^{-4}$ M). The reaction mixture was kept at 50 °C for 4 h, refluxing under nitrogen and monitored by analytical HPLC, using a Vydac C18 column, eluted with H_2O 0.1%(v/v) TFA (solvent A) and acetonitrile 0.1%(v/v) TFA (solvent B) linear gradient, from 10%(v/v) to 50%(v/v) B over 30 min, at 1.0 mL/min flow rate. At the end of the reaction the solvent was removed under vacuum, and the excess iron was removed by RP–HPLC. A Vydac C18 column (250 mm·50 mm; 10 μm) was used, eluted with H_2O 0.1%(v/v) TFA (solvent A) and acetonitrile 0.1%(v/v) TFA (solvent B) with a linear gradient, from 10%(v/v) to 50%(v/v) B over 50 min, at 100.0 mL/min flow rate. ESI–MS confirmed the expected molecular weight (See section 1.2.2.2).

1.4 **References**

- J. S. Ahammad "Hydrogen Peroxide Biosensors Based on Horseradish Peroxidase and Hemoglobin" J. Biosens. Bioelectron. S9 (2012), 001.

- S. Aibara, T. Kobayashi Y. Morita "Isolation and properties of basic isoenzymes of horseradish peroxidase" J. Biochem. (Tokyo), 90 (1981), 489–496.

- R. F. Alford, A. Leaver-Fay, J. R. Jeliazkov, M. J. O'Meara, F. P. DiMaio, H. Park, M. V. Shapovalov, P. D. Renfrew, V. K. Mulligan, K. Kappel, et al. "The rosetta all-atom energy function for macromolecular modeling and design" J. Chem. Theory Comput. 13 (2017), 6, 3031-3048.

- M. Ali, M. Ahmad, Q. Husain "Redox mediated decolorization and detoxification of direct blue 80 by partially purified ginger (Zingiber officinale) peroxidase" Int. J. Environ. Agri. Res. 2 (2016), 4, 19–30.

- M. Ali, Q. Husain, M. Ahmad "Enhanced catalytic activity and stability of ginger peroxidase immobilized on amino functionalized silica coated titanium dioxide nanocomposite" Water Air Soil Poll. 222 (2017), 28–46.

- M. Ali, Q. Husain, S. Sultana, M. Ahmad (2018) "Immobilization of peroxidase on polypyrrole–cellulose–graphene oxide nanocomposite via non–covalent interactions for the degradation of reactive blue 4 dye" Chemosphere 202 (2018), 198–207.

- S. D. Allison, J. Schultz (2004) "Differential activity of peroxidase isozymes in response to wounding, gypsy moth and plant hormones in northern red oak" J. Chem. Ecol. 30 (2004), 1363–1379.

- O. Amor-Gutiérrez, E. Costa-Rama, M. T. Fernández Abedul "Chapter 25 - Determination of glucose with an enzymatic paper-based sensor" Laboratory Methods in Dynamic Electroanalysis (2020), 257-265.

- F. H. Arnold "Directed Evolution: Bringing New Chemistry to Life" Angew. Chem. Int. Ed. 57 (2018), 4143–4148.

- M. Arslan (2011) "Immobilization horseradish peroxidase on amine–functionalized glycidyl meth– acrylate–g–poly(ethylene terephthalate) fibers for use in azo dye decolorization" Polym. Bull. 66 (2011), 865–879.

- H. L. Axelrod, M. Y. Okamura "The structure and function of the cytochrome c2: reaction center electron transfer complex from Rhodobacter sphaeroides"

Photosynth. Res. 85 (2005), 1, 101–114.

- M. Azevedo, V. C. Martins, D. M. Prazeres, V. Vojinovic´, J M. Cabral, L. P. Fonseca "Horseradish peroxidase: a valuable tool in biotechnology" Biotechnology Annu. Rev. 9 (2003), 1387–2656.

- E. G. Baker, G. J. Bartlett, K. L. Porter Goff, D. N. Woolfson "Miniprotein Design: Past, Present, and Prospects" Acc. Chem. Res. 50 (2017), 2085–2092.

- R. Barceló, F. Pomer (2001) "Oxidation of cinnamyl alcohols and aldehydes by a basic peroxidase from lignifying *Zinnia elegans* hypocotyls" Phytochem. 57 (2001), 1105–1113.

- M. A. Bernards, M. A. W. D. Fleming, D. B. Llewellyn, R. Priefer, X. Yang "Biochemical characterization of the suberization–associated anionic peroxidase of potato" Plant. Physiol. 121 (1999), 135–146.

- Bhagi–Damodaran, I. Petrik, Y. Lu "Using Biosynthetic Models of Heme–Copper Oxidase and Nitric Oxide Reductase in Myoglobin to Elucidate Structural Features Responsible for Enzymatic Activities" Isr. J. Chem. 56 (2016), 773–790.

- Bhagi–Damodaran, J. H. Reed, Q. Zhu, Y. Shi, P. Hosseinzadeh, B. A. Sandoval, K. A. Harnden, S. Wang, M. R. Sponholtz, E. N. Mirts, S. Dwaraknath, Y. Zhang, P. Moënne–Loccoz, Y. Lu "Heme redox potentials hold the key to reactivity differences between nitric oxide reductase and heme–copper oxidase" Proc. Natl. Acad. Sci. U.S.A. 115 (2018), 24, 6195–6200.

- G. Bhardwaj, V. K. Mulligan, C. D. Bahl, J. M. Gilmore, P. J. Harvey, O. Cheneval, G. W. Buchko, S. V. S. R. K. Pulavarti, Q. Kaas, A. Eletsky et al. "Accurate de Novo Design of Hyperstable Constrained Peptides" Nature 528 (2016), 329–335.

- M. C. Blanco-López, M. J. Lobo-Castañón, M. T. Fernández Abedul "Chapter 17 - Bienzymatic amperometric glucose biosensor" Laboratory Methods in Dynamic Electroanalysis (2020), 173-181.

- M. G. Boersma, J. L. Primus, J. Koerts, C. Veeger, I. M. C. M. Rietjens, Eur. J. Biochem. 267 (2000), 6673–6678.

- K. L. Bren "Engineered Biomolecular Catalysts" J. Am. Chem. Soc. 139 (2017), 14331–14334.

- G. Caserta, S. Roy, M. Atta, V. Artero, M. Fontecave "Artificial hydrogenases:

Chapter 1

biohybrid and supramolecular systems for catalytic hydrogen production or uptake"
Curr. Opin. Chem. Biol. 25 (2015), 36–47.

- G. Caserta, M. Chino, V. Firpo, G. Zambrano, L. Leone, D. D'Alonzo, F. Nastri, O. Maglio, V. Pavone, A. Lombardi "Enhancement of peroxidase activity in artificial Mimochrome VI catalysts through rational design" ChemBioChem. 19 (2018), 1823–1826.

- G. Cheng, J. C. Salerno, Z. Cao, P. J. Pagano, J. D. Lambeth "Identification and characterization of VPO1, a new animal heme–containing peroxidase" Free Radic. Biol. Med. 45 (2008), 1682–1694.

- M. Chino, O. Maglio, F. Nastri, V. Pavone, W. F. DeGrado, A. Lombardi "Artificial Diiron Enzymes with a De Novo Designed Four–Helix Bundle Structure" Eur. J. Inorg. Chem. 21 (2015), 3371–3390.

- M. Chino, S.-Q. Zhang, F. Pirro, L. Leone, O. Maglio, A. Lombardi, W. F. DeGrado "Spectroscopic and Metal Binding Properties of a de Novo Metalloprotein Binding a Tetrazinc Cluster" Biopolymers 109 (2018), e23339.

- M. Chino, L. Leone, G. Zambrano, F. Pirro, D. D'Alonzo, V. Firpo, D. Aref, L. Lista, O. Maglio, F. Nastri, A. Lombardi "Oxidation catalysis by iron and manganese porphyrins within enzyme–like cages" Biopolymers 109 (2008), e23107

- L. A. Churchfield, F. A. Tezcan "Design and Construction of Functional Supramolecular Metalloprotein Assemblies" Acc. Chem. Res. 52 (2019), 345–355.

- M. Costas "Selective C–H oxidation catalyzed by metalloporphyrins" Coord. Chem. Rev. 255 (2011), 2912–2932.

- R. Crichton, "Biological Inorganic Chemistry: A New Introduction to Molecular Structure and Function" (2019) 3rd Edition. Academic Press.

- R. Cruz–Silva, E. Amaro, A. Escamilla, M. E. Nicho, S. Sepulveda–Guzman, L. Arizmendi, J. Romero–García, F. F. Castillón–Barraza, M. H. Farias "Biocatalytic synthesis of polypyrrole powder, colloids, and films using horseradish peroxidase J. Colloid Interface Sci. 328 (2008), 2, 263–269.

- Dallacosta, E. Monzani, L. Casella "Reactivity study on microperoxidase–8." J. Biol. Inorg. Chem. 8 (2003), 770–776.

- Dallacosta, L. Casella, E. Monzani "Modified microperoxidases exhibit different

reactivity towards phenolic substrates" ChemBioChem 5 (2004), 1692–1699.

- H. J. Davis and T. R. Ward "Artificial metalloenzymes: challenges and opportunities" ACS Cent. Sci. 5 (2019), 1120−1136

- L. Di Costanzo, S. Geremia, L. Randaccio, F. Nastri, O. Maglio, A. Lombardi and V. Pavone "Miniaturized heme proteins: crystal structure of Co(III)–mimochrome IV" J. Biol. Inorg. Chem. 9 (2009), 1017–1027.

- M. Dürrenberger, T. R. Ward "Recent achievements in the design and engineering of artificial metalloenzymes" Curr. Opin. Chem. Biol. 19 (2014), 99–106.

- M. ElKaoutit, I. Naranjo–Rodriguez, M. Domínguez, M. P. Hernández–Artiga, D. Bellido–Milla, J. L. Hidalgo–Hidalgo de Cisneros "A third–generation hydrogen peroxide biosensor based on Horserad– ish Peroxidase (HRP) enzyme immobilized in a Nafion–Sonogel–Carbon composite" Electrochim. Acta 53 (2008), 7131–7137.

- J. Everse "The structure of heme proteins Compounds I and II: some misconceptions" Free Radic. Biol. Med. 24 (1998), 1338–1346.

- P. Fernandez Freire, V. Labrador, J. M. Perez Martin, M. J. Hazen, "Cytotoxic effects in mammalian Vero cells exposed to pentachlorophenol" Toxicology, 210 (2005), 37–44.;

- V. Firpo, J. M. Le, V. Pavone, A. Lombardi, K. L. Bren "Hydrogen evolution from water catalyzed by cobalt–Mimochrome VI*a, a synthetic mini–protein" Chem. Sci. 9 (2018), 8582–8589.

- S. Friedle, E. Reisner, S. Lippard, J. "Current challenges of modeling diironenzyme active sites for dioxygenactivation by biomimetic synthetic complexes" Chem. Soc. Rev. 39 (2010), 2768–2779.

- M. Gajhede, D. J. Schuller, A. Henriksen, A. T. Smith, T. L. Poulos "Crystal structure ofhorseradish peroxidase C at 2.15 A resolution" Nat. Struct. Biol. 4 (1997), 1032–1038.

- E. Gkaniatsou, C. Sicard, R. Ricoux, L. Benahmed, F. Bourdreux, Q. Zhang, C. Serre, J.-P. Mahy "Enzyme encapsulation in mesoporous metal-organic frameworks for selective biodegradation of harmful dye molecules" Angew. Chem. Int. Ed., 57 (2018), 1-7.

- E. Gkaniatsou, C. Serre, J.-P. Mahy, N. Steunou, R. Ricoux, C. Sicard "Enhancing

microperoxidase activity and selectivity: immobilization in metal-organic frameworks" J. Porphyrins Phtalocyanines 23 (2019), 718-728.

- G. Gonzalez, B. Hannigan, W. F. DeGrado "A Real-Time All-Atom Structural Search Engine for Proteins" PLOS Comput. Biol. 10 (2014), e1003750.

- K. J. Grayson, J. R. Anderson "The ascent of man(made oxidoreductases)" Curr. Opin. Struct. Biol. 51 (2018), 149–155.

- T. Hayashi, Y. Hitomi, T. Ando, T. Mizutani, Y. Hiseda, S. Kitagawa, H. Ogoshi "Peroxidase Activity of Myoglobin Is Enhanced by Chemical Mutation of Heme-Propionates" J. Am. Chem. Soc. 121 (1999), 7747−7750.

- T. Hayashi, Y. Hisaeda "New fuctionalization of myoglobin by chemical modification of heme propionates" Acc. Chem. Res., 35 (2002), 1, 35-43.

- T. Hayashi, H. Dejima, T. Matsuo, H. Sato, D. Murata, Y. Hisaeda "Blue myoglobin reconstituted with an iron porphycene shows extremely high oxygen affinity" J. Am. Chem. Soc., 124 (2002), 38, 11226-11227.

- T. Heinisch, T. R. Ward "Artificial Metalloenzymes Based on the Biotin–Streptavidin Technology: Challenges and Opportunities" Acc. Chem. Res. 49 (2016), 9, 1711–1721.

- G. T. Hermanson "Bioconjugate techniques", 2nd edition (2008), Academic Press, San Diego, CA

- J. Huff "Long–term toxicology and carcinogenicity of 2,4,6–trichlorophenol" Chemosphere 89 (2012), 521–525.

- Q. Husain, M. Fahad Ullah "Biocatalysis: enzymatic basics and applications" Springer International Publishing. (2019) ISBN: 978–3–030–25023–2 pp. 139-163.

- T. K. Hyster, T. R. Ward "Genetic optimization of metalloenzymes: enhancing enzymes for non–natural reactions" Angew. Chem. Int. Ed. Engl. 55 (2016), 7344–7357.

- N. Igarashi, H. Moriyama, T. Fujiwara, Y. Fukumori. N. Tanaka "The 2.8 Å structure of hydroxylamine oxidoreductase from a nitrifying chemoautotrophic bacterium, Nitrosomonas europaea" Nat. Struct. Mol. Biol. 4 (1997), 276–284.

- M. Jeschek, S. Panke, T. R. Ward "Artificial metalloenzymes on the verge of new–to–nature metabolism" Trends Biotechnol. 36 (2018), 60–72.

- N. Kadnikova, N. M. Kostić "Effects of the environment on microperoxidase–11 and on its catalytic activity in oxidation of organic sulfides to sulfoxides" J. Org. Chem. 68 (2003), 2600–2608.

- K. Kariyawasam, R. Ricoux, J.–P. Mahy "Recent advances in the field of artificial hemoproteins: New efficient eco–compatible biocatalysts for nitrene–, oxene– and carbene–transfer reactions" J Porphyr. Phthalocya. 23 (2019), 11, 1273–1285.

- Khan, A. H. Rahmani, Y. H. Aldebasi, S. M. Aly "Biochemical and Pathological Studies on Peroxidases –An Updated Review" Glob. J. Health Sci. 6 (2014), 5, 87–98.

- S. J. Klebanoff "Myeloperoxidase: friend and foe" J. Leukoc. Biol. 77 (2005), 598–625.

- K. J. Koebke, F. Yu E. Salerno, C. Van Stappen, A. G. tebo, J. E. Penner-Hahn, V. L. Pecoraro "Modifying the Steric Properties in the Second Coordination Sphere of Designed Peptides Leads to Enhancement of Nitrite Reductase Activity" Angew. Chem. Int. Ed. 57 (2018), 3954–3957.

- I. K. Korendovych, W. F. DeGrado "De novo protein design, a retrospective" Cambrige University Press 53 (2020), e3.

- W. Krainer, A. Glieder "An updated view on horseradish peroxidases: recombinant production and biotechnological applications" Appl. Microbiol. Biotechnol., 99 (2015), 1611–1625.

- Y.-W. Lin "Rational Design of Artificial Metalloproteins and Metalloenzymes with Metal Clusters" Molecules 2019, 24, 2743.

- S. Isaac, J. H. Dawson "Haem iron–containing peroxidases" Essays Biochem. 34 (1999), 51–69.

- S. Itoh "Developing Mononuclear Copper–Active–Oxygen Complexes Relevant to Reactive Intermediates of Biological Oxidation Reactions" Acc. Chem. Res. 48 (2015), 2066–2074.

- S. C. Lee, W. Lo, R. H. Holm "Developments in the Biomimetic Chemistry of Cubane–Type and Higher Nuclearity Iron–Sulfur Clusters" Chem. Rev. 114 (2014), 3579–3600.

- L. Leone, D' D'Alonzo, V. Balland, G. Zambrano, M. Chino, F. Nastri, O. Maglio, V. Pavone, A. Lombardi "Mn–Mimochrome VI*a: an artificial metalloenzyme with peroxygenase activity" Front. Chem. 6 (2018), 590

- J. C. Lewis "Artificial Metalloenzymes and Metallopeptide Catalysts for Organic Synthesis" ACS Catal. 3 (2013), 2954–2975.

- Z. Li, B. Zhu, B. Wang, J. Gao, X. Fu, Q. Yao "Stress responses to trichlorophenol in Arabidopsis and integrative analysis of alteration in transcriptional profiling from microarray" Gene 555 (2015), 159–168.

- A. D. Liang, J. Serrano-Plana, R. L. Peterson, T. R. Ward "Artificial Metalloenzymes Based on the Biotin–Streptavidin Technology: Enzymatic Cascades and Directed Evolution" Acc. Chem. Res. 52 (2019), 585–595.

- R. Lichtenstein, T. A. Farid, G. Kodali, L. A. Solomon, J. L. R. Anderson, M. M. Sheehan, N. M. Ennist, B. A. Fry, S. E. Chobot, C. Bialas, J. A. Mancini, C. T. Armstrong, Z. Zhao, T. V. Esipova, D. Snell, S. A. Vinogradov, B. M. Discher, C. C. Moser, P. L. Dutton "Engineering oxidoreductases: maquette proteins designed from scratch." Biochem. Soc. Trans. 40 (2012), 561–566.

- Y. W. Lin, "Rational design of metalloenzymes: from single to multiple active sites" Coord. Chem. Rev. 336 (2017), 1–27.

- Liszkay, B. Kenk, P. Schopfer "Evidence for the involvement of cell wall peroxidase in the generation of hydroxyl radicals mediating extension growth" Planta, 217 (2003), 658–667.

- J. Z. Liu, T. L. Wang, L. N. Ji (2006) "Enhanced dye decolorization efficiency by citraconic anhydride– modified horseradish peroxidase" J. Mol. Catal. B Enzym. 41 (2006), 81–88.

- J. Liu, S. Chakraborty, P. Hosseinzadeh, Y. Yu, S. Tian, I. Petrik, A. Bhagi, Y. Lu "Metalloproteins containing cytochrome, iron–sulfur, or copper redox centers" Chem. Rev. 114 (2014), 4366–4469.

Chapter 1

- A. Lombardi, D. Marasco, O. Maglio, L. Di Costanzo, F. Nastri, V. Pavone "Miniaturized Metalloproteins: Application to Iron–Sulfur Proteins" Proc. Natl. Acad. Sci. 97 (2000), 11922–11927.

- A. Lombardi, F. Nastri, D. Marasco, O. Maglio, G. De Sanctis, F. Sinibaldi, R. Santucci, M. Coletta and V. Pavone "Design of a new mimochrome with unique topology" Chem.–Eur. J. 9 (2003), 5643–5654.

- A. Lombardi, F. Pirro, O. Maglio, M. Chino, W. F. DeGrado "De Novo Design of Four–Helix Bundle Metalloproteins: One Scaffold, Diverse Reactivities" Acc. Chem. Res. 5 (2019), 1148–1159.

- O. Maglio, F. Nastri, A. Lombardi "Structural and functional aspects of metal binding sites in natural and designed metalloproteins". Chapter 11 (2012) Ionic Interactions in Natural and Synthetic Macromolecules (Ciferri, A. and Perico, A., eds), 361–450.

- J.–P. Mahy, J. –D. Maréchal, R. Ricoux "From "hemoabzymes" to "hemozymes": towards new biocatalysts for selective oxidations" Chem. Commun. 51 (2015), 2476–2994.

- S. M. Mc Innis, R. Desikan, J. T. Hancock, S. J. Hiscock "Production of reactive oxygen species and reactive nitrogen species by angiosperm stigmas and pollen: potential signalling crosstalk?" New Phytol. 172 (2006), 221–228.

- Maki, U. Yugo, M. Yasushi, I. Isao "Preparation of peroxidase–immobilized polymers and their application to the removal of environment–contaminating compounds" Bull. Fib. Tex. Res. Found. 15 (2006), 15–19.

- M. Marques "Insights into porphyrin chemistry provided by the microperoxidases, the haempeptides derived from cytochrome c" Dalton Trans. 39 (2007), 4371–4385.

- S. E. Martinez, D. Huang, M. Ponomarev, W. A. Cramer, J. L. Smith "The heme redox center of chloroplast cytochrome f is linked to a buried five–water chain" Protein Sci. Publ. Protein Soc. 5 (1996), 1081–1092

- T. Matsuo, D. Murata, Y. Hisaeda, H. Hori, T. Hayashi "Porphyrinoid Chemistry in Hemoprotein Matrix: Detection and Reactivities of Iron(IV)-Oxo Species of

Porphycene Incorpporated into Horseradish Peroxidase" J. Am. Chem. Soc. 129 (2007), 12906− 12907.

- M. Matto, Q. Husain (2009) "Decolorization of textile effluent by bitter gourd peroxidase immobilized on concanavalin a layered calcium alginate–starch beads" J. Hazard. Mater. 164 (2009), 2–3,1540–1546.

- L. Meng, A. P. F. Turner, W. C. Mak "Positively–charged hierarchical PEDOT interface with enhanced electrode kinetics for NADH–based biosensors" Biosens. Bioelectron. 30 (2018), 120, 115–121.

- E. N. Mirts, I. D. Petrik, P.Hosseinzadeh, M. J. Nilges, Y. Lu "A designed heme–[4Fe–4S] metalloenzyme catalyzes sulfite reduction like the native enzyme" Science, 361 (2018), 6407, 1098–1101.

- S. Mocny, V. L. Pecoraro (2015) "De novo protein design as a methodology for synthetic bioinorganic chemistry" Acc. Chem. Res. 48 (2015), 2388– 2396

- T. Mogi, K. Saiki, Y. Anraku "Biosynthesis and functional role of haem O and haem A" Mol. Microbiol. 14 (1994), 391–398.

- Nakamura · I. Karube "Current research activity in biosensors" Anal. Bioanal. Chem. 377 (2003), 446–468.

- F. Nastri, A. Lombardi, G. Morelli, O. Maglio, G. D'Auria, C. Pedone, V. Pavone "Hemoprotein Models Based on a Covalent Helix–Heme–Helix Sandwich: 1. Design, Synthesis, and Characterization" Chem. Eur. J. 3 (1997), 340–349.

- F. Nastri, L. Lista, P. Ringhieri, R. Vitale, M. Faiella, C. Andreozzi, P. Travascio, O. Maglio, A. Lombardi, V. Pavone "A heme–peptide metalloenzyme mimetic with natural peroxidase– like activity" Chemistry, 17 (2011), 4444–4453.

- F. Nastri, M. Chino, O. Maglio, A. Bhagi–Damodaran, Y. Lu, A. Lombardi Design and engineering of artificial oxygen–activating metalloenzymes. Chem. Soc. Rev. 45 (2016), 5020–5054.

- F. Nastri, D. D'Alonzo, L. Leone, G. Zambrano, V. Pavone, A. Lombardi "Engineering Metalloprotein Functions in Designed and Native Scaffolds" Trends Biochem. Sci. 44 (2019), 12, 1022–1040.

- S. N. Natoli, J. F. Hartwig "Noble-metal substitution in hemoproteins: an emerging strategy for abiological catalysis" Acc. Chem. Res. 52 (2019), 2, 326-335

- S. L. Newmyer, P. R. Ortiz de Motellano "Horseradish peroxidase His42–Ala, His42–Val, and Phe41–Ala mutants" J. Biol. Chem. 270 (1995), 19430–19438.

- W. N. Oloo, L. Que, Jr., Comprehensive Inorganic Chemistry II, 2nd edition (2013), 763.

- K. Oohora, H. Meichin, L. M. Zhao, M. W. Wolf, A. Nakayama, J. Hasegawa, N. Lehnert, T. Hayashi "Catalytic Cyclopropanation by Myoglobin Reconstituted with Iron Porphycene: Acceleration of Catalysis Due to Rapid Formation of the Carbene Species" J. Am. Chem. Soc. 139 (2017), 17265−17268.

- K. Oohora, A. Onoda, T. Hayashi "Hemoproteins reconstituted with artificial metal complexes as biohybrid catalysts" Acc. Chem. Res. 52 (2019), 945–954

- K. G. Paul "Die isolierung von meerrettichperoxydase" Acta Chem. Scand. 12 (1958), 1312–1318.

- D. Petrik, J. Liu, Y. Lu "Metalloenzyme design and engineering through strategic modifications of native protein scaffolds" Curr. Opin. Chem. Biol. 19 (2014), 67–75

- Q. Raffy, R. Ricoux, E. Sansiaume, S. Pethe and J.–P. Mahy "Coordination chemistry studies and peroxidase activity of a new artificial metalloenzyme built by the "Trojan horse" strategy" J. Mol. Catal. A Chem. 317 (2010), 19–26.

- T. L. Poulos, J. Kraut "The stereochemistry of peroxidase catalysis" J. Biol. Chem. 255 (1980), 8199–8205.

- T. L. Poulos "Heme Enzyme Structure and Function" Chem. Rev. 114 (2014), 7, 3919–3962.

- J. Reedy, B. R. Gibney "Heme Protein Assemblies" Chem. Rev. 104 (2004), 617–650.

- J. Reig, M. M. Pires, R. A. Snyder, Y. Wu, H. Jo, D. W. Kulp, S. E. Butch, J. R. Calhoun, T. Szyperski, E. I. Solomon, W. F. DeGrado "Alteration of the oxygen–dependent reactivity of de novo Due Ferri proteins" Nat. Chem. 4 (2012), 11, 900–906.

- R. Ricoux, H. Sauriat–Dorizon, E. Girgenti, D. Blanchard and J.–P. Mahy "Hemoabzymes: towards new biocatalysts for selective oxidations" J. Immunol. Methods 269 (2002), 39–57.

- N. Rodríguez–López, A. T. Smith, R. N. F. Thorneley "Recombinant horseradish peroxidase isoenzyme C: the effect of distal haem cavity mutations (His42–Leu and Arg38–Leu) on Compound I formation and substrate binding" J. Biol. Inorg. Chem. 1 (1996), 136–142.

- A. Roy, D. J. Sommer, R. A. Schitz, C. L. Brown, D. Gust, A. Astashkin, G. Ghirlanda "A De Novo Designed 2[4Fe-4S] Ferredoxin Mimic Mediates Electron Transfer" J. Am. Chem. Soc. 136 (2014), 17343–17349.

- V. Rumbau, Rebeca Marcilla, E. Ochoteco, J. A. Pomposo, D. Mecerreyes "Ionic Liquid Immobilized Enzyme for Biocatalytic Synthesis of Conducting Polyaniline" Macromolecules, 39 (2006), 25, 8547−8549.

- V. Rumbau, J. A. Pomposo, A. Eleta, J. Rodriguez, H. Grande, D. Mecerreyes, E. Ochoteco "First Enzymatic Synthesis of Water–Soluble Conducting Poly(3,4–ethylenedioxythiophene)" Biomacromolecules, 8 (2007), 2, 315–317.

- M. I. Savenkova, J. M. Kuo, P. R. Ortiz de Montellano "Improvement of Peroxygenase Activity by Relocation of a Catalytic Histidine within the Active Site of Horseradish Peroxidase" Biochemistry (Mosc.), 37 (1998), 10828–10836.

- F. Schubert, S. Saini, A. P. F. Turner "Mediated amperometric enzyme electrode incorporating peroxidase for the determination of hydrogen peroxide in organic solvents" Anal. Chim. Acta 245 (1991), 133-138.

- F. Schwizer, Y. Okamoto, T. Heinisch, Y. Gu, M. M. Pellizzoni, V. Lebrun, R. Reuter, V. Köhler, J. C. Lewis, T. R. Ward "Artificial Metalloenzymes: Reaction Scope and Optimization Strategies" Chem. Rev. 118 (2018), 142–231.

- N. Sekretaryova, M. Eriksson, A. P. F. Turner "Bioelectrocatalytic systems for health applications" Biotechnol. Adv. 34 (2016), 177–197.

- L. M. Shannon, E. Kay, J. Y. Lew "Peroxidase isozymes from horseradish roots. I. Isolation and physical properties." J. Biol. Chem. 241 (1996), 2166–2172.

- Y. Sheng, K. Wang, Q. Lu, P. Ji, B. Liu, J. Zhu, Q. Liu, Y. Sun, J. Zhang, E.-M. Zhou, Q. Zhao "Nanobody-horseradish peroxidase fusion protein as an ultrasensitive probe to detect antibodies against Newcastle disease virus in the immunoassay" J. Nanobiotechnol 17 (2019), 35.

- S. S. Sibbett, J. K. Hurst "Structural analysis of myeloperoxidase by resonance Raman spectroscopy" Biochemistry (Mosc.) 23 (1984), 3007–3013.

- J. A. Sigman, H. K. Kim, X. Zhao, J.R. Carey, and Y. Lu "The role of copper and protons in heme–copper oxidases: Kinetic study of an engineered heme–copper center in myoglobin" Proc. Natl. Acad. Sci. USA 100 (2003), 7, 3629–3634.

- L. J. Smith, A. Kahraman, J. Thornton "Heme proteins–Diversity in structural characteristics, function, and folding" Proteins 78 (2010), 2349–2368.

- Tripathy, I. Sherameti, R. Oelmüller "Siroheme: an essential component for life on earth." Plant Signal. Behav. 5 (2010), 14–20.

- Y. Valasatava, A. Rosato, N. Furnham, J. M. Thornton, C. Andreini "To what extent do structural changes in catalytic metal sites affect enzyme function?" J. Inorg. Biochem. 179 (2018), 40–53.

- K. Vainshtein, W. R. Melik–Adamyan, V. V. Barnynin, A. A. Vagin, A. I. Grebenko, V. V. Borisov, K. S. Bartels, I. Fita, M. G. Rossmann "Three–dimensional structure of catalase from Penicillium vitale at 2.0 A resolution" J. Mol. Biol. 188 (1986), 49–61.

- P. T. Vasudevan, L. O. Li, L. O. "Peroxidase catalyzed polymerization of phenol" Appl. Biochem. Biotechnol. 60 (1996), 1, 73–82.

- N. C. Veitch, A. T. Smith "Horseradish peroxidase" Adv. Inorg. Chem. 51 (2000), 107–162.

- N. C. Veitch "Horseradish peroxidase: a modern view of a classic enzyme" Phytochemistry 65 (2004), 249–259.

- Vitale, R. (2013). Developing metalloprotein models for diagnostic and sensing applications. PhD Thesis in Chemical Sciences, XXV Cycle.

- R. Vitale, L. Lista, C. Cerrone, G. Caserta, M. Chino, O. Maglio, F. Nastri, V. Pavone, A. Lombardi "An artificial heme–enzyme with enhanced catalytic activity: evolution, functional screening and structural characterization" Org. Biomol. Chem. 13 (2015), 4859–4868.

- H. Watanabe, A. Satake, Y. Kido, A. Tsuji "Monoclonal-based enzyme-linked immunosorbent assay and immunochromatographic assay for enrofloxacin in biological matrices" Analyst 127 (2002), 92-103.

- K. G. Welinder "Covalent structure of the glycoprotein horseradish peroxidase (EC 1.11.1.7)" FEBS Lett. 72 (1976), 19–23.

- Werck–Reichhart, R. Feyereisen "Cytochromes P450: a success story". Genome Biol. 1 (2000), 6.

- R. Wilson, A. P. F. Turner "Glucose oxidase: an ideal enzyme" Biosens. Bioelectron 7 (1992), 3, 165–185.

- C. W. Wood, M. Bruning, A. Á, Ibarra, G. J. Bartlett, A. R. Thomson, R. Sessions, R. L. Brady, D. N. Woolfson "CCBuilder: An Interactive Web-Based Tool for Building, Designing and Assessing Coiled-Coil Protein Assemblies" Bioinformatics, 30 (2014), 3029-3035.

- G. Xing, V. J. DeRose "Designing Metal–Peptide Models for Protein Structure and Function" Curr. Opin. Chem. Biol. 5 (2001), 196–200.

- T. Xu, T. J. Zhao, P. Hu, Z. Dong, J. Li, H. Zhang, D. Yin, Q. Zhao," Pentachlorophenol exposure causes Warburg–like effects in zebrafish embryos at gastrulation stage" Toxicol. Appl. Pharmacol. 277 (2014), 183–191.

- H. Yang, C. Gong, L. Miao, F. Xu "A glucose biosensor based on horseradish peroxidase and glucose oxidase co-entrapped in carbon nanotubes modified electrode" Int. J. Electrochem. Sci. 12 (2017), 4958-4969.

- L. Yin, H. Yuan, C. Liu, B. He, S.-Q. Gao, G.-B. Wen, X. Tan, Y.-W. Lin "A Rationally Designed Myoglobin Exhibits a Catalytic Dehalogenation Efficiency More than 1000-Fold That of a Native Dehaloperoxidase" ACS Catal. 8 (2018) 9619–9624.

- F. Yu, V. M. Cangelosi, M. L. Zastrow, M. Tegoni, J. S. Plegaria, A. G. Tebo, C. S. Mocny, L. Ruckthong, H. Qayyum, V. L. Pecoraro "Protein Design: Toward Functional Metalloenzymes" Chem. Rev. 114 (2014), 3495–3578.

- Y. Yu, C. Hu, L. Xia. J. Wang "Artificial metalloenzyme design with unnatural amino acids and non–native cofactors" ACS Catal. 8 (2018), 1851–1863.

- M. Zamocky, P. G. Furtmüller, C. Obinger "Evolution of Catalases from Bacteria to Humans" Antioxid. Redox Signal. 10 (2008), 9, 1527–1548.

- M. L. Zastrow, V. L. Pecoraro "Designing functional metalloproteins: from structural to catalytic metal sites" Coord. Chem. Rev. 257 (2013), 2565–2588.

- S.-Q. Zhang, M. Chino, L. Liu, Y. tang, X. Hu, W. F. DeGrado, A. Lombardi "De Novo Design of Tetranuclear Transition Metal Clusters Stabilized by Hydrogen-Bonded Networks in Helical Bundles" J. Am. Chem. Soc. 140 (2018), 1294–1304.

- J. Zhao, C. Lu, S. Franzen "Distinct Enzyme–Substrate Interactions Revealed by Two Dimensional Kinetic Comparison between Dehaloperoxidase–Hemoglobin and Horseradish Peroxidase" J. Phys. Chem. B 119 (2015), 40, 12828–12837.

- Y. Zhou, H. Xu, H. Wang, B.-C. Ye "Detection of breast cancer-derived exosomes using the horseradish peroxidase-mimicking DNAzyme as an aptasensor" Analyst 145 (2020), 107-114.

This page was intentionally left blank

Chapter 2

Synthetic peroxidases in halophenols dehalogenation and bioremediation

2.1 Introduction

2.1.1 Peroxidases as bioremediation tools

Halophenols (HPs), such as pentachlorophenol (PCP) [Guyton, K. et al. (2016)] and 2,4,6–trichlorophenol (TCP) [Huff, J. (2012)] have been widely used as preservatives for wood and leather and as building–blocks in pesticide, herbicide, drugs and dyes synthesis for more than 100 years. This class of compounds (Figure 2.1) is recalcitrant to degradation, as only a few species of microorganisms can metabolize them [Arora, P. K. and Bae, H. (2014)].
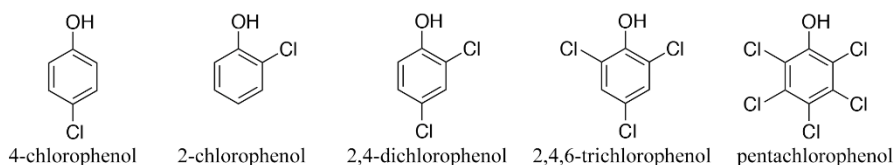
Figure 2.1. Structure of some HPs

Over the years an increased release of these compounds into the environment has been observed, with consequent accumulation and contamination of soils and waters. The toxic effects of HPs on plants, animals and human are widely reported in the literature, involving reduced growth of roots in A*rabidopsis thaliana*, leukemias and lymphomas in mammals [Xu, T. et al. (2014); Li, Z. et al. (2015); Fernandez Freire, P. et al. (2005); Huff, J. (2012)]. In the frame of sustainable bioremediation strategies, enzymes have been proposed as a useful tool to remove these substances from waters and soils [Fukushima, M. et al. (2009)]. Among the wide portfolio of enzymes, heme peroxidases have already proven to convert phenols and HPs with high efficiency. In the case of HRP and some other peroxidases [Osborne, R. L. et al. (2006)] the conversion of HPs with variable substitution degree leads to polymers (either soluble or insoluble) and/or benzoquinones [Vasudevan, P. T. and Li, L. O. (1996)].

Heme peroxidases have already been used in HPs bioremediation strategies. Examples of their practical applications along with heme–based supramolecular

catalysts for HPs bioremediation have already been reported.

A first example [Lai, Y. C. and Lin, S. C. (2004)] reports the use of HRP supported onto a solid matrix. In detail, they used aminopropyl functionalized porous glass to immobilize HRP by glutaraldehyde coupling. The supported enzyme was then exposed to a solution of 4–chlorophenol and hydrogen peroxide. HRP caused the polymerization of 4–chlorophenol into insoluble precipitate within 3 hours with a removal efficiency of 25%, only.

An alternative approach is provided by Morimoto and coworkers [Morimoto, K. and Tatsumi, K. (1997)], which copolymerized toxic PCP with p–hydroxybenzoic and coumaric acids, using HRP as catalyst. The addition of p–hydroxybenzoic and coumaric acids to the HRP–hydrogen peroxide–PCP mixture, not only avoided the formation of toxic octachlorodibenzo–p–dioxin (common peroxidase product of PCP), but also depleted PCP from water with a removal efficiency of 90%, entrapping toxic PCP into HRP–synthesized co–polymer.

Another approach involved the use of simple iron porphyrins along with humic acids (HA) from soils [Fukushima, M. et al. (2003)]. HA are part of the organic matter commonly found in soil, waters and sediments (Figure 2.2).
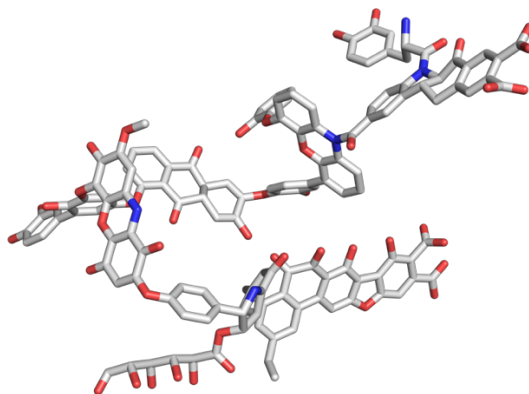
Figure 2.2. Example of 3D model structure of HA

Their chemical structure is highly variable and it usually comprises sugars and aromatic moieties exposing phenolic, cathecolic, quinoid and carboxylic groups [Gomes de Melo, B. A. et al. (2016)]. In the development of a bioremediation process, these substances act as inexpensive supports entrapping phenols and HPs, reducing leachability, toxicity, and bioavailability of the pollutant. The entrapment mediated by HA can be either due to hydrophobic or π/π interactions between the polymerized pollutant with HA or due to covalent linkage of activated pollutants on HA [Eibes, G. et al. (2015)].

Some examples also report the use of HRP in combination with HA for 2,6–dichlorophenol removal in the presence of hydrogen peroxide [Palomo, M. and Bhandari, A. (2010)] and non–halogenated phenols such as phenol, methylphenol, naphtol and o–cresol [Bhandari, A. and Xu, F. (2001); Eibes, G. et al. (2015)].

2.1.2 Reactivity of natural and synthetic heme peroxidases towards HPs

An example of the reactivity of heme peroxidases in the oxidative dehalogenation of HPs is reported by Osborne and coworkers [Osborne, R. L. et al. (2009)]. They describe the interesting activity of dehaloperoxidase (DHP) from a marine worm *Amphitrite Ornata*. DHP, existing in two isoforms A and B, shares structural similarities with globins (e.g. myoglobin), such as the arrangement of the helices and functional features of the distal histidine (His55). The His55 conformational changes (in and out of the distal pocket) resemble those observed in the globin family for the regulation of binding affinity to molecular oxygen [de Serrano, V. et al. (2007); Thompson, M. K. et al. (2010); Franzen, S. et al. (2012)].

In contrast to well–studied plant peroxidases, where the proximal His residue, due to the strong hydrogen bond to an Asp residue sidechain, is mostly in the

imidazolate form, DHP shares a weak hydrogen bond between the proximal histidine and the backbone carbonyl of Leu83 residue, similarly to myoglobin. The X–ray structure of DHP revealed that the His55 assumes two conformations: closed and open (Figure 2.3).
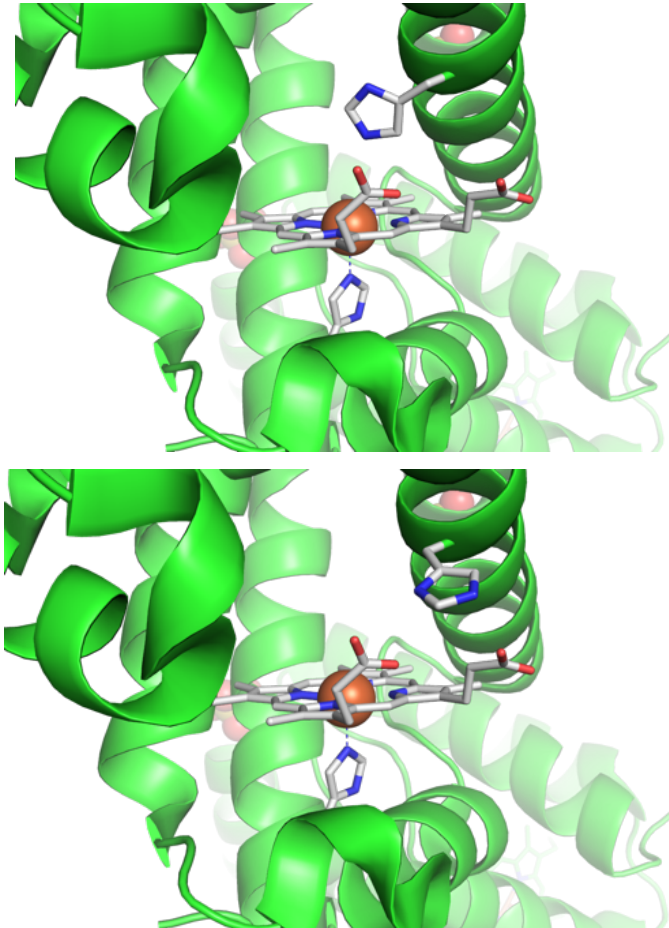
Figure 2.3. X–ray crystal structure (resolution 1.78 Å) of DHP. Top: "closed" conformation Bottom: "open" conformation with His55 exposed to solvent (PDB: 1EW6).

The closed conformation shows the His55 inside the distal pocket, thus placing it in proximity of exogenous ligands (such as O_2 or H_2O_2), bound to the heme. On

the contrary, the "open" conformation shows the His55 pointing away from the heme center and exposed to the solvent [de Serrano, V. et al. (2007)].

Moreover, substrate binding site also differs from peroxidases, as DHP demonstrated to bind halophenols above the heme rather than at an heme edge (Figure 2.4), as observed for HRP [Osborne, R. L. et al. (2004); Osborne, R. L. et al. (2009)]. The flexibility of His55 in and out of DHP active site is increased compared to that of other globins [Chen, Z. et al. (2008)]. X–ray crystal structures also highlight that in the presence of monohalogenated inhibitor (e.g. 4–bromophenol), His55 is displaced out of the distal pocket (open conformation) thus impeding hydrogen peroxide activation and inhibiting substrate conversion [Thompson, M. K. et al. (2010)]. Instead, in the presence of trihalogenated phenol substrate, His55, located above the active site (closed conformation), participates in the activation of hydrogen peroxide in order to generate Compound I, thus enabling the formation of dihalogenated quinone [Plummer, A. et al. (2013)].

This is a two–site competitive inhibition in which the active site switches between peroxide inhibition and peroxide activation.
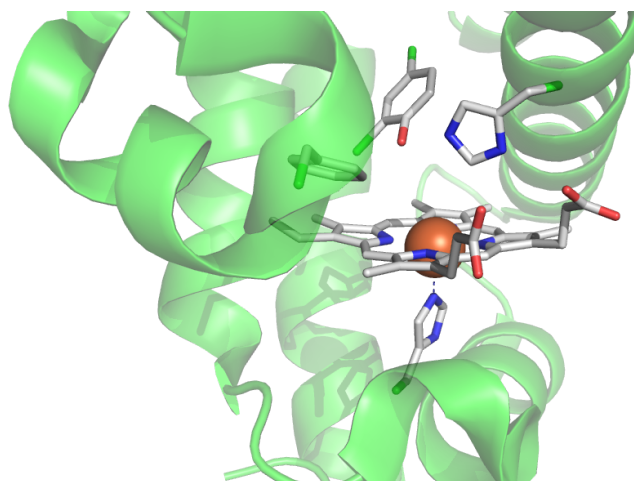
Figure 2.4. X–ray crystal structure (resolution 1.85Å) of the halophenol binding pocket in DHP B (PDB code: 6I7F)

The extensive research on DHP has led to a deep understanding on the mechanism undergoing the conversion of HPs to benzoquinone analogues.

As shown in Figure 2.5, the first step involves the formation of a high valent iron–oxo species, which then is brought back to resting state by two single electron steps with the HP substrate.
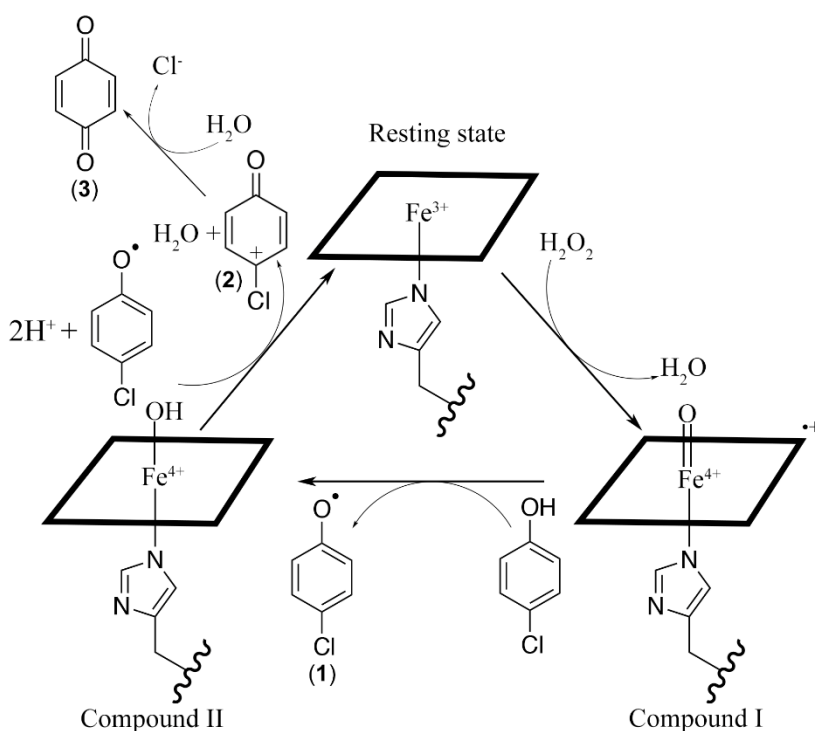
Figure 2.5. Catalytic cycle undergoing the oxidative dehalogenation of 4–chlorophenol

In particular, in the mechanism proposed by Osborne and coworkers, [Sumithran, S. et al (2012); Osborne, R. L. et al. (2009)] 4–chlorophenol undergoes a first one–electron oxidation, producing a phenoxyradical species (**1**). Then, a second one–electron oxidation on the phenoxyradical yields a

positively charged ring (**2**), that is readily converted into benzoquinone (**3**) after reaction with a water molecule. At this stage the chloride ion is released.

A similar mechanism involving two single electron steps and formation of phenoxyradical intermediate is also described for HRP [Sumithran, S. et al. (2012)].

The catalytic parameters of natural peroxidases for oxidative dehalogenation are listed in Table 2.1. For the kinetic characterization, TCP was chosen as model substrate.

Table 2.1. Catalytic parameters calculated for natural peroxidases

	Enzyme	K_m^{TCP} (M)	K_m^{H2O2} (M)	k_{cat} (s^{-1})	k_{cat}/K_m^{TCP} $(M^{-1}\,s^{-1})$	k_{cat}/K_m^{H2O2} $(M^{-1}\,s^{-1})$
1	**DHP A a**	$2.07 \cdot 10^{-3}$	$3.35 \cdot 10^{-4}$	13.67	$6.60 \cdot 10^{3}$	$4.08 \cdot 10^{4}$
2	**DHP B** [a]	$6.85 \cdot 10^{-4}$	$1.65 \cdot 10^{-4}$	25.72	$3.75 \cdot 10^{4}$	$1.56 \cdot 10^{5}$
3	**HRP** [b]	$5.40 \cdot 10^{-3}$	$5.0 \cdot 10^{-5}$	571.3	$1.06 \cdot 10^{5}$	$1.14 \cdot 10^{7}$

[a][enzyme] = $2.4 \cdot 10^{-6}$ M; 100 mM phosphate buffer pH 7.0. [b][enzyme] = $2 \cdot 10^{-7}$ M; 100 mM phosphate buffer pH 7.0 Data reported in [J. Zhao et al. (2015)]

The oxidative dehalogenation catalysis has been reproduced in artificial systems. An example is represented by the thermostable *c*–type cytochrome *maquette* (CTM C45), *de novo* designed by Anderson and coworkers (Figure 2.6), which bound heme within a four–helix bundle structure [Watkins, D. et al. (2017)]. The enzyme exhibited substrate promiscuity as it was able to catalyze both ABTS oxidation and TCP dehalogenation with excellent catalytic efficiencies. In particular, the kinetic characterization over TCP highlights a low k_{cat} value ($k_{cat} = 0.5$ s^{-1}) and an excellent affinity of CTM C45 in TCP binding ($K_m^{TCP} = 1.2 \cdot 10^{-5}$ M) which positively impacts on the catalytic efficiency (k_{cat}/K_m^{TCP} $4.17 \cdot 10^{4}$ M^{-1} s^{-1}) (see Table 2.5).
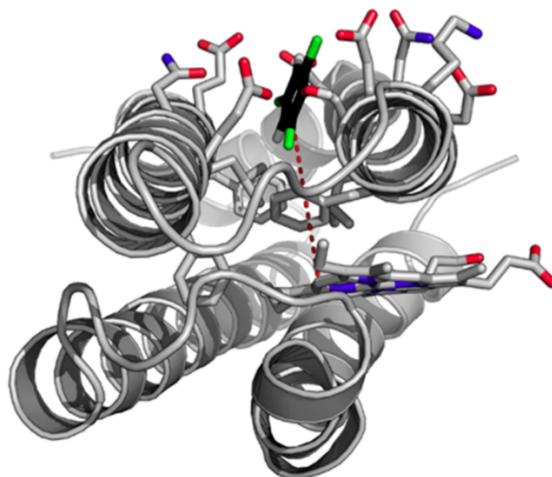
Figure 2.6. Model structure of the C45 (CTM C45) / TCP complex. Reproduced with permission from [Watkins, D. et al. (2017)].

More recently, with a different approach, Lin and coworkers redesigned the heme center of myoglobin (Mb), combining the structural features of *Caldariomyces fumago* chloroperoxidase (CCPO) with those of DHP [Yin, L. et al. (2018)]. The mutation F43Y/H64D installed a new function into Mb, transforming a pure dioxygen binding heme protein into an efficient catalyst for oxidative dehalogenation (Figure 2.7).
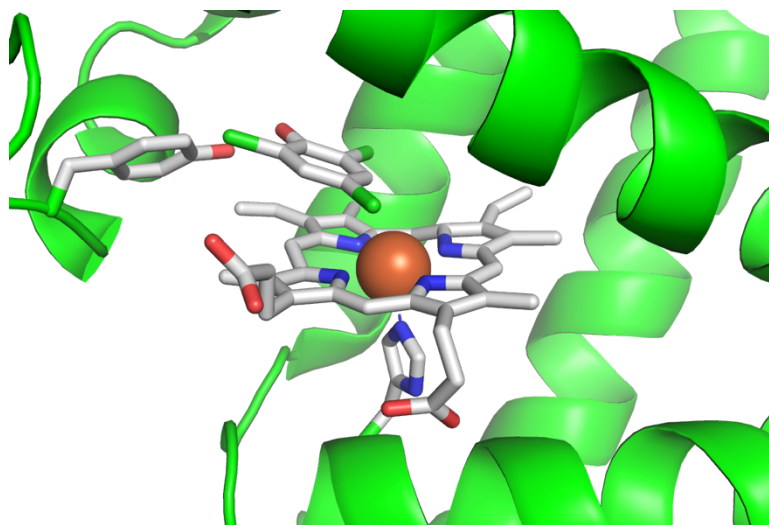
Figure 2.7. X–ray structure of F43Y/H64D Mb (PDB ID: 5ZZG)

The obtained mutant exhibited even lower K_m^{TCP} values ($3.5 \cdot 10^{-6}$ M $\pm$ $3 \cdot 10^{-7}$) and higher k_{cat} of 27.5 s^{-1} in comparison with CTM C45, resulting in the highest efficiency ever reported for TCP oxidative dehalogenation (k_{cat}/K_m^{TCP} $7.86 \cdot 10^{6}$ M^{-1} s^{-1}) (see Table 2.5).

Competent catalysts for TCP oxidative dehalogenation were successfully obtained by design and engineering approaches. In particular, these approaches yielded enzymes with good performances, overcoming, in the case of F43Y/H64D, that of natural HRP. However, both the engineered F43Y/H64D Mb and the *de novo* designed CTM C45, show low k_{cat} values, which hinder practical applications of these catalysts.

In an effort to capture the behavior of natural metalloproteins into artificial molecules, and taken into accounts the high catalytic versatility and enhanced performances of the synthetic heme-protein FeMC6*a, we explored its catalytic potential toward TCP oxidation.

Furthermore, a preliminary analysis on the catalytic properties of this synthetic peroxidase in oxidative degradation of TCP in presence of humic acids was

performed, for testing its application in the bioremediation of phenolic compounds from wastewaters.

2.2 Results and discussion

2.2.1 Catalytic activity of FeMC6*a towards TCP

The catalytic activity of FeMC6*a towards TCP, chosen as model substrate was evaluated. This substrate was used to define optimal experimental conditions (solvent and pH) in oxidative dehalogenation and to determine kinetic parameters such as the k_{cat} and the K_m.

2.2.1.1 Oxidation of TCP

A schematic representation of oxidative dehalogenation of TCP catalyzed by FeMC6*a is shown in Fig. 2.8. This reaction leads to the formation of 2,6–dichlorobenzoquinone (DBQ) without further oxidation and/or polymerization products.
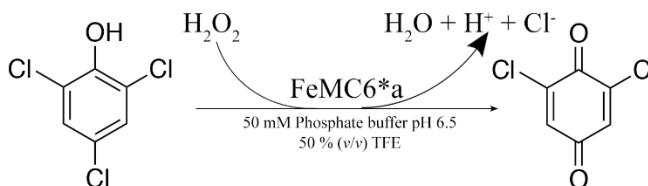
Figure 2.8. Catalytic transformation of TCP into DBQ

A first screening for the catalytic activity was performed under optimal experimental conditions used for ABTS oxidation catalyzed by FeMC6*a (50 mM phosphate buffer pH 6.5, 50%(v/v) 2,2,2–trifluoroethanol (TFE), at 25 °C), [Caserta, G. et al. (2018)]. The reaction was monitored by continuous UV–Vis scanning in the 200–800 nm region.
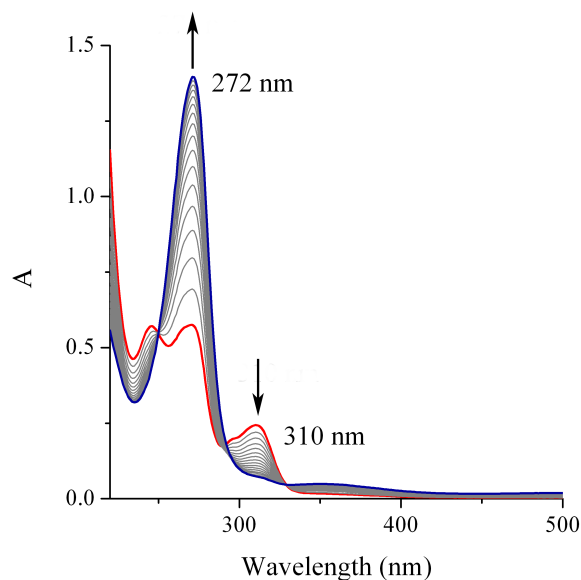
Figure 2.9. UV−vis spectra of FeMC6*a (0.1μM) in the presence of TCP (100 μM) in 50 mM sodium phosphate (pH 6.5) with 50%(*v/v*) TFE upon addition of H_2O_2 (400 μM). The spectrum before H_2O_2 addition is marked as red. The blue line shows the spectrum after 15 min from H_2O_2 addition. The spectra were collected each 60 s at 25 °C.

Figure 2.9 shows the UV–Vis profile of the TCP oxidation catalyzed by FeMC6*a.

The addition of H_2O_2 to a solution of TCP containing FeMC6*a led to the disappearance of the band at 310 nm assigned to TCP and to the concurrent appearance of a band at 272 nm consistent with DBQ absorption profile, as observed for natural peroxidases. Two isosbestic points at λ=250 nm and λ=329 nm suggest a direct conversion of TCP substrate into DBQ product. Analogously with other peroxidases, H_2O_2 triggers the oxidative dehalogenation reaction by forming high-valent metal oxo species, which is then reduced back to resting state using TCP as electron-donor, as reported for HRP and DHP [Sumithran, S. et al (2012); Osborne, R. L. et al. (2009)].

Control reaction in absence of catalyst was also performed, which showed no DBQ formation, confirmed either by UV–Vis spectroscopy and GC–MS analysis (data not shown).

2.2.1.2 Product identification

After 15 minutes from hydrogen peroxide addition, a GC–MS analysis was carried out. The reaction mixture was acidified with water 0.1% (*v/v*) TFA, extracted with dichloromethane (DCM) and analyzed by GC–MS. Figure 2.10 reports the TIC chromatogram obtained.
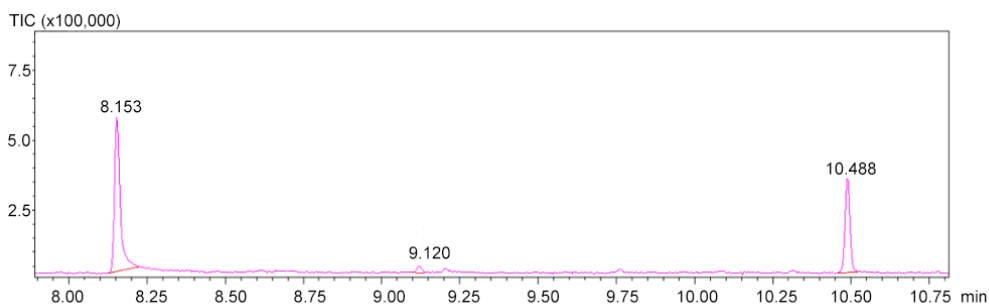
Figure 2.10. GC–MS profile of TCP– FeMC6*a mixture after 15 min from H_2O_2 addition.

The electron impact–mass spectrometry (EI–MS) spectra of products eluted at 8.153, 9.120 min and 10.488 are reported in Figure 2.10a, 2.10b and 2.10c, respectively.
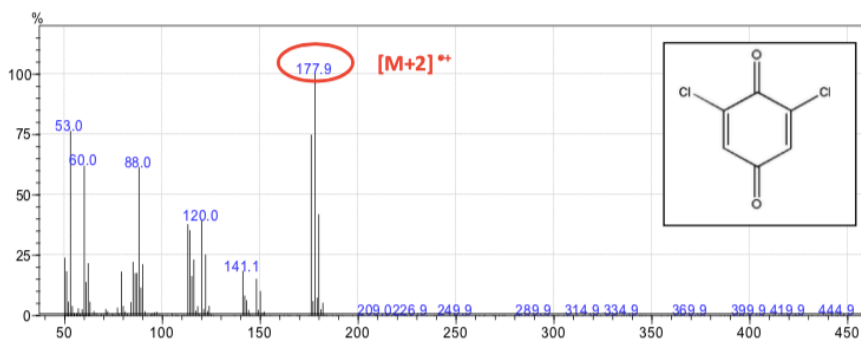
Figure 2.10a. Mass spectrum of DBQ at R_t 8.153 min; $[M+2]^{•+}$ = 177.9 amu.
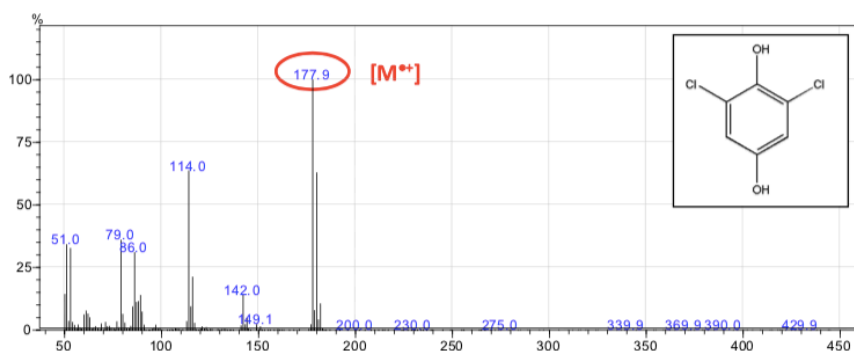
Figure 2.10b. Mass spectrum of 2,6–dichlorohydroquinone (DHQ) at R_t 10.488 min; $[M]^{\bullet+}$ =179.9 amu.
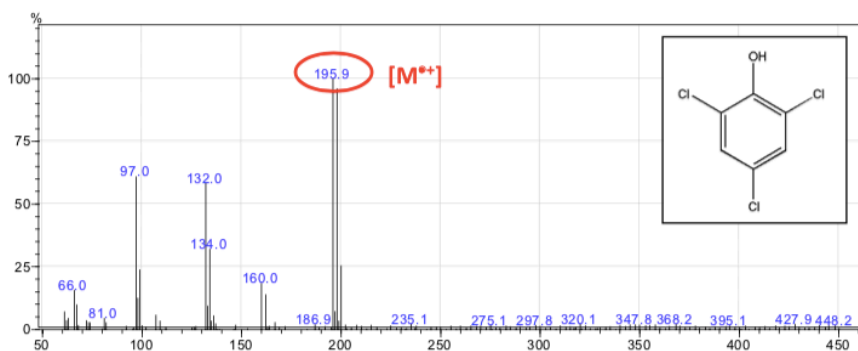
Figure 2.10c. Mass spectrum of TCP at R_t 9.120 min; $[M]^{\bullet+}$ = 195.9 amu.

GC-MS analysis shows the presence of the product in both reduced (DHQ) and oxidized (DBQ) form due to an independent equilibrium of DBQ, possibly related to reduction during mass anaylsis, as reported in literature [Qin, F. et al. (2010); Pei, J. et al. (2018)] and confirmed by control experiments with standard DBQ in the same buffer used in the experiments (data not shown). These results prove that FeMC6*a is able to transform TCP to its quinone analogue DBQ similarly to natural peroxidases HRP and DHP.

2.2.2 **Functional Screening: optimal reaction conditions assessment**

To gain more insights on the catalytic performances of FeMC6*a toward HPs oxidation, the influence of pH, and of the helix–inducing solvent TFE [Roccatano, D. et al. (2002)] was studied.

First, the influence of TFE on catalysis was evaluated. At fixed TCP, H_2O_2 and enzyme concentrations (250 μM, 250 μM and 63 nM, respectively), the initial rates for TCP oxidation were extrapolated. All catalytic assays were performed in 50 mM sodium phosphate buffer pH 6.5 at different percentages of TFE (v/v).
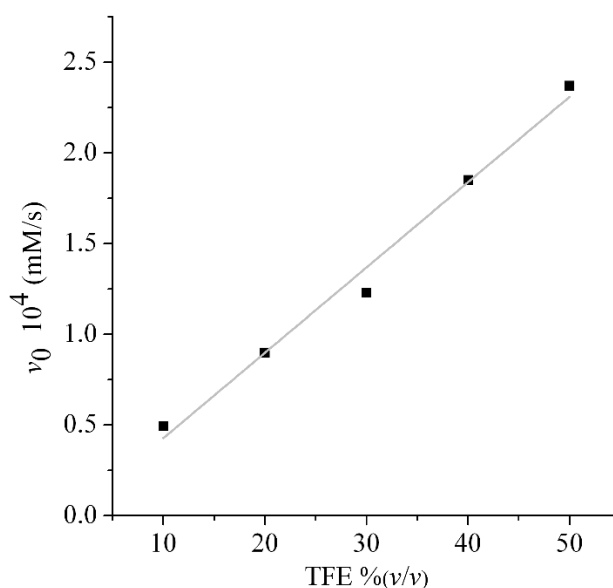
Figure 2.11. Initial rates of TCP oxidation as a function of %TFE (v/v). Experimental conditions: [TCP] = 250 μM, [H_2O_2] = 250 μM, [enzyme] = 63 nM, in 50 mM sodium phosphate buffer pH 6.5. TFE range 0–50 %(v/v).

Figure 2.11 shows the initial rates (expressed as mM/s), determined from the absorbance change at $\lambda=272$ nm during the reaction progress, as function of TFE from 10 to 50 %(v/v). Analogously to what observed for ABTS oxidation [Caserta, G. et al. (2018)] a linear increase in initial rate of reaction was

observed with increasing concentration of TFE, confirming the positive impact of secondary structure in FeMC6*a and its assistance in the catalysis.
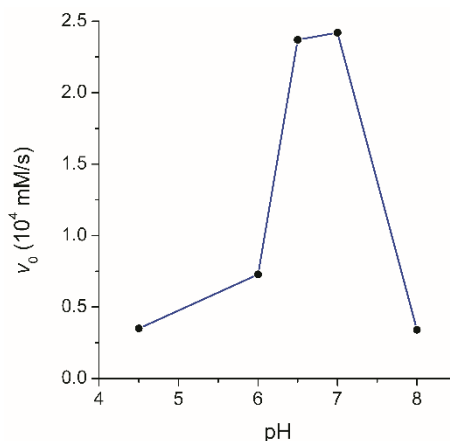
Figure 2.12. Initial rates of TCP oxidation as a function of pH. Experimental conditions: [TCP] = 250 μM, [H$_2$O$_2$] = 250 μM, [FeMC6*a] = 63 nM, in 50 mM buffers (acetate pH 4.5; phosphate pH 6.0, 6.5, 7.0; carbonate pH 8.0) with 50 %(v/v) TFE.

Similar experiments were carried out by varying pH, using buffers with 50%(v/v) TFE and containing a fixed concentration of TCP, H$_2$O$_2$ and enzyme (250 μM, 250 μM and 63 nM, respectively), evaluating the initial rates for TCP oxidation.

Figure 2.12 shows the initial reaction rate (expressed as mM/s) for TCP oxidation reported as function of pH (ranging from 4.5 to 8.0). As for ABTS [Caserta, G. et al. (2018)], best performances were observed in a narrow pH range (6.5–7.0).

Both TFE and pH dependence on the initial rates confirm that optimal catalytic conditions are 50 %(v/v) TFE in phosphate buffer pH 6.5, well retained compared to previous characterizations with other substrates.

2.2.3 **Kinetic parameters: k_{cat} and K_m**

Kinetic parameters such as k_{cat} and Michaelis–Menten constant (K_m) for both substrates, H_2O_2 and TCP, were determined in optimal conditions for catalysis. Initial rates (v_0) were plotted against concentration of the variable substrate and fitted with a two-substrates Michaelis–Menten equation (Equation 1).

$$v = \frac{[E]_0}{\frac{1}{k_{cat}} + \frac{K_{M(TCP)}}{k_{cat}[TCP]} + \frac{K_{M(H2O2)}}{k_{cat}[H2O2]}} \quad \text{(Equation 1)}$$
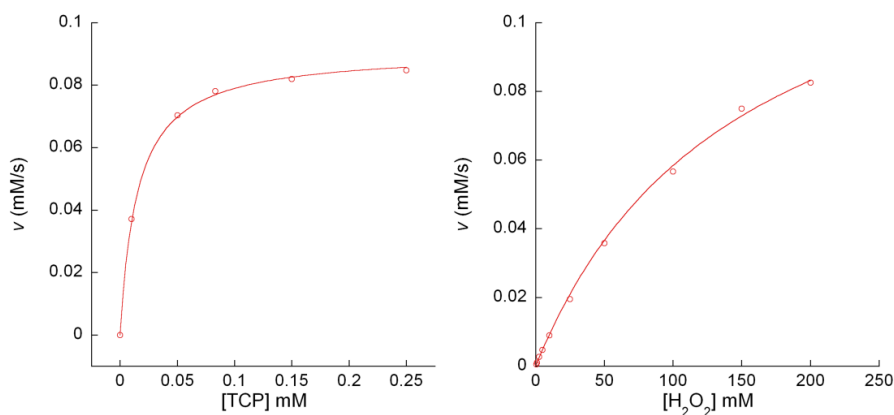
Figure 2.13. Catalytic activity of FeMC6*a in the presence of 50 %(v/v) TFE. **LEFT** Initial rate dependence towards TCP concentration (0.0100–0.25 mM range). **RIGHT** Initial rate dependence towards H_2O_2 concentration (0–200 mM range).

The two sets of data were acquired by keeping one of the two substrates concentration constant by varying the other and *vice versa*. In particular, TCP was in the range 0.0100–0.250 mM with 300 mM fixed concentration of

hydrogen peroxide. Alternatively, hydrogen peroxide was in the range 0.500–200 mM with 0.250 mM fixed concentration of TCP (Figure 2.13). Enzyme concentration in all assays was fixed at 63.0 nM.

The catalytic parameters obtained are listed in Table 2.2.

Table 2.2. Catalytic parameters calculated for FeMC6*a in 50 mM phosphate buffer pH 6.5 with 50% (*v/v*) TFE.

K_m^{TCP} (M)	K_m^{H2O2} (M)	k_{cat} (s^{-1})	k_{cat}/K_m^{TCP} (M^{-1} s^{-1})	k_{cat}/K_m^{H2O2} (M^{-1} s^{-1})
$(1.40 \pm 0.05) \cdot 10^{-5}$	$(1.64 \pm 0.11) \cdot 10^{-1}$	$(2.37 \pm 0.02) \cdot 10^{3}$	$1.69 \cdot 10^{8}$	$1.44 \cdot 10^{4}$

Catalytic parameters were also evaluated in the absence of TFE (Figure 2.14).
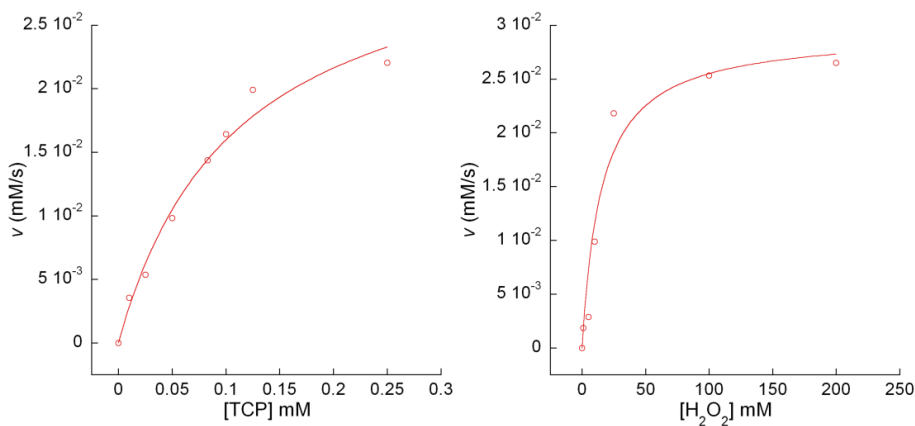
Figure 2.14. Catalytic activity of FeMC6*a in 50 mM phosphate buffer pH 6.5. **LEFT** Initial rate dependence towards TCP concentration (0.0100–0.250 mM range). **RIGHT** Initial rate dependence towards H$_2$O$_2$ concentration (0–200 mM range).

The catalytic parameters obtained for FeMC6*a are listed in Table 2.3.

Table 2.3. Catalytic parameters calculated for FeMC6*a in 50 mM phosphate buffer pH 6.5 only.

K_m^{TCP} (M)	K_m^{H2O2} (M)	k_{cat} (s^{-1})	k_{cat}/K_m^{TCP} ($M^{-1}\,s^{-1}$)	k_{cat}/K_m^{H2O2} ($M^{-1}\,s^{-1}$)
$(1.0 \pm 0.2)\cdot 10^{-4}$	$(9.4 \pm 0.8)\cdot 10^{-2}$	70 ± 6	$7.0\cdot 10^5$	$7.4\cdot 10^2$

FeMC6*a catalytic parameters obtained for TCP oxidative dehalogenation were compared to those obtained with other enzymes both of natural or synthetic origin (Table 2.5).

Table 2.4. Kinetic parameters for TCP oxidative dehalogenation catalyzed by FeMC6*a, natural , mutated and heme–protein models.

Enzyme	K_m^{TCP} (M)	K_m^{H2O2} (M)	k_{cat} (s^{-1})	$k_{cat}/K_m^{T CP}$ ($M^{-1}\,s^{-1}$)	k_{cat}/K_m^{H2O2} ($M^{-1}\,s^{-1}$)
FeMC6*a [a]	$(1.40 \pm 0.05)\cdot 10^{-5}$	$(1.64 \pm 0.11)\cdot 10^{-1}$	$(2.37 \pm 0.02)\cdot 10^3$	$1.69\cdot 10^8$	$1.44\cdot 10^4$
FeMC6*a [b]	$(1.00 \pm 0.2)\cdot 10^{-4}$	$(9.4 \pm 0.8)\cdot 10^{-2}$	70 ± 6	$7.0\cdot 10^5$	$7.4\cdot 10^2$
DHP A[1,c]	$2.07\cdot 10^{-3}$	$3.35\cdot 10^{-4}$	13.67	$6.60\cdot 10^3$	$4.08\cdot 10^4$
DHP B[1,c]	$6.85\cdot 10^{-4}$	$1.65\cdot 10^{-4}$	25.72	$3.75\cdot 10^4$	$1.56\cdot 10^5$
HRP[1,d]	$5.40\cdot 10^{-3}$	$5.0\cdot 10^{-5}$	571.3	$1.06\cdot 10^5$	$1.14\cdot 10^7$
F43Y/H64D Mb[2,e]	$3.5\cdot 10^{-6} \pm 3\cdot 10^{-7}$	N.R.	27.4 ± 0.9	$7.83\cdot 10^6$	N.R.
CTM C45[3,f]	$1.2\cdot 10^{-5}$	N.R.	0.50	$4.17\cdot 10^4$	N.R.

Conditions: [a][enzyme] = $6.7\cdot 10^{-8}$ M; 50 mM phosphate buffer, pH 6.5 with 50% (v/v) TFE. [b][enzyme] = $6.7\cdot 10^{-8}$ M; 50 mM phosphate buffer, pH 6.5. [c][enzyme] = $2.4\cdot 10^{-6}$ M; 100 mM phosphate buffer pH 7.0. [d][enzyme] = $2\cdot 10^{-7}$ M; 100 mM phosphate buffer pH 7.0 [e][enzyme] = $1\cdot 10^{-6}$ M; 50 mM phosphate buffer, pH 7.0. [f][enzyme] = $1\cdot 10^{-7}$ M; 100 mM KCl, 20 mM N–cyclohexyl–2–aminoethanesulfonic acid buffer, pH 8.58. N.R.: not reported. ([1]: [J. Zhao et al. (2015)]; [2]: [Yin, L. et al. (2018)]; [3]: [Watkins, D. et al. (2017)])

The catalytic performances of FeMC6*a are enhanced, compared to those of natural enzymes, particularly in terms of catalytic efficiency on TCP. More specifically, the k_{cat}/K_m^{TCP} of FeMC6*a in its optimal conditions is found 1600–fold enhanced compared to that of HRP thanks to the high k_{cat} value and good affinity towards TCP.

The enhancement in the catalytic performances of FeMC6*a is also evident when we compare the activity of *de novo* designed proteins with that of engineered proteins. In particular, k_{cat}/K_m^{TCP} of FeMC6*a is 20–fold enhanced compared to that of F43Y/H64D Mb and 4000–fold enhanced compared to that of CTM C45.

On the contrary, k_{cat}/K_m^{H2O2} is lower, when compared to natural enzymes, as observed for other substrates (e. g. ABTS).

The low difference in K_m^{TCP} between FeMC6*a and catalysts with higher structural complexity suggests that FeMC6*a miniaturized scaffold provides a suitable cavity able to bind TCP, while the high k_{cat} value suggests a fast exchange of substrates and products in and out from the active site thanks to the flexibility of the distal site.

The absence of TFE strongly affects both on the K_m^{TCP} and the k_{cat} value of FeMC6*a, which are 7–fold increased and 33–fold decreased, respectively, while leaving K_m^{H2O2} nearly unaffected. These findings suggest that the helical folding provided by TFE creates a binding pocket around the heme, and has a positive effect on catalysis.

These results prove that the miniaturized heme protein model FeMC6*a recapitulates the essential features required for oxidative dehalogenation reactions catalyzed by heme peroxidases.

2.3.4 **Oxidative dehalogenation of TCP in presence of HA – a preliminary study**

The results obtained on the activity of FeMC6*a towards TCP encouraged us to investigate its applicability as tool in the development of an efficient bioremediation strategy. We used the artificial metalloenzyme coupled with HA that can work as cheap and valuable matrix for the adsorption of HPs. Pilot experiments were performed using TCP. Reactions were carried out by adding HA to the FeMC6*a/TCP/hydrogen peroxide mixture and residual phenol in solution (upon extraction) was measured by GC–MS analysis. Table 2.4 reports reaction conditions used for these experiments and the observed removal efficiencies.

Table 2.5 TCP removal (%) catalyzed by FeMC6*a in the presence of HA

	[FeMC6*a] (M)	FeMC6*a:TCP:H_2O_2	TCP removal (%)
1	$6.3 \cdot 10^{-5}$	1:40:40[a]	90.2
2	$6.3 \cdot 10^{-6}$	1:400:400[a]	95.1
3	$6.3 \cdot 10^{-7}$	1:400:400[a]	7.1
4	$6.3 \cdot 10^{-7}$	1:4000:4000[a]	4.2
5	$6.3 \cdot 10^{-8}$	1:4000:4000[a]	0
6	$6.3 \cdot 10^{-8}$	1:4000:4000[b]	91.9
7	$6.3 \cdot 10^{-8}$	1:4000:400[b]	91.7

Reaction conditions: FeMC6*a in variable ratios with respect to TCP and H_2O_2. HA fixed concentration 10 mg/mL. All reactions were performed in phosphate buffer 50 mM pH 6.5 at 50 %(v/v) TFE, except for entry number **8**, which was instead performed in 50 mM phosphate buffer pH 6.5 only. [a] HA added before H_2O_2 (Entry **1–5**); [b] HA added 30 minutes after H_2O_2 (Entry **6–8**).

The GC–MS measurements were performed 40 minutes after H_2O_2 addition for entries **1–5**, and 10 minutes after HA addition for entries **6** and **7**. Two parameters were taken into account in this analysis: 1) enzyme–to–substrate ratio; 2) order of addition of the reagents. As reported in Table 2.4, the addition

of HA prior or after H_2O_2 severely affects the TCP removal efficiency. High removal efficiency was observed only with high catalyst concentration when HA is added prior H_2O_2 (Entries **1** and **2**), on the contrary low or negligible efficiencies were observed when lowering the amount of catalyst (Entries **3–5**). Interestingly, good removal efficiency was observed at very low catalyst concentration (63 nM) when HA is added after H_2O_2 (Entry **6**). Surprisingly, a ~92% removal efficiency was observed even at sub–stoichometric amount of hydrogen peroxide (entry **7**), suggesting a FeMC6*a–triggered radical mechanism undergoing TCP polymerization onto HA.

Chapter 2

2.3 **Conclusions and future perspectives**

The activity of a synthetic peroxidase, FeMC6*a, towards HPs was analyzed. A model substrate, TCP, was used to thoroughly investigate the catalytic activity of FeMC6*a in oxidative dehalogenation. By varying reaction conditions as pH and percentage of TFE, optimal conditions for catalysis were determined and used for a thorough characterization of the catalytic performances. The catalytic parameters of FeMC6*a were then evaluated both in the presence of TFE (optimal conditions for catalysis) and in its absence. The results obtained confirmed the positive impact of helical folding provided by TFE on catalysis. Furthermore, by comparing the catalytic performances obtained for other natural or synthetic enzymes, FeMC6*a confirms to be the best performing catalyst ever observed for TCP oxidative dehalogenation, both in terms of k_{cat} and k_{cat}/K_m^{TCP}. The outstanding catalytic properties of FeMC6*a have encouraged us to explore the applicability of FeMC6*a in bioremediation. Preliminary experiments were carried out to address the immobilization efficiency of TCP, in the presence of HA, with the aim of developing a new HPs–targeted bioremediation strategy. Promising results were obtained, as even sub–stoichometrical amounts of hydrogen peroxide were able to deplete TCP from water with a removal efficiency > 90%. These pilot experiments are promising and lay the basis for future practical applications of FeMC6*a in the development synthetic peroxidase based bioremediation strategies in aqueous media.

2.4 **Materials and methods**

2.4.1 **Materials**

HPLC grade solvents were employed for chromatographic analyses and purifications. Solvents with higher purity were used in the preparation of samples for GC–MS, LC–MS and UV–Vis investigations. All solvents and acetate salts were provided by Romil; trifluoroethanol (TFE) was supplied from Fluka; trifluoroacetic acid (TFA) was purchased from Applied Biosystem.

All halophenols, monobasic and bibasic phosphate salts, hydrogen peroxide (30% (v/v) stock solution), 2,6–dichloro–1,4–benzoquinone were purchased from Sigma–Aldrich.

All solvents and reagents were used without further purification.

2.4.2 **Instrumental methods**

GC–MS analyses were performed using a Shimadzu GCMS–QP2010 SE system equipped with an electron impact source and a quadrupole array as MS analyzer. All analyses were performed with capillary column Restek Rxi®–5Sil MS (30m x 0.25mm, 25µm). The optimized GC–MS parameters were selected as follows: column oven temperature 50°C; interface temperature 220°C; ion source temperature 200°C. Helium served as carrier gas (flow rate: 1.10 mL·min–1). Injections were made by an auto–sampler injector in the split mode (injection temperature: 300°C, split ratio: 50). All the molecular graphics pictures were generated with PyMOL software (DeLano Scientific Ltd) and ChemDraw Ultra 15. Data analysis was made with Origin pro 9.0 software and Kaleidagraph 4.5 software.

2.4.3 **UV–Vis measurements**

Initial concentrations of FeMC6*a, H_2O_2 and DBQ were determined by UV–Vis spectroscopy, using ε_{387} (117000 $M^{-1}cm^{-1}$), ε_{240} (39.0 $M^{-1}cm^{-1}$) and ε_{272} (14000

$M^{-1}cm^{-1}$) values, respectively; UV–Vis spectra were recorded using quartz cuvette with 0.100 and 1.000 cm path lengths.

2.4.4 pH dependence

UV–Vis spectra were recorded with a Cary Varian 60 Spectrophotometer, using quartz cuvette with 1.000 cm path length. UV–Vis analysis for pH dependence were carried out at fixed concentrations of TCP (250 μM) and Fe(III)–Mimochrome VIa (63 nM), in 50 %(v/v) TFE and different 50 mM buffers: acetate buffer pH 4.5 and 5.5, phosphate buffer pH 6, 6.5, 7 and 8.

The reactions were initiated by addition of one equivalent of H_2O_2 (250 μM) respect to TCP. Wavelength scans were recorded from 200 to 800 nm, with a 60 nm/s scan speed, under constant magnetic stirring.

2.4.5 TFE dependence

UV–Vis spectra were recorded using quartz cuvette with 1.000 cm path length. UV–Vis analysis for pH dependence were carried out at fixed concentrations of TCP (250 μM) and FeMC6*a (63 nM), in 50 mM phosphate buffer pH 6.5 and different percentages of TFE: 0, 10, 20, 30, 40 and 50 %(v/v).

The reactions were initiated by addition of one equivalent of H_2O_2 (250 μM) respect to TCP. Wavelength scans were recorded from 200 to 800 nm, with a 250 μM) respect to TCP. Wavelength scans were recorded from 200 to 800 nm, with a 60 nm/s scan speed, under constant magnetic stirring.

2.4.6 GC–MS analysis and product identification

After addition of one equivalent of hydrogen peroxide to the FeMC6*a–TCP reaction mixture, 100 μL aliquots at times 0, 10, 20 and 30 minutes were withdrawn. Each aliquot was acidified with 100 μL H_2O 0.1 %(v/v) TFA and then extracted with 200 μL of DCM. Residual water was removed from the

organic phase by filtration on anhydrous sodium sulfate. A linear temperature gradient from 50°C to 300°C, with a rate of 24°C/min, was used to analyze the organic phase. Mass spectra were recorded in 50–450 m/z range.

2.4.7 **Kinetic analysis**

UV–Vis spectra were recorded using quartz cuvette with 1.00 cm path length. The dependence towards the oxidizing substrate was carried out at fixed concentrations of TCP (0.250 mM) and FeMC6*a (63.0 nM), in 50 mM phosphate buffer pH 6.5 and 50%(v/v) TFE. The H_2O_2 concentration was varied in the range of 0.50 mM to 200 mM. To study the dependence towards the reducing substrate TCP, H_2O_2 concentration was fixed at 300 mM and FeMC6*a was 63.0 nM, in phosphate buffer pH 6.5 and 50 %(v/v) TFE. The TCP concentration was varied in the range of 0.010 to 0.250 mM. The two set of data were then fitted according to a two–substrates Michaelis–Menten equation

2.4.8 **Catalysis in the presence of humic acids**

All reactions were performed at fixed TCP concentration (250 μM), with variable enzyme and hydrogen peroxide ratios (See Table 2.4). Pilot experiments were perfomed at different concentrations of HA (1-10-100 mg/mL) and 10 mg/mL was set as best operative condition both for removal efficiency and disperdability of HA in buffer solution (data not shown). Identification of residual TCP was performed upon extraction with DCM as reported in Paragraph 2.4.6. Quantitation was performed by normalizing the area of TCP with that obtained for chlorobenzene used as internal standard. %Removal of TCP was calculated as follows:

$$\% \, Removal = \frac{\left(\frac{A_{sub}}{A_{I.Std.}}\right)_0 - \left(\frac{A_{sub}}{A_{I.Std.}}\right)_x}{\left(\frac{A_{sub}}{A_{I.Std.}}\right)_0} \cdot 100$$

2.5 **References**

- P. K. Arora, H. Bae "Bacterial degradation of chlorophenols and their derivatives" Microb. Cell Fact. 13 (2014), 25–31.

- A. Bhandari, F. Xu "Impact of peroxidase addition on the sorption– desorption behavior of phenolic contaminants in surface soils" Environ. Sci. Technol. 35 (2001), 15, 3163–3168.

- Z. Chen, V. de Serrano, L. Betts, S. Franzen "Distal histidine conformational flexibility in dehaloperoxidase from *Amphitrite ornata*" Acta Cryst. D65 (2009), 34-40.

- G. Eibes A. Arca–Ramos G. Feijoo J. M. Lema M. T. Moreira "Enzymatic technologies for remediation of hydrophobic organic pollutants in soil" Appl. Microbiol. Biotechnol. 99 (2015), 8815–8829.

- P. Fernandez Freire, V. Labrador, J. M. Perez Martin, M. J. Hazen, "Cytotoxic effects in mammalian Vero cells exposed to pentachlorophenol" Toxicology 210 (2005), 37–44.

- S. Franzen, M. K. Thompson, R. A. Ghiladi "The dehaloperoxidase paradox" Biochim. Biophys. Acta 1824 (2012), 578–588.

- M. Fukushima, A. Sawada, M. Kawasaki, H. Ichikawa, K. Morimoto, K. Tatsumi, M. Aoyama. "Influence of Humic Substances on the Removal of Pentachlorophenol by a Biomimetic Catalytic System with a Water–Soluble Iron(III)−Porphyrin Complex" Environ. Sci. Technol. 37 (2003), 1031–1036.

- M. Fukushima, S. Shigematsu, S. Nagao "Oxidative degradation of 2,4,6–trichlorophenol and pentachlorophenol in contaminated soil suspensions using a supramolecular catalyst of 5,10,15,20–tetrakis(p–hydroxyphenyl)porphine–iron(III) bound to humic acid via formaldehyde polycondensation" J. Environ. Sci. Heal. A 44 (2009), 1088–1097.

- B. A. Gomes de Melo, F. Lopes Motta, M. H. Andrade Santana "Humic acids: Structural properties and multiple functionalities for novel technological developments" Mat. Sci. Eng. C 62 (2016), 967–974.

- K. Guyton, D. Loomis, Y. Grosse, F. El Ghissassi, D. Bouvard, N. Guha, H. Mattock, K. Straif "Carcinogenicity of pentachlorophenol and some related compounds" Lancet Onc. 17 (2016), 1637–1638.

- J. Huff "Long–term toxicology and carcinogenicity of 2,4,6–trichlorophenol" Chemosphere, 89 (2012), 521–525.

- Y. C. Lai, S. C. Lin "Application of immobilized horseradish peroxidase for the removal of p–chlorophenol from aqueous solution" Process Biochem. 40 (2004), 1167–1174.

- Z. Li, B. Zhu, B. Wang, J. Gao, X. Fu, Q. Yao "Stress responses to trichlorophenol in Arabidopsis and integrative analysis of alteration in transcriptional profiling from microarray" Gene, 555 (2015), 159–168.

- R. L. Osborne, L. O. Taylor, K. P. Han, B. Ely, J. H. Dawson "Amphitrite ornata dehaloperoxidase: enhanced activity for the catalytically active globin using MCPBA" Biochem. Bioph. Res. Co. 324 (2004), 1194–1198.

- R. L. Osborne, G. M. Raner, L. P. Hager, J. H. Dawson "*C. fumago* Chloroperoxidase is also a Dehaloperoxidase: Oxidative Dehalogenation of Halophenols" J. Am. Chem. Soc. 128 (2006), 1036–1037.

- R. L. Osborne, M. K. Coggins, G. M. Raner, M. Walla, J. H. Dawson "The Mechanism of Oxidative Halophenol Dehalogenation by Amphitrite ornate Dehaloperoxidase Is Initiated by H_2O_2 Binding and Involves Two Consecutive One–Electron Steps: Role of Ferryl Intermediates" Biochemistry 48 (2009), 20, 4231–4238.

- M. Palomo, A. Bhandarib "Peroxidase–Catalyzed Stabilization of 2,4–Dichlorophenol in Alkali–extracted Soils" J. Environ. Qual. 40 (2010), 126–132.

- J. Pei, R. Zhang, C. Hsu, Y. Wang "ass Spectrometry-Inspired Degradation of Disinfection By-Product, 2,6-Dichloro-1,4-benzoquinone, in Drinking Water by Heating" Mass Spectrom. (Tokyo) 7 (2018), 1, A0068.

- A. Plummer, M. K. Thompson, S. Franzen "Role of Polarity of the Distal Pocket in

the Control of Inhibitor Binding in Dehaloperoxidase–Hemoglobin" J. Am. Chem. Soc. 52 (2013), 2218–2227.

- F. Qin, Y.-Y. Zhao, Y. Zhao, J. M. Boyd, W. Zhou, X.-F. Li "A toxic disinfection by-product, 2,6-dichloro-1,4-benzoquinone, identified in drinking water" Angew. Chem. Int. Ed. 49, (2010), 790-792.

- D. Roccatano, G. Colombo, M. Fioroni and A. E. Mark, "Mechanism by which 2,2,2–trifluoroethanol/water mixtures stabilize secondary–structure formation in peptides: A molecular dynamics study" Proc. Natl. Acad. Sci. USA 99 (2002), 12179–12184.

- V. de Serrano, Z. Chen, M. F. Davis and S. Franzen "X–ray crystal structural analysis of the binding site in the ferric and oxyferrous forms of the recombinant heme dehaloperoxidase cloned from Amphitrite ornata" Acta Cryst. D63 (2007), 1094– 1101.

- S. Sumithran, M. Sono, G. M. Raner, J. H. Dawson "Single Turnover Studies of Oxidative Halophenol Dehalogenation by Horseradish Peroxidase Reveal a Mechanism Involving Two Consecutive One Electron Steps: Toward a Functional Halophenol Bioremediation Catalyst" J. Inorg. Biochem. 117 (2012), 316–321.

- M. K. Thompson, M. F. Davis, V. de Serrano, F. P. Nicoletti, B. D. Howes, G. Smulevich, and S. Franzen "Internal Binding of Halogenated Phenols in Dehaloperoxidase–Hemoglobin Inhibits Peroxidase Function" Biophys. J., 99 (2010), 1586–1595.

- P. T. Vasudevan, L. O. Li, L. O. "Peroxidase catalyzed polymerization of phenol" Appl. Biochem. Biotechnol. 60 (1996), 1, 73–82.

- D. W. Watkins, J. M. X. Jenkins, K. J. Grayson, N. Wood, J. W. Steventon, K. K. L. Vay, M. I. Goodwin, A. S. Mullen, H. J. Bailey, M. P. Crump "Construction and in Vivo Assembly of a Catalytically Proficient and Hyperthermostable de Novo Enzyme" Nat. Commun. 8 (2017), 1, 358–367.

- T. Xu, T. J. Zhao, P. Hu, Z. Dong, J. Li, H. Zhang, D. Yin, Q. Zhao," Pentachlorophenol exposure causes Warburg–like effects in zebrafish embryos at

gastrulation stage" Toxicol. Appl. Pharmacol. 277 (2014), 183–191.

- L. Yin, H. Yuan, C. Liu, B. He, S. Q. Gao, G. B. Wen, X. Tan, Y. W. Lin, "A Rationally Designed Myoglobin Exhibits a Catalytic Dehalogenation Efficiency More than 1000–Fold That of a Native Dehaloperoxidase" ACS Catal. 8 (2018), 10, 9619.9624.

- J. Zhao, C. Lu, S. Franzen "Distinct Enzyme–Substrate Interactions Revealed by Two Dimensional Kinetic Comparison between Dehaloperoxidase–Hemoglobin and Horseradish Peroxidase" J. Phys. Chem. B 119 (2015), 40, 12828–12837.

This page was intentionally left blank

Chapter 3

Synthetic peroxidases in electrochemistry and amperometric biosensors

3.1 **Introduction**

    3.1.1 **Metalloproteins in electrochemistry**

Nature deals with electrons in a specific and unique manner [Nanda, V. et al. (2016)]. In the field of bioenergetics, the energy flow produced by metabolic pathways, such as ATP production (photosynthesis and respiration), is strictly controlled and requires electron transfer (ET). To accomplish this "simple" task, Nature uses metal ions, such as iron and copper, housed into protein matrices. The protein matrix modulates the environments of these metal ions and tunes their redox potential to handle electrons properly. The limited set of metal ions, mainly iron and copper, across evolution, has been installed in different coordination environments and geometries to fulfill all the requirements for efficient, fast and selective ET process. The most highly represented metal sites involved in ET processes are listed in Figure 3.1.

Cytochrome b_5 [Fe_4S_4] ferrodoxin   Azurin
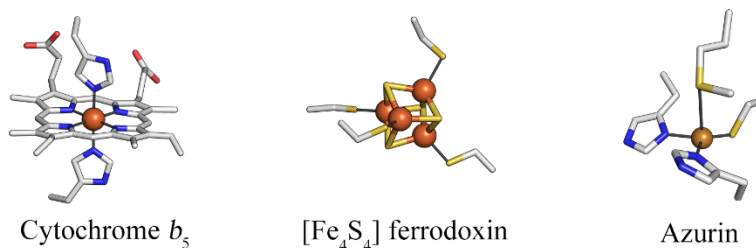
Figure 3.1. Common metal centers found in ET proteins

Three main ET protein classes can be listed: cytochromes, iron–sulfur proteins and cupredoxins [Nanda, V. et al. (2016); Plegaria, J. S. et al. (2015)]. All together, these three classes are able to cover a wide range of potentials, spanning from –1 V (where H^+ is reduced to H_2) to +1 V (where water is oxidized to O_2). Iron–sulfur proteins and copper proteins occupy the middle high ends of the potential window while heme proteins, such as cytochromes lay in the middle (Figure 3.2).

Iron–sulphur proteins are among the oldest on earth. They arose in early times, when iron and sulfur were both highly abundant in the earth crust. This allowed these two elements to spontaneously assemble in clusters, mainly containing four iron and four sulfur atoms [Meyer, J. (2008); Imlay, J. A. et al. (2006)]. Although the atmosphere evolved towards more oxidizing environment, these proteins were conserved in living systems and preserved across evolution, playing a crucial role in photosynthesis and respiration. Copper proteins, by means of Type 1 Cu and Cu_A centers are also highly represented as ET proteins. They are highly widespread in nature and count with high ET rates. Cytochromes are a major class of heme–containing ET proteins found ubiquitously in biology. In eukaryote, they are mainly localized in the inner membrane of mitochondria and play an important role in the respiratory chain. [Yanagisawa, S. et al. (2006)].

Thanks to the diversity in the coordination environment, these proteins are able to exert their function over a very wide range of potential (Figure 3.2).
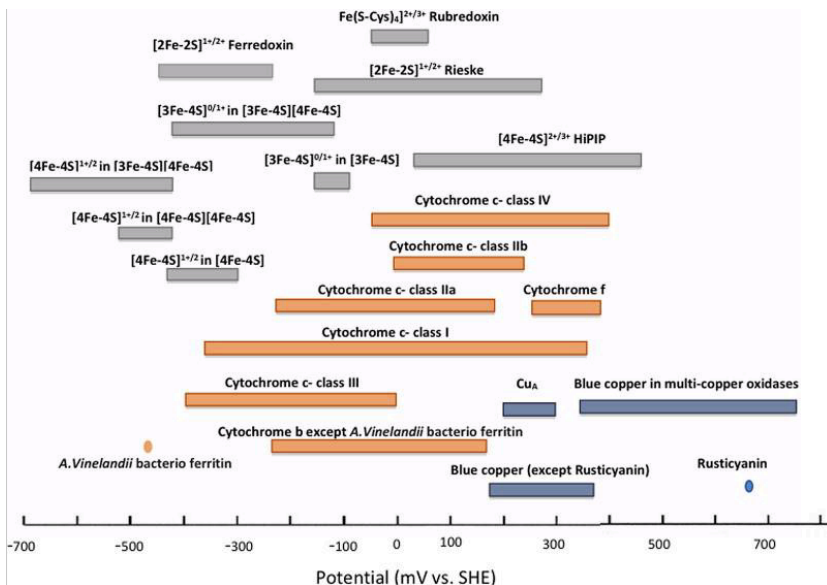
Figure 3.2. Potential windows for ET proteins. Adapted from [Liu, J. (2014)]

Bioelectrochemistry over the years has been a valuable tool to gain insights in the complex world of the structure/function relationships of redox proteins. Many metalloproteins have been studied by direct bioelectrochemistry and their activity at electrode surfaces has been thoroughly investigated thanks to bioelectrocatalysis [Milton, R.D. et al. 2017].

Indeed, by simple electrochemical techniques such as cyclic voltammetry (CV) and square–wave voltammetry (SWV), key parameters of metalloproteins can be measured, such as $E^{0'}$ potentials and electron transfer rates. When taking into account an enzyme, by measuring catalytic currents, electrochemistry can often provide non trivial insights into the reaction mechanism, number of exchanged electrons, affinity for substrates (K_m) and catalytic constants (k_{cat}). Particular interest over the latest decades has been devoted to the investigation of immobilized proteins [Ranieri, A. et al. (2019)]. Thanks to the advances in surface chemistry, the evaluation of the electrochemical properties can be carried out by using negligible amounts of metalloproteins. To this aim, a plethora of immobilization techniques have been developed which help retaining tridimensional structure of the protein therefore preserving the native properties.

Mainly, immobilization of metalloproteins onto electroactive surfaces can be accomplished by direct chemisorption, molecular entrapment into polymers or chemical linkage to electrodes [Nöll, T. and Nöll, G. (2011)].

Many factors should be considered when developing an immobilization strategy. Its success relies on the control of orientation of the proteins and on the distance to the electrode, so that the redox active site can be in contact with the electrode surface, the packing density (i.e. number of proteins per surface unit), which are critical for electron exchange rate. The environment surrounding the protein also plays a critical role in the preservation of its native tridimensional structure, therefore an efficient immobilization strategy should provide a soft environment [Ranieri, A. et al. (2019)] in order to mimic physiological conditions, thus

decreasing and in some cases avoiding denaturation.

3.1.2 Heme proteins in electrochemistry

Bioelectrochemistry has long been a powerful tool to characterize heme proteins. It fascinated scientists since the first studies on cytochrome *c* [Eddowes, M. J. and Hill, H. A. O. (1976)]. After this, a great variety of differently functional heme proteins (cytochromes, O_2–binding proteins, peroxidases, cytochromes P450, catalases) were characterized electrochemically and thanks to these studies a deeper understanding of the electrochemical properties of these heme proteins was acquired. This paved the way for the plethora of applications we are aware of nowadays.

The differences in the coordination sphere of the heme reflects in differently tuned heme cofactors, leading to extreme diversity in electrochemical and electrocatalytic properties. Furthermore, the easy integration of these proteins in electroconductive systems makes their use an easy challenge for scientists. Heme proteins, and among all, peroxidases, are robust components in biosensors and serve mainly as reliable reporter enzymes for the detection of peroxides. The high affinity of peroxidases for hydrogen and organic peroxides (*t*–buthyl hydroperoxide, di–*t*–buthyl peroxide) yields devices with enhanced selectivity, low detection limit and sensitivity.

Table 3.1. Peroxides HRP biosensors

Substrate	Surface	LOD	Linear range	Ref.
H_2O_2	HRP–MWCNTs/ Chit/GCE	10.3 µM	16.7–740 µM	[Quian, L. (2006)]
H_2O_2	Co_3O_4/MWCNTs/ HRP/GCE	0.74 µM	0.74–19 µM	[Kaçar, C. et al. (2014)]
H_2O_2	SPCE|GS–Nafion/ Fe_3O_4–Au–HRP	12 µM	20 µM–2.5 mM	[Xin, Y. et al. (2013)]
H_2O_2	HRP/TiO_2–c– MWCNT–GR– RUT/GCE	0.44 µM	2–120 µM	[Özdemir, D. et al. (2019)]
H_2O_2	HRP/HAuDE	1.5 µM		[Wu, S.-H. (2020)]
t–BuOOH	GCE/SWCNT	120 µM	391–3340 µM	[Xu, H. et al. (2009)]

Legend: Chit: chitosan; TiO_2: titanium dioxide; GCE: glassy carbon; MWCNT: multiwalled carbon nanotubes; SWCNT: single–walled carbon nanotubes; Co_3O_4: cobalt oxide nanoparticles; SPCE: screen–printed carbon electrode; RUT: hexaammineruthenium chloride; HAuDE: heated gold disk electrode; t–BuOOH: t– buthyl hydroperoxide.

Table 3.1 lists some amperometric biosensors, which profit of HRP as sensing component to detect peroxides. HRP can be efficiently immobilized onto different surfaces, while preserving its peroxidase activity, and the resulting device shows good detection ranges and limits of detection (LOD).

The great versatility and wide range of substrates for HRP has been also exploited for the construction of devices with different applications. Recently, HRP, immobilized onto TiO_2 was efficiently used for the development of light-activated phenol sensor operating by flow injection analysis [Rahemi, V. et al. (2020)]. The sensing system of this device relies on the ability of TiO_2 to produce, upon light irradiation, reactive oxygen species (ROS), which are then used by HRP to oxidize phenolic substrates (hydroquinone and 4-aminophenol).

Another example is provided by [Marquitan, M. et al. (2020)]. The authors developed a device capable to measure glutamate concentration amperometrically, on a single cell-level, with a remarkable sensitivity. The high

sensitivity was achieved by integrating a mixed glutamate oxidase-HRP bienzymatic system onto sub-micron range carbon electrode. In this device, the oxidation of glutamate by means of glutamate oxidase yields H_2O_2 which is readily detected by HRP.

Also, non-peroxidases heme proteins can be used in biosensors. When immobilized onto electroconductive surfaces, inducible catalytic properties can be observed, either for slight structural changes or for "exotic" oxidation states. Efficient H_2O_2–sensors have been developed with O_2–binding myoglobin or with ET cytochrome *c*. In these cases, the immobilization plays an important role, as the H_2O_2–reactivity of myoglobin and cytochrome *c* might arise from slight structural changes that "de–tunes" the heme from its built–in function and unleashes it for a new function [Lu, H. et al. (2006); Niu, T. et al. (2019); Wang, T. et al. (2013); Luo, Y. et al. (2009)]. Another example is given by HRP based O_2–sensors. The operational principle of these sensors relies on the electrocatalytic reduction of O_2 by ferrous heme. Heme in its Fe^{3+} form is unable to bind molecular oxygen, but, upon electrochemical reduction to its Fe^{2+} oxidation state, it becomes sensitive to O_2. After the formation of the Fe^{2+}–O_2 complex, the iron center can easily shuttle electrons to the oxygen thus yielding reduction product as superoxide anion (O_2^-) by one–electron reduction, H_2O_2 by two–electron reduction or H_2O by 4–electron reduction [Huang, X. and Groves, J. T. (2018)]. HRP coordination environment finely tunes and stabilizes Fe^{3+} or higher oxidation states, but by electrochemical reduction of HRP, a Fe^{2+}–HRP is readily achieved, which is able to bind and reduce O_2. The high affinity of ferrous–heme towards O_2 would allow for the development of O_2–sensor with extremely high sensitivity, but unfortunately no meaningful practical application has been proposed yet. A possible reason of this might be related to the technical issues regarding the measurement of O_2 concentration in standards solutions, especially at low concentrations.

3.1.3 **ET properties by structure simplification**

Although great advances in immobilization chemistry were achieved, recreating the native conditions ensuring protein stability and performing direct electrochemistry in a perfectly safe environment is still a challenge. The stability of proteins and metalloproteins requires precise environment, such as pH and ionic strength, which not always are complied upon immobilization. Interaction with a solid matrix often implies structural changes of the protein which may harm its catalytic/electrocatalytic properties, therefore lowering its efficiency. Another issue relies in the usually large non–conductive matrix which envelops the redox cofactor, thus hindering the direct ET process and lowering ET rates [Wong, T. S. and Schwaneberg, U. (2003)].

An enzyme reaction at an electrode surface can proceed through direct electron transfer: the electron is directly transferred from the active center of the enzyme to the electrode surface. Many proteins or glycoproteins have their redox centers buried in their structure, thus the direct communication between the active site and the electrode can be hindered. To this aim, efforts were devoted to simplify the structure and "trim the fat" hindering ET processes [Wong, T. S. and Schwaneberg, U. (2003)]. Yeasts and fungi usually express highly glycosylated proteins. In order to boost the ET rates between these proteins and electrodes, a possible solution would be to pretreat them with oxidizing agents for cleaving the sugar moieties. However, strong oxidizing agents such as periodates often reduce enzymatic activity significantly and safe protocols must be optimized for each protein [Wong, T. S. and Schwaneberg, U. (2003); Tiziani, S. et al. (2003)]. Another example of structure simplification for improving the ET rates is to remove amino acid residues that are not key residues in the protein structure and function. Microperoxidase–11 (MP–11) results from the proteolytic cleavage of cytochrome *c*. It is an undecapeptide (H–Val–Gln–Lys–Cys–Ala–Gln–Cys–His–

Thr–Val–Glu–OH) with a heme *c* group attached through thioether bonds at Cys4 and Cys7 residues [Katz, E. et al. (2002)]. MP–11 reveals several advantages compared to its undigested analogue. It indeed exhibits enhanced performances in peroxide reduction and direct electrical communication with many different electrodes because of its heme exposure [Zhang, B. et al. (2015)]. The ET properties enhancement have paved the way for many applications of MP–11 scaffold in O_2 reduction [Renault, C. et al., (2012)] or hydrogen evolution [Kleingardner, J. G. et al. (2014)] by replacement of iron with cobalt. Moreover, a further structurally simplified analogue, MP–8 has been successfully employed in the development of biofuel cells [Ramanavicius, A. et al., (2005)].

3.1.4 Designed and engineered ET metalloproteins

Protein design and engineering is a powerful approach [Nastri, F. et al (2019)] which, over the last decades, provided scientists not only with robust and efficient electrocatalysts, but also with great insights into the structure–function relationships determining the activity of metal centers.

In the field of *de novo* design [Nastri, F. et al. (2019)], De Grado and Dutton were the first who achieved the goal in designing an artificial heme–containing oxidoreductase [Robertson, D.E. et al. (1994); Choma, C.T. et al. (1994)]. More specifically they *de novo* designed a four–helix bundle protein able to bind one or multiple heme groups. The investigation over the electrochemical properties of the designed oxidoreductase confirmed a behavior similar to the native protein.

A further contribution by Dutton was provided with the design of *maquettes*. Dutton's group achieved to reproduce the natural ET function within a *de novo* sequence, confirming that only few principles must be satisfied in order to recreate an ET center within an artificial protein:

(**1**) a highly hydrophobic environment for housing the cofactor and ensuring tight binding to the protein matrix;

(**2**) a stable protein scaffold tolerating side–chain protonation changes and allowing pH–dependent redox behavior;

(**3**) a modulation of the cofactor redox potential by different charge distributions in the exterior polar residues [Moser, C.C. et al. (2016); Lichtenstein, B.R. et al. (2012)]. Thanks to these pioneering research, in recent years many *de novo* designed four–helix bundles appeared. These principles were applied in the design and engineering of a water–soluble heme *maquette* able to perform diffusive electron transport, mimicking natural cytochromes [Fry, B. A. et al. (2016)]. The authors proved that the water–soluble *maquette* was able to shuttle electrons to cytochrome *c* within similar timescales and charge complementarity modulation observed in natural systems.

Further examples of the power of *de novo* design are provided by the results achieved in Ghirlanda's group. They successfully designed a homo–dimeric three–helix bundle (DSD) binding two [4Fe–4S] groups within its hydrophobic core. The insertion and integrity of the [4Fe–4S] core was confirmed by CD and EPR analysis. Moreover, pulsed electron–electron double–resonance experiments confirmed an inter–cluster distance of 29–34Å [Roy, A. et al. (2013)]. An evolution of this work yielded CTPR–[4Fe–4S] (consensus tetratricopeptide repeat with [4Fe–4S] metal cluster), in which multiple [4Fe–4S] clusters were inserted into a repetitive sequence designed applying a bottom–up approach [Main, E. R. G. et al. (2013)]. Square wave voltammetry characterization confirmed that the designed CTPR–[4Fe–4S] proteins are redox active showing potentials consistent with low–potential protein–bound clusters [Mejias, S. H. et al. (2019)].

By *de novo* approach, the challenge to design redox active copper centers embedded in protein matrices was overcome. Protein matrices with the features

to house metal ions in different oxidation states, therefore fulfilling their different coordination requirements were successfully designed. In a recent work, Pecoraro and coworkers [Plegaria, J. S. et al. (2015); Plegaria, J. S. et al. (2016)] characterized the intermolecular electron transfer (ET) properties of a *de novo* designed metallopeptide using laser–flash photolysis. They incorporated copper metal binding site within an antiparallel three helix bundle α3D–CH3 to mimic a Type 1 copper ET site naturally observed in the β–barrel fold of cupredoxins. Upon addition of photosensitizers, the conversion of Cu(I)α$_3$D–CH3 to a Cu(II) (λ_{max}=400 nm) species was observed, confirming the ET transfer reaction between the photo–oxidant and Cu(I)α$_3$D–CH3. Even though no full replication of native cupredoxin spectroscopic features was observed, this work demonstrated the success of *de novo* approach in building an ET site within a designed protein that is capable of rapid electron transfer at a desired reduction potential. The α$_3$D three helix bundle scaffold was also used by Pecoraro's group to recreate a rubredoxin metal site within α$_3$DIV-L21C-GSGC, obtained by site directed mutagenesis [Tebo, A. G. et al. (2018)]. The spectroscopic characterization over the *de novo* rubredoxin highlighted its similarity to natural rubredoxin, as confirmed by UV-Vis, Mössbauer, electron paramagnetic resonance and magnetic circular dichroism. Furthermore, measurements of reduction potential suggested that the designed metalloprotein could function similarly to natural rubredoxins.

Along with *de novo* approach, protein engineering has proved its value in expanding and enhancing the activity of metalloenzymes. In this respect, the design of mutant enzymes containing single and/or multiple residues substitutions represents an excellent strategy to fine tuning the redox potentials of ET center that are involved in controlling the ET rates [Hosseinzadeh, P., Lu, Y., (2016)].

Chapter 3

Ward and Borovik [Mann, S. I. et al. (2016)] developed a modular artificial cupredoxin by inserting a series of biotinylated di[2–(2–pyridyl)propyl]amine ligands, differing by the length of the linker, into a $S^{112}C$ engineered streptavidin. Spectroscopic investigations confirmed the nature of the complex. In particular, one of these analogues showed a structure similar to a Type 1 copper center. Moreover, EPR measurements highlighted the presence of a Cu−S$_{cys}$ bond, and X-ray diffraction analysis provided structural evidence of a Cu center endowed with a N_3S primary coordination sphere and is positioned at 1.3 Å from the biotin's binding site. Cyclic voltammetry experiments confirmed the electroactivity of the complex despite its non–fully reversible behavior.

Lu and coworkers [Yu, Y. et al. (2017)] engineered azurin, a common Type 1 copper protein, by linking the N– and C–termini and creating new termini in the loops between first and second β–strands or between 3rd and 4th β–strands. Spectroscopic, EPR, CV and crystallography confirmed a well–preserved primary coordination sphere in all the variants. Interestingly, the reduction potentials increased by 18 and 124 mV were observed over that of the wild-type protein.

Within the same research group, myoglobin was engineered to yield a designed oxidase. The L29H/F43H/G65Y mutation of myoglobin originated a catalyst capable of reducing dioxygen with an O_2 reduction rate of 52 s^{-1}, similarly to a native cytochrome c_{bb3} oxidase (50 s^{-1}). In this mutant, patterning more favorable electrostatic interactions between the engineered myoglobin and its native redox partner, cyt b_5, resulted in a 400–fold electron transfer (ET) rate enhancement [Yu, Y. et al. (2015)].

Some examples of ET process within miniaturized scaffold come from the results achieved by our group. Through miniaturization process applied to rubredoxins a new class of miniaturized electron transfer protein (METP) was designed and synthesized. Starting from the crystal structure of *Desulfovibrio*

vulgaris rubredoxin, a tetrahedral $(S^{\gamma}–Cys)_4$ iron–binding site was designed. UV–Visible and circular dichroism spectroscopy confirmed a peptide–to–metal 2:1 stoichiometry in the presence of Co^{2+}, Zn^{2+} and $Fe^{2+/3+}$. Moreover, UV–visible analysis of the metal complexes confirmed that the four Cys ligands arrange themselves tetrahedrally around the metal ion, as expected from design. The NMR characterization of the diamagnetic Zn(II)–METP complex fully supported the structure of the designed model, proving that METP reproduces the main features of rubredoxin [Lombardi, A. et al. (2000)]. Further, DeGrado's group *de novo* designed RM1, a single chain beta-protein that forms a stable, redox-active 4-Cys thiolate $Fe^{2+/3+}$ site, analogously to rubredoxin [Nanda, V. et al. (2005)]. Although rubredoxins redox potential falls between -90 and 40 mV *vs* NHE, the electrochemical characterization showed a high midpoint potential, being 55 mV *vs* NHE at pH 7.5. Nonetheless, compared to the previously reported METP, the single-chain RM1 showed enhanced redox activity, being able to complete up to 16 cycles under aerobic conditions.

As mentioned in paragraph 3.1.3, structural simplification boosts ET process, as confirmed by the enhanced ET properties of MPs. It has been demonstrated that small redox protein, such as cytochrome c, can shuttle electrons directly to bare glassy carbon electrodes [Heller A., Acc. Chem. Res., (1990) 23, 128-134].

For large redox enzyme, such as glucose oxidase, this is difficult to accomplish as they have thick insulating protein shells and their catalytic centers are buried deep inside and protected from the surroundings.

To this aim, using miniaturized heme protein models can offer many advantages both in terms of electron transfer properties and electrochemical signal.

Their robustness (to prevent denaturation on the electrode surface), and small size can simplify the electron transfer path to the electrode and ensure direct electron transfer. Moreover, the closeness between the redox center and the surface together with the increasing surface coverage allows for a better wiring

between the enzyme and the electrode and enhance electrochemical signals.

This feature encouraged us to explore the electrochemical properties of FeMC6*a miniaturized scaffold, immobilized onto electrode surfaces for biosensing purposes. Previous explorative studies over the electrochemistry of Fe–mimochromes were reported. MC6 was immobilized by hydrophobic interactions onto decanethiol coated gold electrode [Ranieri, A. et al. (2010)]. Although immobilization slightly influenced the reduction potential, a reversible behavior was observed under argon. Instead, when the MC6 electrode is exposed to O_2, interestingly it electrochemically turned over dioxygen.

Further electrochemical characterization was reported for other mimochrome analogues [Vitale, R. et al. (2014)]. In particular, the spectroelectrochemistry behavior FeMC6* was investigated. Upon immobilization onto indium–tin–oxide electrodes, Fe^{3+}–MC6* showed remarkable reversible features under argon when cycling between ferric and ferrous oxidation states with a $E^{0'}$ reduction potential of –0.32 V *vs* Ag/AgCl. In a recent paper, the electrochemical behavior of a mimochrome analogue, FeMC6–S6G was investigated [Zambrano, G. et al. (2018)]. FeMC6–S6G was conjugated to lipoic acid and then immobilized onto gold electrodes showing quasi–reversible properties with a $E^{0'} = $ –0.326 V *vs* Ag/AgCl for the $Fe^{2+/3+}$ couple, similarly with previous works.

These results on the electrochemical behavior of mimochromes have encouraged us to further investigate mimochrome electroactivity with the aim to integrate miniaturized heme protein models in biosensing.

3.2 **Results and discussion**

3.2.1 **Electrochemical behavior of FeMC6*a immobilized onto GCE**

The interesting insights given by the electrochemical analysis of metalloproteins led us to explore the behavior of FeMC6*a immobilized onto electrode surface. FeMC6*a was immobilized onto glassy carbon electrodes (GCE) by using Nafion polymer. The functionalized electrode behavior was studied by CV between 0.4 and –0.5 V *vs* Ag/AgCl (100 mM phosphate buffer at pH 6.5), range in which the reduction of Fe^{3+} to Fe^{2+} is usually observed for peroxidases [Lee, A. C. et al. (2008)]. The CV is reported in Figure 3.3.
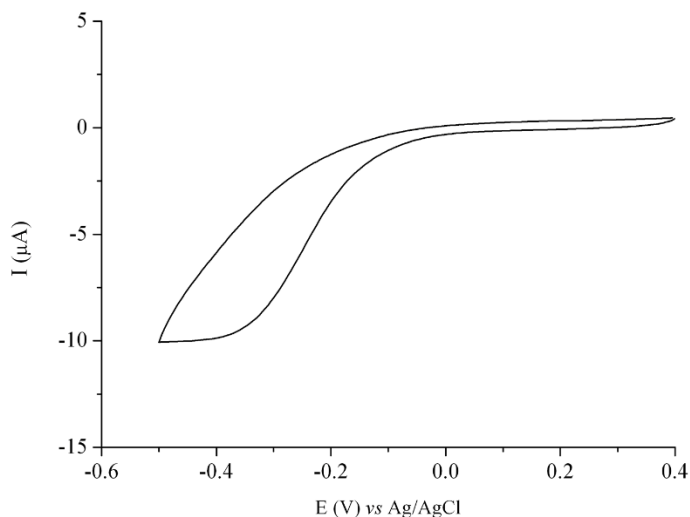
Figure 3.3. CV of FeMC6*a@GCE in 100 mM phosphate buffer pH 6.5

FeMC6*a onto GCE (FeMC6*a@GCE) CV showed a moderate reduction peak around –0.3 V *vs* Ag/AgCl, similar to the $E^{0'}$ reduction potential of previously studied analogues [Vitale, R. et al. (2014); Zambrano, G. et al. (2018)].

Due to the strong dependency between activity of FeMC6*a and fluorinated alcohols, we investigated the effect of these alcohols on the electrode behavior

was assessed by CV analysis. Two concentrations of fluorinated alcohols were chosen (20%(v/v) for 2,2,2–trifluoroethanol (TFE) and 10%(v/v) for 1,1,1,3,3,3–hexafluoroisopropanol (HFIP)) to ensure stability of entrapping Nafion polymer. The CV obtained in these conditions are reported in Figure 3.4.
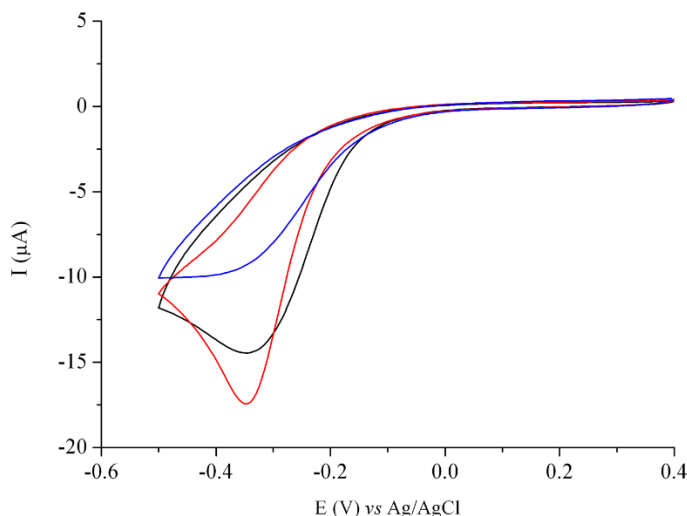
Figure 3.4. CV analysis of FeMC6*a at 20%(v/v) TFE (black line), 10%(v/v) of HFIP (red line) in 100 mM phosphate buffer pH 6.5, and buffer only (blue line).

The presence of fluorinated alcohols modified the electrochemical profile of FeMC6*a. Figure 3.4 clearly highlights a strong effect given by these two fluorinated alcohols. Moreover, a non–reversible peak at -0.32 V *vs* Ag/AgCl is observed. The non–reversible behavior of FeMC6*a suggests a catalytic process undergoing the reduction of Fe^{3+}–MC6*a to Fe^{2+}–MC6*a species, and an oxygen reduction reaction (ORR) mechanism. Further details on the catalytic behavior of FeMC6*a will be given in paragraph 3.2.3.

3.2.2 **Selectivity of FeMC6*a@GCE**

The strong increase in current with 20%(*v/v*) TFE and 10%(*v/v*) HFIP led us to investigate FeMC6*a@GCE as a sensor for halogenated alcohols.

To test whether the FeMC6*a@GCE is selective towards fluorinated alcohols, a chlorinated alcohol was used as control. To this purpose, 2,2,2–trichloroethanol (TCE) was used at 10%(*v/v*) in 100 mM phosphate buffer pH 6.5. The CV analysis was performed as previously reported and it is shown in Figure 3.5.
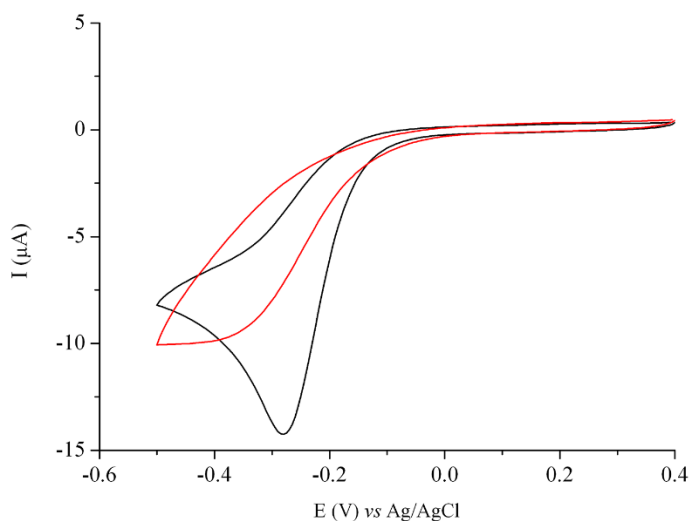
Figure 3.5. CV analysis of FeMC6*a at 10%(*v/v*) TCE (black line), and in buffer only (red line).

Figure 3.5 shows an increase in reduction current caused by TCE addition, highlighting the inability of FeMC6*a@GCE in discriminating between differently halogenated alcohols.

A second selectivity test was performed by comparing CVs obtained with halogenated alcohols (Figure 3.6a) with those obtained with non–halogenated alcohols (Figure 3.6b). The effect of DMSO as polar aprotic solvent was also studied.

Ethanol, methanol, isopropanol and dimethylsulfoxide at 20%(*v/v*) were used.

Figure 3.7 compares the peak currents in different solvent condition.

(a)

(b)
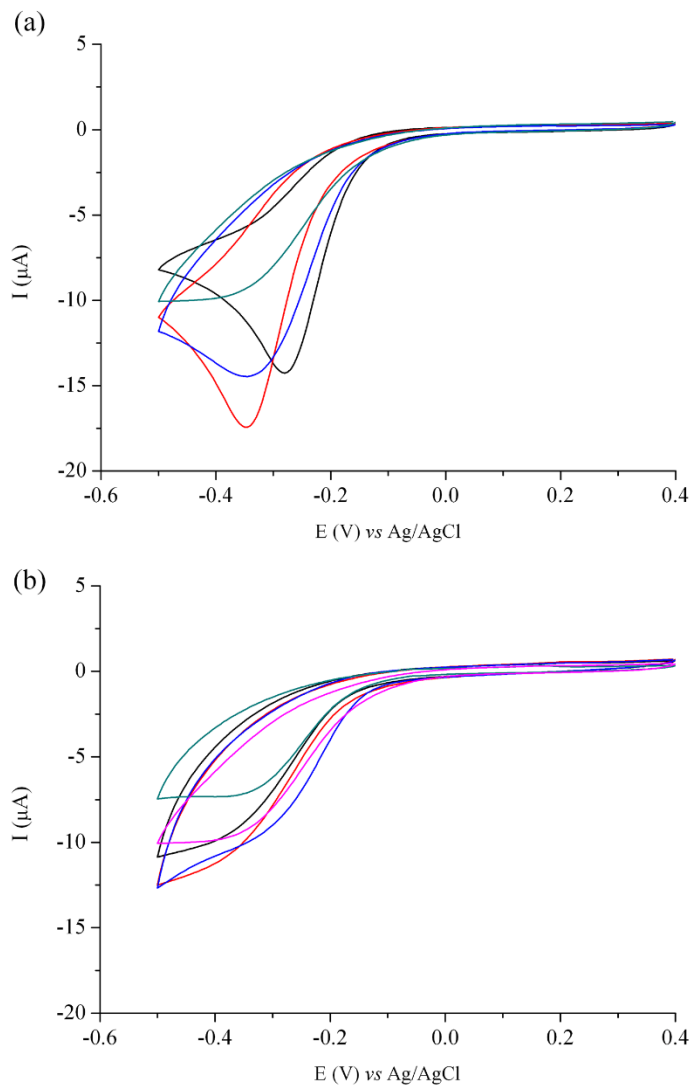
Figure 3.6. (a) CV analysis of FeMC6*a at 10%(*v/v*) TCE (black line), 20%(*v/v*) TFE (blue line), 20%(*v/v*) HFIP (red line). The CV is compared with those obtained in buffer only (grey line).   (b) CV analysis of FeMC6*a at 20%(*v/v*) of ethanol (red line), 20%%(*v/v*) methanol (black line), 20%(*v/v*) isopropanol (blue line), 20%(*v/v*) dimethylsulfoxide (grey line). The CV is compared with that obtained in buffer only (pink line).
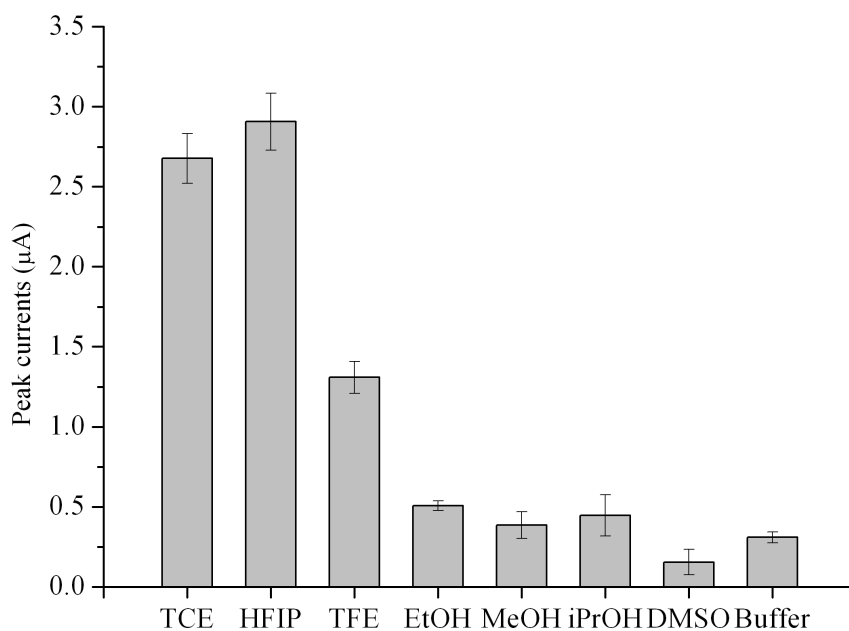
Figure 3.7. Bar chart of the peak currents obtained for the different solvents. All solvents are at 20%(v/v), except for TCE which is instead at 10%(v/v). Data are compared to buffer only.

The CV recorded in the presence of non–halogenated solvents show no changes in peak currents with respect to buffer–only. These experiments prove the selectivity of FeMC6*a@GCE towards halogenated alcohols.

A further selectivity test was performed in the presence of mixed halogenated/non–halogenated solvents by evaluating the peak currents (triplicate experiments).
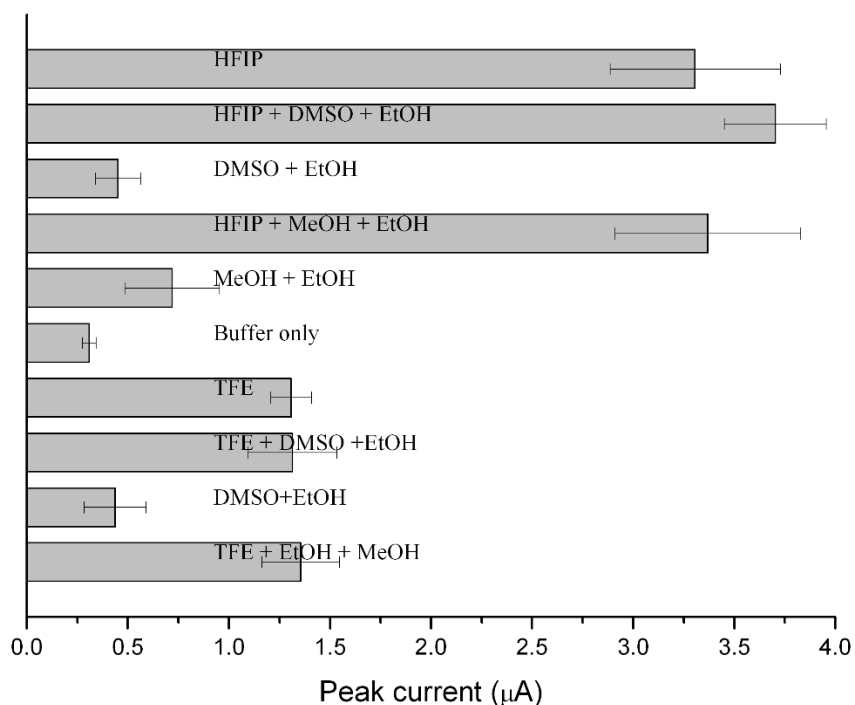
Figure 3.8. Bar chart of the peak currents obtained for different solvent mixtures. All solvents are at 20%(*v/v*) final concentrations. Data are compared to buffer only.

All solvents were added at 20%(*v/v*) final concentration. Several combinations were analyzed, and in all cases no significant decrease in peak currents was observed in the halogenated/non–halogenated solvent mixture compared to halogenated alcohol only (Figure 3.8).

Although FeMC6*a@GCE is not capable of distinguishing between differently halogenated alcohols, it can efficiently discriminate between halogenated and non–halogenated solvents without interferences on the peak current intensity, also when mixed together.

Based on these results, FeMC6*a@GCE proves to be the first selective electrochemical sensor for halogenated alcohols. The proposed method allows for cheap and easy determination of such compounds, in contrast with expensive

methods as a GC-MS detection of similar compounds reported by [Brendan, M. M. and Cort, A. (2000)].

3.2.3 Operational principles in FeMC6*a@GCE sensor for halogenated alcohols

The CV analysis performed in the presence and absence of halogenated alcohols arouse two important questions regarding the operational principles of FeMC6*a@GCE. i) the lack of reversibility of FeMC6*a; ii) the halogenated alcohol effect on peak currents.

3.2.3.1 Oxygen reduction reactions catalyzed by FeMC6*a@GCE

The lack of reversibility upon FeMC6*a reduction might be due to oxygen reduction reaction (ORRs). Porphyrins and heme proteins are widely reported for their ability to carry out ORR [Huang, X. and Groves, J. T. (2018)]. All the CVs obtained for FeMC6*a@GCE in the presence of air in different solvent systems show the presence of a non–reversible peak in the −0.3 to −0.4 V (*vs* Ag/AgCl) region. These electrochemical features are comparable with those reported in literature [Ghatak, S. et al. (2019)] suggesting a O_2 activation mechanism undergoing the reduction of $Fe^{3+}MC6*a$ to its Fe^{2+} species.

Differential pulse voltammetry (DPV) analysis with 20%(*v/v*) of TFE in 100 mM phosphate buffer was carried out in Ar–saturated and air saturated buffers sequentially, using the same electrode. DPV is shown in figure 3.9.
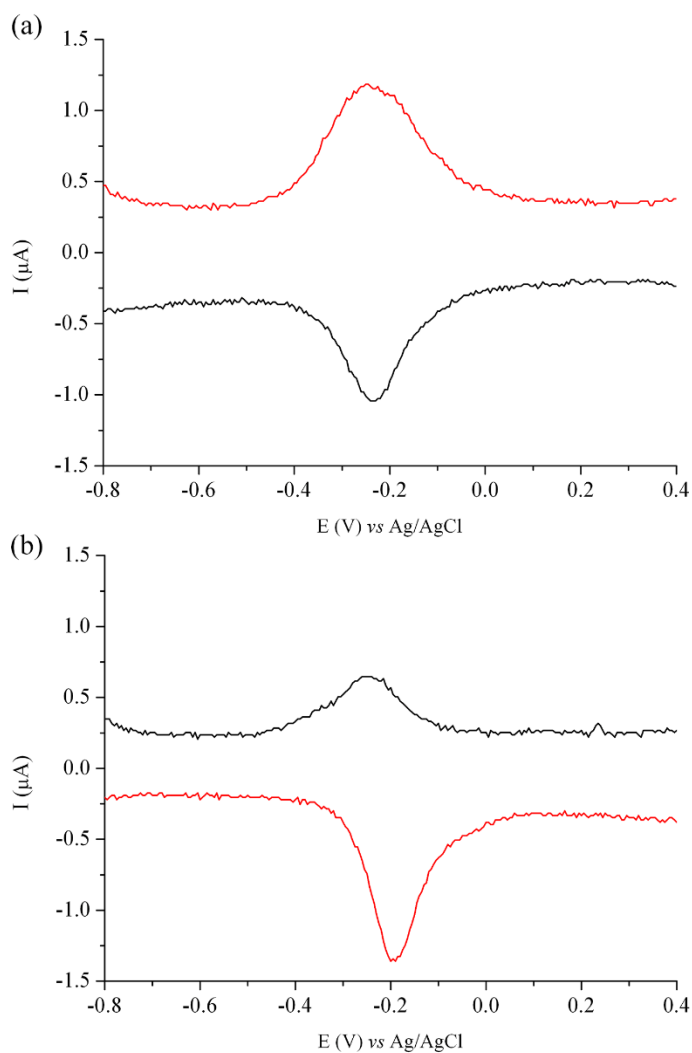
Figure 3.9. DPV in argon saturated (a) and air saturated (b) buffers. Data were collected 20%(v/v) TFE.

FeMC6*a@GCE shows almost symmetric reversible oxidation and reduction peaks at 0.220 V (*vs* Ag/AgCl) in Ar saturated buffer (Figure 3.9a). In air saturated buffer the reversibility is nearly lost (Figure 3.9b), with a decrease of

the intensity of the oxidation peak and an increase in the reduction peak, strongly suggesting chemical oxidation steps.

A further evidence was given by investigation over the electrochemical behavior of FeMC6*a@GCE at different O_2 saturation of the buffer solution. CV in 20%(v/v) of TFE in 100 mM phosphate buffer were acquired with different concentrations of O_2. The superimposition of CV is shown in Figure 3.10.
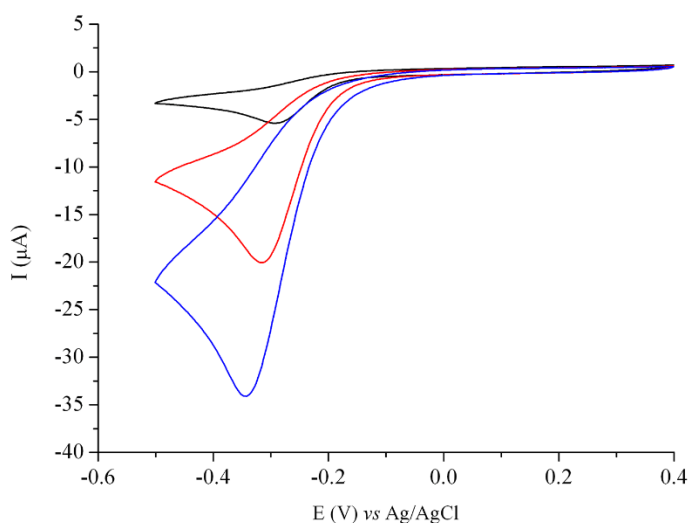
Figure 3.10. CVs in oxygen depleted (black line) and air saturated (red line) and oxygen saturated (blue line) buffers. CVs were recorded in 20%(v/v) TFE.

As illustrated in Figure 3.10 a dramatic increase in currents is observed in O_2–saturated buffer (~35 µA) compared to O_2–depleted buffer (~5 µA), whereas air–saturated buffer lies in the middle (~20 µA). By comparing with literature, these experiments provide enough data to address a concentration–dependent electrocatalytic ORR [Dey, A. et al. (2019)].

Although the DPV and CV experiments confirm a ORR mechanism undergoing the reduction of FeMC6*a, further efforts were devoted to obtain more detailed information regarding the mechanism undergoing FeMC6*a–catalyzed ORR. To this aim, steady state Tafel slope analysis [Shinagawa, T. et al. (2015)] was

carried out. Tafel analysis allows for quantitative measurement of potential-dependent kinetics, by correlating the electric current to the applied potential [Fang, Y.-H. and Liu, Z.-P. (2014); Pizarro, A. et al. (2018)]. The measurements were made in 100 mM phosphate buffer pH 6.5 with 20%(*v/v*) TFE and without TFE for comparison. Steady state currents were acquired for FeMC6*a immobilized onto conductive porous carbon paper to increase the surface area. Figure 3.11 shows the ln(I) *vs* potential. The linear fitting of the data points allowed to derive the Tafel slopes.
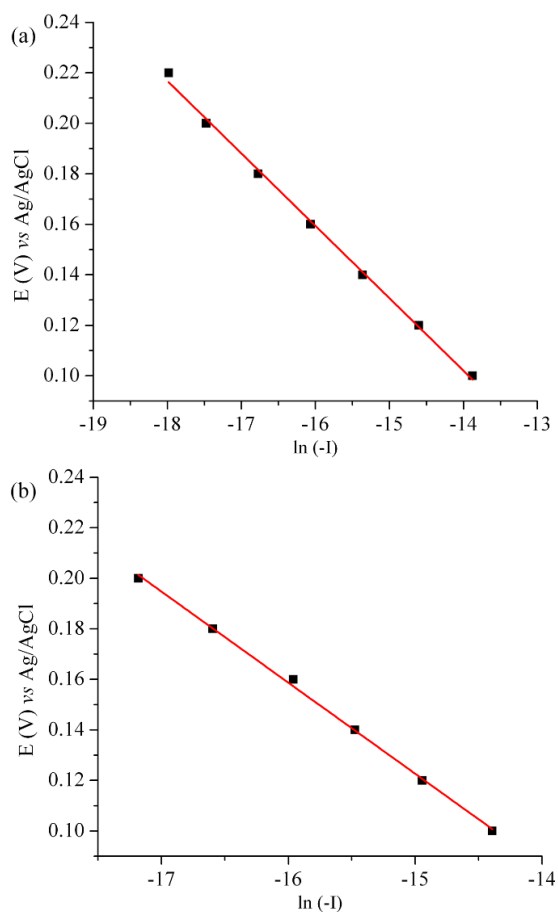
Figure 3.11. Tafel plots obtained from steady–state currents in 100 mM phosphate buffer pH 6.5 (a) and 100 mM phosphate buffer pH 6.5 with 20%(*v/v*) TFE.

In both cases a wide linear range was observed in the ln(I)–E plot. The slopes obtained with TFE were ~30 mV/decade and ~40 mV/decade, with and without TFE, respectively. These values were compared to those reported in literature by [Fletcher, S. (2009)]. A ~30 mV/decade slope might indicate a mechanism involving two sequential electron step, followed by a chemical rate–limiting step. In contrast, the interpretation of a ~40 mV/decade Tafel slope was inconclusive as no direct interpretation can be made. Possibly, this value might arise from multiple mechanism simultaneously occurring.

Even though the ORR mechanism could not be precisely determined, sufficient evidences were collected to prove that the non–reversible behavior of FeMC6*a@GCE arises from an intrinsic ORR activity, in which, the reduction of the catalyst by the electrode is followed by one chemical reoxidation or sequential reduction–oxidation steps, using O_2 as substrate. Further experiments will be devoted to fully understand the ORR catalyzed by FeMC6*a.

3.2.3.2 Effect of halogenated alcohols on FeMC6*a@GCE peak currents

TFE is widely known as folding cosolvent, as it destabilizes hydrophobic interactions while promoting the formation of hydrogen bonds between close residues in the peptide chain [Hamada, D. et al. (2000); Povey, J. F. et al. (2007)]. X-ray scattering demonstrated that fluorinated alcohols are able to arrange as micelle-like clusters in water, with dimensions related to the percentage of fluorinated alcohol in solution [Hong, D.-P. et al. (1999); Reiersen, H. and Rees, A. R. (2000)]. Due to the ability of TFE to interact with water molecules, a "push and pull" mechanism might explain the TFE-assisted folding [Reiersen, H. and Rees, A. R. (2000); Vitale, R. et al. (2015)]. At low TFE percentages (0-10%) a "pull phase" takes place, in which amino acid side

chains are surrounded both by non-fully stabilized TFE clusters and water molecules. At higher percentages (until 50%), clusters become larger and more stabile so that TFE molecules can directly interact with amino acid hydrophobic side chains, thus providing a matrix assisted driving force for folding (push phase). Molecular dynamics simulations provided by [Roccatano, D. et al. (2002)] confirmed that TFE clusters assist with the folding, by promoting the formation of local peptide interactions, thus originating an ordered secondary structure.

Previous catalytic studies on FeMC6*a highlighted a relationship between the catalytic activity and the presence of fluorinated alcohols. As mentioned in a recent paper [Caserta, G. et al. (2018)], the helical content (measured as θ_{222}) and v_0 (as rate of reaction in ABTS oxidation) are strictly dependent. More specifically, an increase in the TFE concentration increases the helical content, thus structuring the peptides into a helix–heme–helix sandwich and enhancing the catalytic properties of FeMC6*a.

A similar enhancement of the catalytic activity might be provided also by halogenated alcohols in ORR. To prove this, far–UV circular dichroism (CD) spectra were acquired by using different solvents (TFE, HFIP, water, methanol, ethanol, isopropanol) 20%(v/v) in 100 mM phosphate buffer pH 6.5 and θ_{222} values were acquired. Then, the θ_{222} were plotted as function of peak currents in the same solvent conditions (Figure 3.12). Due to TCE and DMSO absorbance in the far UV region, acquisition of the CD spectra was not possible for these solvents.
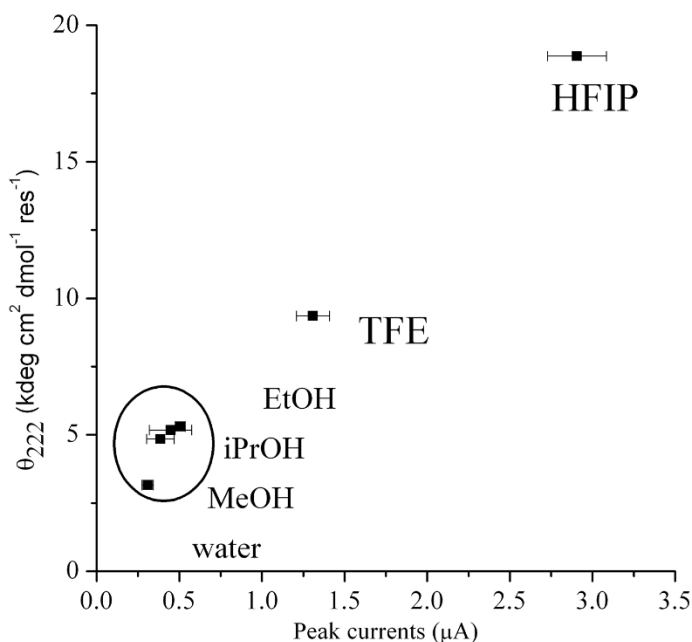
Figure 3.12. Plot of θ_{222} as function of peak currents.

Non–halogenated solvents show low values both in current and θ_{222} and are clustered in the low–left end of the plot, being low both in currents and θ_{222}, while TFE and HFIP occupy middle–high–right end of the plot.

These data strongly suggest a tight correlation between helical content and ORR electrocatalytic activity: similarly to ABTS oxidation, the increase in helical content leads to an increase in the catalytic activity of FeMC6*a. Therefore, the increase in observed peak currents upon folding–alcohols addition could be explained either by an increased amount of active catalyst involved in the ORR or more likely by an enhancement of the catalytic properties of the enzyme, leading to higher turnover number in ORR. In both cases, a greater number of electrons are withdrawn from the electrode, thus causing increase in peak currents.

3.2.4 **Analytical performances of FeMC6*a@GCE**

To evaluate the analytical performances of the FeMC6*a@GCE electrochemical sensor the peak currents at different concentrations of TFE, HFIP and TCE extracted by CV were plotted as function of solvent percentage %(*v/v*) and reported in Figure 3.13a-b-c.
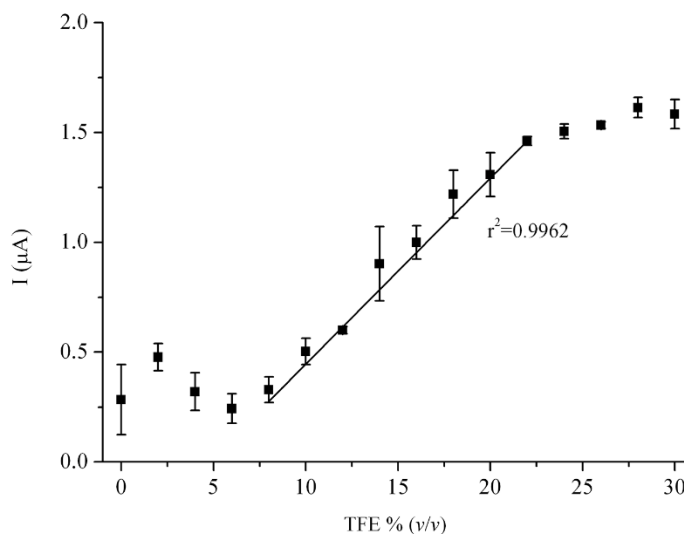
Figure 3.13a. Calibration curve obtained reporting peak currents obtained at 2%(*v/v*) steps of TFE as function of %(*v/v*) TFE.
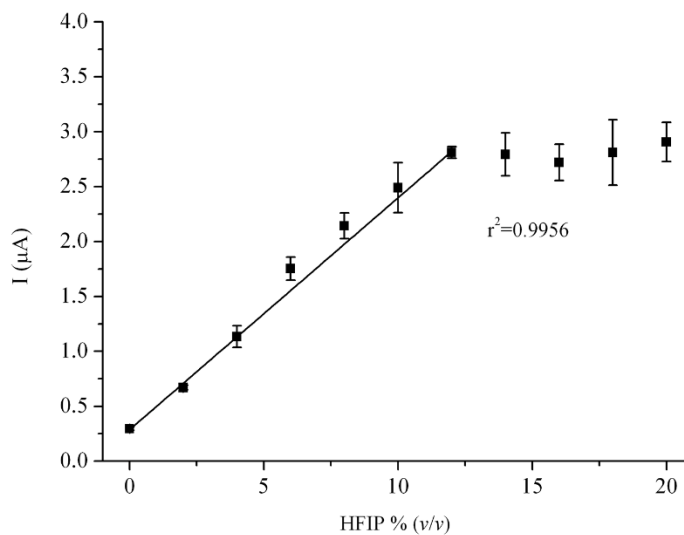
Figure 3.13b. Calibration curve obtained reporting peak currents obtained at 2%(*v/v*) steps of HFIP as function of %(*v/v*) HFIP.
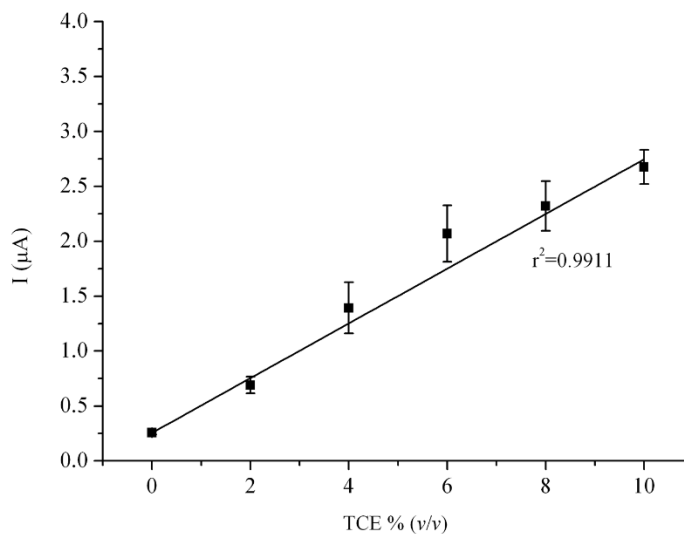
Figure 3.13c. Calibration curve obtained reporting peak currents obtained at 2%(*v/v*) steps of TCE as function of %(*v/v*) TCE.

All calibration curves were acquired in triplicate and good linearity correlation was achieved for all solvents investigated. As shown in the calibration curves, the cathodic peak current of the FeMC6*a@GCE is linearly proportional to halogenated alcohols concentration over the range of 6–22 % (v/v) for TFE, 0–12 % (v/v) for HFIP and 0–10 % (v/v) for TCE. TFE shows a lag phase in the 0–6 % (v/v), whereas both TFE and HFIP show a plateau at 22%(v/v) and 12%(v/v), respectively. TCE was not investigated at higher %(v/v) due to the miscibility in water.

3.3 Conclusions and future perspectives

With this work, we demonstrated that FeMC6*a can be efficiently used for bioelectrochemical purposes. When immobilized onto electroconductive surfaces it shows an oxygen dependent non–reversible behavior. Steady state current experiments confirmed the ORR pathway, but the mechanism involved still remains to be clarified. Further efforts will also be devoted to achieve a thorough overview over the mechanism undergoing the ORR properties of FeMC6*a.

The proposed sensor is, to the best of our knowledge, the first sensor in which the operational principle relies on the use of an enzyme with a positive switched amperometric detection of organic solvents mixtures in water. Moreover, this is the first sensor for determination of TFE, HFIP and TCE in solution. The easy preparation and set–up of the electrode allows for future applications of FeMC6*a@GCE in solvent sensing, miniaturization and integration in more compact and inexpensive systems such as screen printed graphite electrodes. Furthermore, the extremely high sensitivity of FeMC6*a@GCE towards dioxygen can be exploited for future application as O_2 sensor in aqueous environment.

3.4 **Materials and methods**

Nafion polymer 5 %(w/v) solution in aliphatic alcohols, TFE, HFIP and TCE, ethanol, methanol, isopropanol, dimethylsulfoxide were purchased from Sigma–Aldrich (USA). Disodium hydrogen phosphate monohydrate and sodium dihydrogen phosphate were purchased from Merck (Darmstadt, Germany). Phosphate buffer solution was prepared by mixing Na_2HPO_4 and NaH_2PO_4 stock solution. All chemicals were of analytical grade and used without any further treatment. Deionized water from a MilIi–Q System was used throughout. All electrodes used in this work were purchased from BASi (West Lafayette, Indiana, USA).

All electrochemical measurements were performed with a CompactStat potentiostat (Ivium, Netherlands) at room temperature with a conventional three–electrode system comprising a platinum wire as the counter electrode, a glassy carbon working electrode, and a silver/silver chloride (Ag/AgCl) electrode as the reference. Alternatively, carbon paper (AvCarb GDS2230CV) was used as working electrode (1 cm^2 area). Measurements were performed at a scan speed of 50 mV/s. DPV measurements were carried out in a –0.8–0.4 V (*vs* Ag/AgCl) potential window, with a pulse time of 20 ms, pulse amplitude of 20 mV, and scan rate of 20 mV/s. Steady-state currents were acquired by registering currents at fixed potential for 10 minutes, at 0.02 V intervals. IVIUM software (Ivium, Netherlands) was used for electrochemical data analysis and peak current extraction. Data were analyzed with Origin Lab (8.0 version).

CD spectra were obtained at 25°C on a Jasco J–815 dichrograph. Data were collected from 260 to 190 nm (0.2 nm intervals, 20 nm min^{-1} scan speed,1 nm bandwidth, at 16 s response). Cuvette path length of 1.0 cm was used. CD intensities are reported as molar ellipticity per residue (kdeg cm^2 $dmol^{-1}$ res^{-1}), calculated by dividing the total molar ellipticity by the number of amino acids in the molecule. All spectra were collected at 2.0 10^{-6} M sample concentration, in

10 mM phosphate buffer (pH 6.5), with different solvents, all at 20% (v/v) concentrations. All data were blank subtracted.

3.4.1 **Electrochemical measurements**

Prior to coating, GCEs were polished with 0.05 μm alumina and sonicated in deionized water three times. They were then treated in 6% aqueous hydrochloric acid for 10 min, followed by rinsing and sonication in water and acetone successively. A Nafion–FeMC6*a mixture was prepared by mixing 10 µL of 5 % (w/v) Nafion solution in aliphatic alcohols with 4 µL of FeMC6*a aqueous stock solution with 0.1 % (v/v) TFA ($1.5 \cdot 10^{-3}$ M). From the resulting mixture, 7 µL were withdrawn and casted onto a polished and dried GCE. The Nafion–FeMC6*a layer was allowed to dry and cure for 30 minutes at room temperature. Finally, prior use, the electrode surface was flushed with highly pure N_2 for 2 minutes to finalize drying process.

Immobilization of FeMC6*a onto carbon paper was performed by dropcasting 20 µL of FeMC6*a/Nafion solution (6 µL of FeMC6*a $1.5 \cdot 10^{-3}$ M and 14 µL of Nafion 5%(w/v)).

Air, N_2 or O_2 saturated buffers were prepared by bubbling the gas in the buffer for at least 1 h prior measurements.

3.5 **References**

- M. M. Brendan, A. Cort "Determination of halogenated mono-alcohols and diols in water by gas chromatography with electron-capture detection" J. Chromatogr. A, 866 (2000), 1, 65-77.

- C. T. Choma, J. D. Lear, M. K. Nelson, P. L. Dutton, D. E. Robertson, W. F. DeGrado "Design of a heme–binding four–helix bundle" J. Am. Chem. Soc. 116 (1994), 856–865.

- M. J. Eddowes and H. A. O. Hill "Novel method for the investigation of the electrochemistry of metalloproteins: cytochrome c" J. Chem. Soc., Chem. Commun. 21(1977), 771–772.

- Y.-H. Fang, Z.-P. Liu "Tafel kinetics of electrocatalytic reactions: from experiments to first principles" ACS Catal. 4 (2014), 4364-4376.

- B. A. Fry, L. A. Solomon, P. L. Dutton, C. C. Moser "Design and engineering of a man–made diffusive electron–transport protein" Biochim. Biophys. Acta 1857 (2016), 513–521.

- S. Ghatak, S. Bhakta, A. Bhunia, A. Dey "Influence of the distal guanidine group on the rate and selectivity of O_2 reduction by iron porphyrin" Chem. Sci. 10 (2019), 9692–9698.

- D. Hamada, F. Chiti, J. I. Guijarrom M. Kataoka, N. Taddei, C. M. Dobson "Evidence concerning rate-limiting steps in protein folding from the effects of trifluoroethanol" Nat. Struct. Biol. 7 (2000), 58-61.

- D.-P. Hong, M. Hoshino, R. Kuboi, Y. Goto "Clustering of Fluorine-Substituted Alcohols as a Factor Responsible for Their Marked Effects on Proteins and Peptides" J. Am. Chem. Soc. 121 (1999), 37, 8427- 8433

- P. Hosseinzadeh, Y. Lu "Design and fine–tuning redox potentials of metalloproteins involved in electron transfer in bioenergetics" Biochim. Biophys. Acta – Bioenergetics, 1857 (2016), 5, 557–581.

- X. Huang, J. T. Groves "Oxygen Activation and Radical Transformations in Heme Proteins and Metalloporphyrins" Chem. Rev. 118 (2018), 2491–2553.

- C. Kaçar C, B. Dalkiran, P. E. Erden, E. Kılıç (2014) "An amper– ometric hydrogen

peroxide biosensor based on Co_3O_4 nanoparticles and multiwalled carbon nanotube modified glassy carbon electrode" Appl. Surf. Sci. 311 (2014),139–146.

- E. Katz, L. Sheeney–Haj–Ichia, I. Willner "Magneto–switchable electrocatalytic and bioelectrocatalytic transformations" Chemistry 8 (2002), 4138–4148.

- J. G. Kleingardner, B. Kandemir, K. L. Bren Hydrogen evolution from neutral water under aerobic conditions catalyzed by cobalt microperoxidase–11. J. Am. Chem. Soc. 136 (2014), 4–7.

- Imlay, J. A. "Iron–sulphur clusters and the problem with oxygen" Mol. Microbiol. 59 (2006), 1073–1082.

- C. Lee, G. Liu, C. K. Heng, S. N. Tan, T. M. Lim, Y, Lin "Sensitive Electrochemical Detection of Horseradish Peroxidase at Disposable Screen-Printed Carbon Electrode" Electroanalysis 20 (2008), 18, 2040–2046.

- Y.P. Li, H.B. Cao, Y. Zhang "Electrochemical dechlorination of chloroacetic acids (CAAs) using hemoglobin–loaded carbon nanotube electrode." Chemosphere 63 (2006), 359–364.

- R. Lichtenstein, T. A. Farid, G. Kodali, L. A. Solomon, J. L. R. Anderson, M. M. Sheehan, N. M. Ennist, B. A. Fry, S. E. Chobot, C. Bialas, J. A. Mancini, C. T. Armstrong, Z. Zhao, T. V. Esipova, D. Snell, S. A. Vinogradov, B. M. Discher, C. C. Moser, P. L. Dutton "Engineering oxidoreductases: maquette proteins designed from scratch" Biochem. Soc. Trans. 40 (2012), 561–566.

- J. Liu, S. Chakraborty, P. Hosseinzadeh, Y. Yu, S. Tian, I. Petrik, A. Bhagi, Y. Lu "Metalloproteins Containing Cytochrome, Iron–Sulfur, or Copper Redox Centers" Chem. Rev. 114 (2014), 4366−4469.

- A. Lombardi, D. Marasco, O. Maglio, L. Di Costanzo, F. Nastri, V. Pavone "Miniaturized metalloproteins: Application to iron–sulfur proteins" Proc. Natl. Acad. Sci. USA 97 (2000), 22, 11922–11927.

- H. Lu, J. Yang, J. F. Rusling, N. Hu, "Vapor-Surface Sol-Gel Deposition of Titania Alternated with Protein Adsorption for Assembly of Electroactive, Enzyme-Active Films" Electroanalysis 18 (2006), 379–390.

- Y. Luo, H. Liu, Q. Rui, Y. Tian "Detection of Extracellular H2O2 Released from Human Liver Cancer Cells Based on TiO2 Nanoneedles with Enhanced Electron

Transfer of Cytochrome c" Anal. Chem. 81 (2009), 3035–3041.

- E. R. G. Main, J. J. Phillips, C. Millership "Repeat protein engineering: creating functional nanostructures/biomaterials from modular building blocks" Biochem. Soc. Trans. 41 (2013), 5, 1152–1158.

- S. I. Mann, T. Heinisch, A. C. Weitz, M. P. Hendrich, T. R. Ward, A. S. Borovik "Modular artificial cupredoxins" J. Am. Chem. Soc. 138 (2016), 9073–9076.

- M. Marquitan, M. D. Mark, A. Ernst, A. Muhs, S. Herlitze, A. Ruff, W. Schuhmann "Glutamate detection at the cellular level by means of polymer/enzyme multilayer modified carbon nanoelectrodes" J. Mater. Chem. B (2020), C9TB02461A

- S. M. Mejias, Z. Bahrami–Dizicheh, M. Liuktus, D. J. Sommer, A. Astashkin, G. Kodis, G. Ghirlanda, A. L. Cortajarena "Repeat proteins as versatile scaffolds for arrays of redox–active FeS clusters" Chem. Commun. 55 (2019), 3319–3322.

- J. Meyer "Iron–sulfur protein folds, iron–sulfur chemistry, and evolution" J. Biol. Inorg. Chem. 13 (2008), 157–170.

- R. D. Milton, S. D. Minteer. "Direct enzymatic bioelectrocatalysis: differentiating between myth and reality" J. R. Soc. Interface 14 (2017), 131.

- C. Moser, M. M. Sheehan, N. M. Ennist, G. Kodali, C. Bialas, M. T. Engelander, B. M. Discher, P. L. Dutton "De novo construction of redox active proteins" Methods Enzymol. 580 (2016), 365–388.

- V. Nanda, M. M. Rosenblatt, A. Osyczka, H. Kono, Z. Getahun, P. L. Dutton, J. G. Saven, W. F. DeGrado "De novo design of a redox active minimal rubredoxin mimic" J. Am. Chem. Soc. 127 (2005), 5804-5805.

- V. Nanda, S. Senn, D. H. Pike, A. Rodriguez–Granillo, W. A. Hansen, S. D. Khare, D. Noy Structural principles for computational and de novo design of 4Fe–4S metalloproteins. Biochim. Biophys. Acta 1857 (2016), 531–538.

- F. Nastri, D. D'Alonzo, L. Leone, G. Zambrano, V. Pavone, A. Lombardi "Engineering Metalloprotein Functions in Designed and Native Scaffolds" Trends Biochem. Sci. 12 (2019), 1022–1040.

- T. Nöll, G. Nöll "Strategies for "wiring" redox–active proteins to electrodes and applications in biosensors, biofuel cells, and nanotechnology" Chem. Soc. Rev. 40 (2011), 3564–3576.

- D. Özdemir, C. Kaçar, B. Dalkıran, S. Küçükkolbaşı, P. E. Erden, E. Kılıç "Effect of hexaammineruthenium chloride and/or horseradish peroxidase on the performance of hydrogen peroxide (bio)sensors: a comparative study" J. Mater. Sci. 54 (2019), 5381–5398.

- A. Pizarro, G. Abarca, C. Gutiérrez-Cerón, D. Cortés-Arriagada, F. Bernardi, C. Berrios, J. F. Silva, M. C. Rezende, J. H. Zagal, R. Oñate, I. Ponce "Building Pyridinium Molecular Wires as Axial Ligands for Tuning the Electrocatalytic Activity of Iron Phthalocyanines for the Oxygen Reduction Reaction" ACS Catal. 8 (2018), 8406-8419.

- J. S. Plegaria, M. Duca, C. Tard, T. J. Friedlander, A. Deb, J. E. Penner–Hahn, V. L. Pecoraro "De novo design and characterization of copper metallopeptides inspired by native cupredoxins" Inorg. Chem. 54 (2015), 9470–9482.

- J. S. Plegaria, C. Herrero, A. Quaranta, V. L. Pecoraro "Electron transfer activity of a de novo designed copper center in a three–helix bundle fold" Biochim. Biophys. Acta 1857 (2016), 522–530.

- J. F. Povey, C. M. Smales, S. J. Hassard, M. J. Howard "Comparison of the effects of 2,2,2-trifluoroethanol on peptide and protein structure and function" J. Struct. Biol. 157 (2007), 329-338.

- L. Qian, X. Yang "Composite film of carbon nanotubes and chitosan for preparation of amperometric hydrogen peroxide biosensor" Talanta 68 (2006), 3, 721–727.

- Ramanavicius, A. Kausaite, A. Ramanaviciene "Biofuel cell based on direct bioelectrocatalysi". Biosens. Bioelectron. 20 (2005), 1962–1967.

- V. Rahemi, S. Trashin, Z. Hafiddedine, S. Van Doorslaer, V. Meynen, L. Gorton, K. De Wael "Amperometric Flow-Injection Analysis of Phenols Induced by Reactive Oxygen Species Generated under Daylight Irradiation of Titania Impregnated with Horseradish Peroxidase" Anal. Chem. 92 (2020), 5, 3643-3649.

- A. Ranieri, C. A. Bortolotti, G. Di Rocco, G. Battistuzzi, M. Sola, M. Borsari "Electrocatalytic Properties of Immobilized Heme Proteins: Basic Principles and Applications" ChemElectroChem. 6 (2019), 5172–5185.

- H. Reiersen, A. R. Rees "Trifluoroethanol may form a solvent matrix for assisted hydrophobic interactions between peptide side chains" Protein Eng., Des. Sel., 13

(2000), 739–743.

- Renault, C. P. Andrieux, R. T. Tucker, M. J. Brett, V. Balland, B. Limoges "Unraveling the mechanism of catalytic reduction of O_2 by microperoxidase–11 adsorbed within a transparent 3D–nanoporous ITO film" J. Am. Chem. Soc. 134 (2012), 6834–6845.

- E. Robertson, R. S. Farid, C. C. Moser, J. L. Urbauer, S. E. Mulholland, R. Pidikiti, J. L. Lear, A. J. Wand, W. F. DeGrado, P. L. Dutton "Design and synthesis of multi–haem proteins" Nature 368 (1994), 425–432.

- D. Roccatano, G. Colombo, M. Fioroni and A. E. Mark, "Mechanism by which 2,2,2–trifluoroethanol/water mixtures stabilize secondary–structure formation in peptides: A molecular dynamics study" Proc. Natl. Acad. Sci. USA 99 (2002), 12179–12184.

- Roy, I. Sarrou, M. D. Vaughn, A. V. Astashkin, G. Ghirlanda "De Novo Design of an Artificial Bis[4Fe–4S] Binding Protein" Biochemistry 52 (2013), 43, 7586–7594.

- T. Shinagawa, A. T. Garcia–Esparza, K. Takanabe "Insight on Tafel slopes from a microkinetic analysis of aqueous electrocatalysis for energy conversion" Sci. Rep. 5 (2015), 13801.

- X. Song, J. Wang, J. Chen, Q. Liu "Bioelectrocatalytic Dechlorination of Trichloroacetic Acid by Hemoglobin Modified Graphite Electrode in Aqueous Solutions of Different pH and Temperature" Int. J. Electrochem. Sci. 7 (2012) 10519 – 10529.

- Z.R. Sun, H. Ge, X. Hu, Y.Z. Peng "Preparation of foam–nickel composite electrode and its application to 2,4–dichlorophenol dechlorination in aqueous solution" Sep. Purif. Technol. 72 (2010), 133–139.

- A. G. Tebo, T. B. J. Pinter, R. García-Serres, A. L. Speelman, C. Tard, O. Sénéque, G. Blondin, J. –M. Latour, J. Penner-Hahn, N. Lehnert, V. L. Pecoraro "Development of a rubredoxin-type center embedded in a de novo-designed three-helix bundle" Biochemistry, 57 (2018), 16, 2308-2316.

- S. Tiziani, F. Sussich, A. Cesàro "The kinetics of periodate oxidation of carbohydrates 2. Polymeric substrates" Carbohydr. Res. 1 (2003), 10, 1083-1095.

- R. Vitale, L. Lista, S. Lau–Truong, R. T. Tucker, M. J. Brett, B. Limoges, V.

Pavone, A. Lombardi and V. Balland "Spectroelectrochemistry of Fe(III) and Co(III)–mimochrome VI artificial enzymes immobilized on mesoporous ITO electrodes" Chem. Commun. 50 (2014), 1894–1896.

- T. Wang, L. Wang, J. Tu, H. Xiong, S. Wang "Core–shell structured Ag@C for direct electrochemistry and hydrogen peroxide biosensor applications" Bioelectrochemistry 94 (2013), 94–99.

- T. S Wong, U. Schwaneberg "Protein engineering in bioelectrocatalysis" Curr. Opin. Biotech. 14 (2003), 590–596.

- S. –H. Wu, X.-B. Huang, Y- Tang, L.-M. Ma, Y. Liu, J.-J. Sun "Temperature controllable electrochemical sensors based on horseradish peroxidase as electrocatalyst at heated Au disk electrode and its preliminary application for H_2O_2 detection" Anal. Chim. Acta 1096 (2020), 44-52.

- Y. Xin, X. Fu–bing, L. Hong–wei, W. Feng, C. Di–Zhao, W. Zhaoyang "A novel H_2O_2 biosensor based on Fe_3O_4–Au magnetic nanoparticles coated horseradish peroxidase and graphene sheets–Nafion film modified screen–printed carbon electrode" Electrochim. Acta 109 (2013), 750–755.

- H. Xu, H. Y. Xiong, Q. X. Zeng, L. Jia, Y. Wang, S. F. Wang, "Direct electrochemistry and electrocatalysis of heme proteins immobilized in single–wall carbon nanotubes–surfactant films in room temperature ionic liquids" Electrochem. Commun. 11 (2009), 286–289.

- S. Yanagisawa, M. J. Banfield, C. Dennison "The role of hydrogen bonding at the active site of a cupredoxin: the Phe114Pro azurin variant" Biochemistry 45 (2006), 8812–8822.

- X. Yang, X. Chen, X. Zhang, W. Yang, D. G. Evans "Direct electrochemistry and electrocatalysis with horseradish peroxidase immobilized in polyquaternium–manganese oxide nanosheet nanocomposite films" Sens. Actuators B 134 (2008), 182–188.

- Y. Yu, C. Cui, X. Liu, I. D. Petrik, J. Wang, Y. Lu "A Designed Metalloenzyme Achieving the Catalytic Rate of a Native Enzyme" J. Am. Chem. Soc. 137 (2015), 36, 11570–11573.

- Y. Yu, I. D. Petrik, K. N. Chacon, P. Hosseinzadeh, H. Chen, N. J. Blackburn, Y. Lu

"Effect of circular permutation on the structure and function of type 1 bluecopper center in azurin" Protein Sci. 26 (2017), 218–226.

- Zhang, J. Zhou, S. Li, X. Zhang, D. Huang, Y. He, M. Wang, G. Yang, Y. Shen "Hydrogen peroxide sensor based on microperoxidase–11 immobilized on flexible MWCNTs–BC nanocomposite film" Talanta 131 (2005), 243–248.

Chapter 4

Synthetic peroxidases

in bionanomaterials

construction

4.1 **Introduction**

    4.1.1   **Biocatalysis as a smart tool for sustainability**

The current demand of sustainable green methodologies, and the variety of chemical transformations promoted by biocatalysts, make enzymes important tools for emerging industries [Kirk, O. et al. (2002)].

The application of enzymes has great potential into a variety of fields, including pharmaceutical industry and biofuel production, environmental monitoring, disease diagnostics, wastewater treatment and dye bleaching (Table 4.1) [Koeller, K. M. et al. (2001)].

With respect to sustainability and process efficiency, the use of biocatalysts offers numerous benefit over traditional chemical processes. Biodegradability, high reaction selectivity and high catalytic rates under relatively mild conditions and aqueous environment are the main advantages of enzymatic catalysis. However, the reduced stability of biocatalysts in hard conditions and often their short lifetime, hinders practical applications. In fact, enzyme activity is strictly related to the experimental conditions (pH, temperature, solvent) which makes them extremely sensitive to even small changes. Furthermore, they are not easily separated from the reaction mixture; thus leading to high catalysts consumption, time and cost of the analysis and make them non–viable for in continuous processes [Kim, J. et al. (2006)].

      To overcome the drawbacks associated with enzyme applications, optimization of a biocatalytic process is often required. Optimization relates not only to enzyme functionality and operational stability, but also to the potential application in large–scale processes. Therefore, latest research has been carried out to facilitate practical applications of biocatalysts by using immobilization procedures [Zdarta, J. et al. (2018)].

Table 4.1. Industrial application of enzyme catalysis adapted from [Koeller, K. M. et al. (2001)].

Sector	Enzymes	Applications
Pharmaceuticals	Nitrile hydratase, transaminase, monoamine oxidase, lipase, penicillin acylase	Synthesis of intermediates for production of active pharmaceutical ingredients
Food Processing	Trypsin, amylase, glucose isomerase, papain, pectinase	Conversion of starch to glucose, production of high fructose corn syrup, production of prebiotics, debittering of fruit juice
Detergent	Protease, lipase, amylase, cellulase	Stain removal, removal of fats and oils, color retention,
Biofuels	Lipase, cellulase, xylanase	Production of fatty acid methyl esters, decomposition of lignocellulotic material for bioethanol production
Paper and Pulp	Lipase, cellulase, xylanase	Removal of lignin for improved bleaching, improvement in fiber properties

4.1.2 **Gold nanoparticles: interesting matrix for enzyme immobilization**

Compared to the classical immobilization matrices, the use of AuNPs for enzyme immobilization provides important advantages. AuNPs are nanometric structures of atomic gold in the size–range of 1–100 nm. As all nanomaterials, the nanometric size massively increases the surface area to volume ratio, thus enabling high loading of catalyst while minimizing amount of matrix used. This particular feature makes the use of AuNPs cost–effective. Furthermore, AuNPs can be easily synthesized in different sizes with narrow distribution and can be

conjugated to proteins without the use of surfactants and toxic reagents [Daniel, M. C. et al. (2004); Ansari, S. A. et al. (2012)].

Gold nanoparticles employment in catalytic processes allows for easy purification of reaction products, thus leading to many operational and practical benefits. For instance, the centrifugation is a simple and efficient method for separating AuNPs from the reaction mixture, that make them an attractive tool for large–scale enzymatic immobilization. Furthermore, thanks to their inert nature, stability, non–cytotoxicity and biocompatibility these particles are currently being investigated for biological and biomedical applications and for the development of drug delivery systems [Khan, A. et al. 2014)].

4.1.3   **Physico–chemical properties of AuNPs**

It is well known that the reduction of a solid material to dimension of nanometers, drastically changes its properties respect to the macroscopic state. Indeed, the physico–chemical features of gold nanoparticles are very different from those of the corresponding bulk material [Schmidt, G. et al. (1992); Liu, Y. et al. (2014)].

AuNPs show peculiar optical properties, such as an intense color that can shift from red to blue/purple and arises from the localized surface plasmon resonance (LSPR) phenomenon (Figure 4.1). LSPR originates from the coherent oscillation of the conduction band electrons of metallic nanoparticles and the incident light absorption. These resonances are known as surface plasmons and are indeed a small particle effect, since they are absent in the individual atoms as well as in the bulk [Link, S. et al. (1999)].
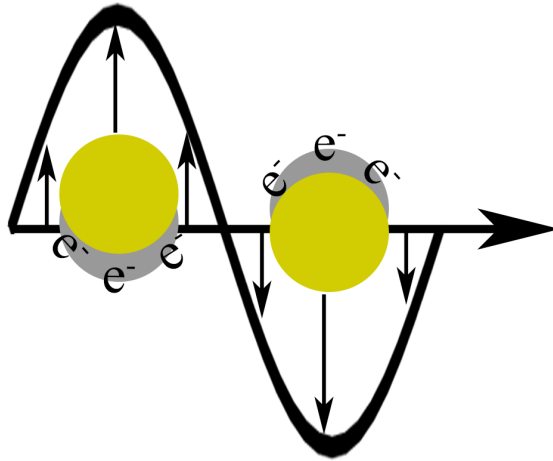
Figure 4.1. Schematic plasmon oscillation for a sphere, and UV–Vis absorption.

A useful feature of the SPRB is the dependence of its position and width on the particle size and stability of colloidal suspension. It is well ascertained, that a red shift and a widening in SPRB occurs upon increasing nanoparticles dimension. For instance, it has been reported that the SPRB maximum shifts from ≈518 nm up to 565 nm, when the particle sizes increase from 9 to ≈ 100 nm (Figure 4.2) [Peng, S. et al. (2010)]. This effect is due to different light–matter interaction, arising when the particle size approaches or moves away from the wavelength of light, and it has been described by [Kreibig, U. et al. (1995)].
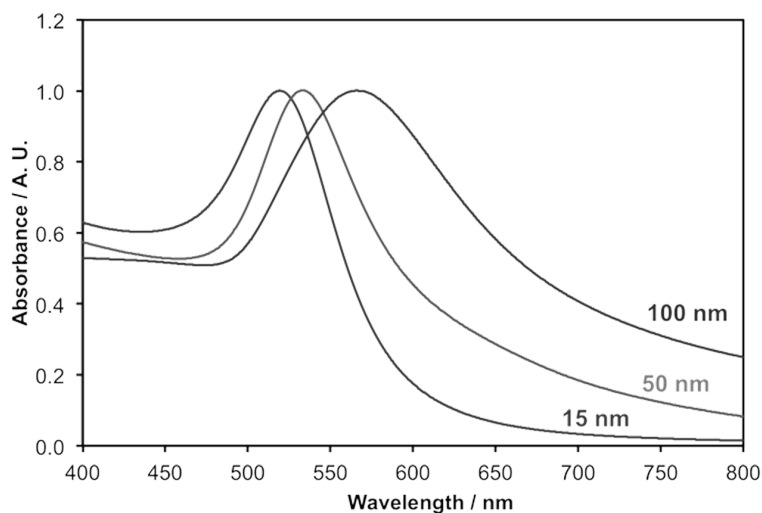
Figure 4.2. Relation between size and SPRB position. Adapted from
www.chembam.com.

As change in particle dimension causes variation in SPRB absorbance, it is possible to determine the size of gold nanoparticles directly from UV–Vis spectrum. Accurate theoretical calculation for the determination of gold nanoparticles diameter can be obtained using the ratio of absorbance of AuNPs at the SPRB (maximum) to the absorbance at 450 nm of AuNPs (Table 4.2) [Haiss, W. et al. (2007)].

The LSPR phenomenon depends not only on the wave frequency and structural parameters (shape, size, and chemical nature) of nanoparticles but also on the distance between nanoparticles. Therefore, aggregation of AuNPs induces variations in absorption spectra accompanied by significant color changes of solutions. Specifically, the aggregation is reflected by a broadening and an increase in the SPRB bandwidth, and a shift to longer wavelengths (700–1100 nm region) [Liz–Marzán, L. M. (2006); Miller, M. and Lazarides, A. A. (2005)].

Table 4.2. AuNPs diameter obtained using the ratio of absorbance of SPRB and 450 nm adapted from [Haiss, W. et al. (2007)].

A_{spr}/A_{450}	d (nm)	A_{spr}/A_{450}	d (nm)	A_{spr}/A_{450}	d (nm)
1.10	3	1.56	12	1.96	40
1.19	4	1.61	14	2.00	45
1.27	5	1.65	16	2.03	50
1.33	6	1.69	18	2.07	55
1.38	7	1.73	20	2.10	60
1.42	8	1.80	25	2.12	65
1.46	9	1.86	30	2.15	70
1.50	10	1.92	35	2.17	75

Colloidal stability is influenced by a high salt concentration. It has been reported that the UV–Vis spectrum of citrate–capped 40 nm gold nanoparticles shows significant aggregation of the particles when the salt concentration increases over 20 mM [Han, X. et al. (2011)]. The AuNPs optical resonance is sensitive on slight changes in the environment they are suspended in. Indeed, the plasmonic absorbance band depends on: temperature presence of passivating ligand, dielectric constant of the medium and refractive index of the medium [Link, S. et al. (2000); Horikoshi, S. et al. (2013); Peceros, K. E. et al (2005)].

SPRB is a versatile signal for studying chemisorption, redox reaction, biosensing, as the nature of the protecting organic shell (passivating layer) plays an important role in the determination of SPRB properties. Changes in the thickness of the passivating layer results in different SPRB shift as reported by [Mulvaney, P. (1996)]. The presence of a stabilizing ligand onto nanoparticles surface, and increases in the passivating shell thickness usually causes red shift in the SPRB maximum absorption [Ghosh, S. K. et al. (2004)].

4.1.4 **AuNPs: functionalization and bioconjugation**

The chemical features of gold make AuNPs surface chemistry particularly interesting. Surface functionalization of AuNPs with small molecules and biomolecules can be performed in an easy and straightforward manner, paving the way for a plethora of applications for AuNPs in different fields [Elahi, N. et al. (2018)]. Furthermore, the addition of ligands covering the gold surface enhances the stability of the colloid, preventing aggregation [Zeng, S. et al. (2011)]. The functionalization of AuNPs can be achieved either during their synthesis, by adding a suitable ligand, or after synthesis [Walper, S. A. et al. (2015)].

AuNPs can be coated with a variety of groups by "ligand exchange" reactions. The rate of this reaction depends on several factors, such as the chain length, steric hindrance and affinity of the ligand to the gold. Many ligands have been investigated as anchor groups for adsorption onto AuNPs surfaces. The most commonly used are thiols, disulfides, carboxylates, thioethers, phosphines and amines. Among them, thiol groups show to be proper passivating material, thanks to the soft character of sulfur enabling strong bond with the soft metal. Indeed, with a strength of 197 kJ/mol, the sulphur–gold bond is considered to ensure stability to nanoparticles coating layer [Di Felice, R. et al. (2004)].

The passivation with organic layer is also useful to modulate the optical, chemical and catalytic properties of the gold core. For instance, AuNPs functionalized with long alkylthiol chains are dispersable only in poorly polar organic solvents, while the coating with carboxyl functionalized alkylthiolates enhances dispersability in polar solvents, such as water [Porter, L. A. et al. (1998)].

The presence of different molecules on the surface can be useful for chemical reactivity of gold nanoparticles. The absorption onto AuNPs of reactive bifunctional ligands allows gold colloids conjugation with a wide variety of

molecules and biomolecules. These conjugated systems offer the possibility of obtaining innovative materials with new capabilities both for basic studies and practical application [Abad, J. M. et al. (2005)].

AuNPs surface can be coated with peptides, enzymes, antibodies, DNA and used in biotechnology and biosensing [Jia, J. et al. (2002)]. Ahirwal et al. reported the use of AuNPs functionalized with to an antibody (Ab1) through a spacer, for the electrochemical immunoassay on Au electrode [Ahirwal G. K. and Mitra C. K. (2010)]. AuNPs have been also used for glucose sensing, heavy metal ions detection and for many other applications. In particular, a huge number of enzyme–based biosensors based on HRP–conjugated AuNPs have been reported. Surprisingly, some of these conjugates exhibit an enhanced catalytic activity over HRP itself [García–Galan, C. et al (2011)]. Further examples involve the electrochemical application of HRP entrapped onto layers of AuNPs–thionine–chitosan absorbed on a glassy carbon electrode (GCE), which was applied as signal amplification system, for the electrochemical biosensing of tetrahydrocannabinol [Lu, D. and Pang, G. A. (2016)]. Similarly, HRP was encapsulated in nanogold hollow spheres and used for signal amplification in the electrochemical detection of hepatitis C virus [Tang, D. et al. (2011)]. In a recent work, the activity of HRP adsorbed onto AuNPs of different sizes was investigated. Interestingly, the catalytic performances of the enzyme were found to be dependent on the hydrodynamic size of the AuNPs, as the k_{cat} of the AuNPs–HRP conjugates decreases with the increase in the size of the AuNPs [Tadepalli, S. et al. (2017)].

However, it must be pointed out that commonly used methods for enzymes conjugation are difficult to control, and conjugation mainly lead to random adsorption and orientation of molecules, yielding catalytic active sites with different accessibility. In this view, an optimized strategy should be based on specific interactions between the biological molecule and functionalized

nanoparticles surface, thus producing proper protein anchoring in a suitable orientation for catalysis. For this purpose, significant efforts in selective protein immobilization field are still required.

Recent advances in organic chemistry have led to the development of some efficient site–specific biomolecules conjugation protocols [Agarwal, P. and Bertozzi, C. R. (2015)]. Among current labeling methods available, bioorthogonal chemistry is emerging as an alternative for NPs functionalization offering the advantage of an intimate control over the site and type of bond formation [Sletten, E. M. et al. (2009)].

4.1.5 Click chemistry: an efficient method for enzymes conjugation and immobilization

Biomolecule labeling and bioconjugation strategies present significant challenges for any ligation methodology since they require reaction procedures that can be performed under physiological conditions, with a reasonable time–scale, involving low toxicity reagents while still ensuring retention of biological function. Among them, Click Chemistry strategies fit the required reactivity, selectivity and biocompatibility criteria. The concept of 'Click chemistry' was first termed in 2001 by Sharpless and co–workers [Kolb, H. C. et al. (2001)], and refers to simple organic reactions carried out under mild conditions (neutral pH, aqueous medium, room temperature) with high yields [Rostovtsev, V. V. et al. (2002)]. Several types of chemical transformations have been grouped under the definition of 'click reactions' over the years [Palomo, J. M. (2012)], including: cycloadditions; nucleophilic substitution chemistry, ring–opening reactions of epoxides or aziridine; formation of ureas, thioureas, aromatic heterocycles, hydrazones, and amides; additions to carbon–carbon multiple bonds, such as epoxidation, dihydroxylation, and sulfenyl halide addition, but also Michael additions [Sletten, E. M. et al. (2009)]. Interesting examples are provided by

"tetrazine ligation" [Blackman, M. L. et al. (2008)], the Staudinger ligation [Schilling, C. I. et al. (2011)], "thiol–ene reaction" [Bhat, T. et al. (2015)] shown in Scheme 4.1. The first is the reaction of a trans–cyclooctene and an s–tetrazine in an inverse–demand Diels Alder reaction followed by a retro–Diels Alder reaction with nitrogen elimination. The reaction proceeds extremely fast with a second order rate constant of $\cong$2000 $M^{-1}s^{-1}$(in 9:1 methanol/water) allowing modifications of biomolecules at extremely low concentrations (Scheme 4.1a). The azide–Staudinger ligation represents the reaction between an azide and an ortho–methylbenzoate phosphine and was described for the first time in 1919 by Hermann Staudinger (Scheme 4.1b). This reaction yields an amide bond, upon intramolecular rearrangement from a iminophosphorane intermediate. Thiol–ene reaction instead, involves efficient reactions of thiols with reactive carbon–carbon double bonds. Thiol–ene chemistry has proved to be an extremely efficient method for the formation of sulfur–carbon bonds in both small–molecule and polymer chemistry. It proceeds either by radical–mediated reaction pathway or following Michael addition mechanism (Scheme 4.1c).
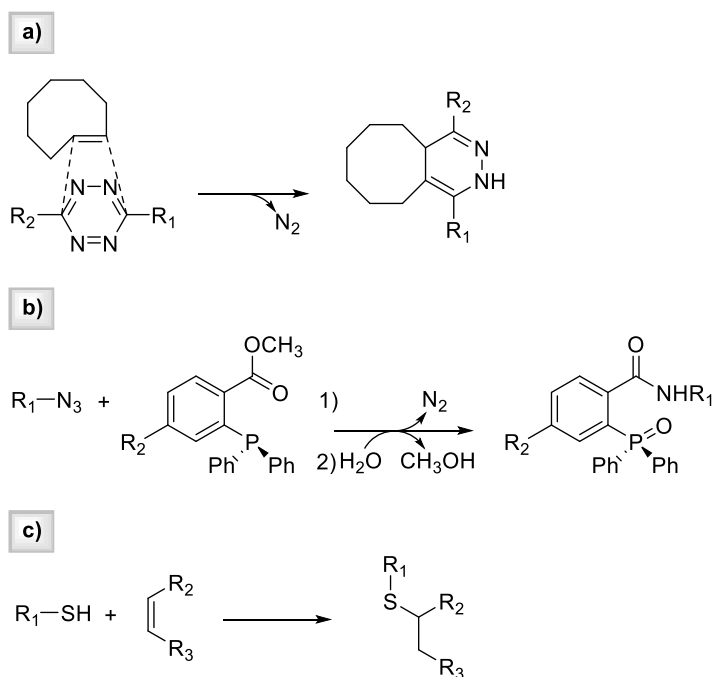
Scheme 4.1. Click reactions examples: a) tetrazine ligation b) Staudinger reaction c) thiol–ene reaction.

This group of quick and quantitative chemical reactions, are capable of producing a wide variety of functional and organic synthetic molecules, independently from solvent and pH. Click reactions, indeed, work well in water and buffers, as well as in organic medium like dimethylsulfoxide, dimethylformamide, acetonitrile and alcohols, in the pH range 4–11.

In particular, a set of click transformations, labelled as "Bioorthogonal reactions", has recently gathered great attention. Although endowed with all the attributes of click reactions, "Bioorthogonal chemistry" identify pairs of functional groups that rapidly and selectively react with each other. By contrast to the 'classical' bioconjugation and biolabeling techniques, bioorthogonal transformations provide a well–defined point of attachment between surfaces and molecules or between two molecules, thanks to the high reactions

selectivity. In this view, bioorthogonal chemistry is well–suited for biological or biomedical purpose, as reactions take place only between click reagents without crossreactivity with the plethora of reactive groups existing in living system and leaving no toxic byproducts behind [Devaraj, N. K. (2018)].

To overcome intrinsic toxicity of the copper(I)–catalyzed [3+2] alkyne azide cycloaddition (Scheme 4.2a) (CuAAC), Bertozzi's group has developed new copper–free AAC strategies, through the employment of alkynes in a strained geometry, as occurs in a cyclooctyne–based ring system [Sletten, E. M. et al. (2009)]. This strain–promoted AAC variant, namely SPAAC, proceeds with the same mechanism but in the absence of copper(I) catalyst, due to the lower activation barrier compared to that of traditional AAC (Scheme 4.2b).
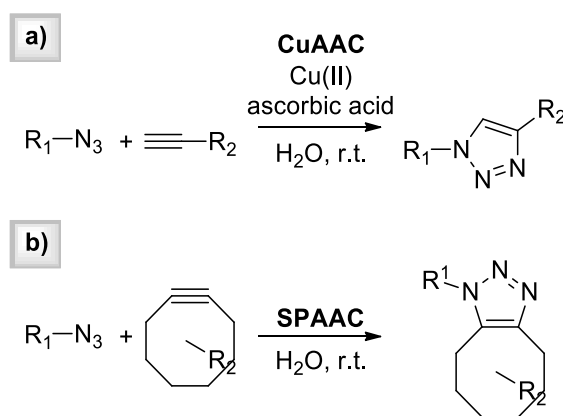
Scheme 4.2. (a) Cu–catalyzed Alkynes Azides cycloaddition (b) Strain–promoted Alkynes Azides cycloaddition.

SPAAC has been exploited as a biocompatible bioorthogonal strategy for the fluorogenic labeling of proteins and is currently used in many chemical applications. Promising studies show that Huisgen 1,3–dipolar cycloaddition and thereby variation, area precious tool in biomolecules coupling technology, thanks to robustness of the linkage and the preservation of biochemical properties of immobilized substrates.

The absence of metal catalysts makes these reactions suitable for dynamic in vivo imaging [Jewett, J. C. et al (2010)], drug discovery [Moses, J. E. and Moorhouse A. D. (2007)], for the functionalization of various surfaces [Kuzmin, A. et al. (2010)], biomolecules modification [Mamidyala, S. K. et al. (2010)] and enzyme bioconjugation [Buhl, M. et al. (2015)].

For instance, promising studies has been reported towards the successful conjugation of HRP to AuNPs by means of click chemistry. In particular, alkyne–HRP was clicked onto azide functionalized AuNPs in the presence of Cu(I) under mild condition (pH 7, 25°C). The enzyme–AuNPs conjugates show catalytic activity in oxidation of ABTS by H_2O_2. The finding that HRP retains its catalytic activity upon conjugation with AuNPs, demonstrates the feasibility of the click chemistry as biomolecule conjugation protocol, and offers new perspectives in the development of nanobioprobes and biosensors (Scheme 4.3) [Zhang, M. X. et al. (2010)].
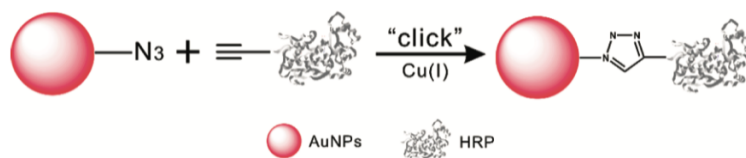
Scheme 4.3. Conjugation of horseradish peroxidase (HRP) via click chemistry. Adapted with permission from [Zhang, M. X. et al. (2010)]. Copyright (2010) American Chemical Society

The large applicability of immobilized enzyme has led us to explore the performances of mimochromes onto AuNPs for further applications in industry and biosensing. AuNPs were chosen as matrix for their straightforward synthesis and easy conjugation. Furthermore, the simplicity in conjugation of mimochromes, exposing only one lysine residue, allows to produce site–selectively derivatized analogues, ready to be tethered to surfaces in an oriented

manner. Previous investigation using a different mimochrome analogue MC6-S6G already proved that miniaturized enzymes could be efficiently conjugated onto gold nanoparticles by direct chemisorption approach, while partially retaining the peroxidase activity [Zambrano, G. et al. (2018)]. In this work, totally synthetic nano–bioconjugates were obtained by means of click chemistry functionalization. Finally, the herein synthesized nanobioconjugate was thoroughly characterized with regards to catalytic performances.

4.2 **Results and discussion**

4.2.1 **Strain promoted alkyne–azide cycloaddition approach**

With the aim to produce Mimochrome@AuNPs conjugates with high catalytic performances, the use of innovative bioorthogonal conjugation methodology, such as strain promoted alkyne–azide cycloaddition (SPAAC) (Scheme 4.4) was applied.
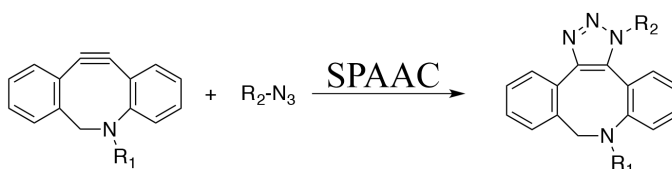
Scheme 4.4. Schematic representation of SPAAC reaction

The functionalization was carried out as follows. First, FeMC6*a was functionalized with the bifunctional linker dibenzoazacyclooctyne–PEG(4)–N–hydroxysuccinimide (DIBAC–PEG(4)–NHS). Then, the linker–modified enzyme was immobilized onto azide–modified AuNPs, and the conjugate was characterized by different techniques such as TEM, UV–Vis and CD spectroscopy (Figure 4.3).

Finally, catalytic assays were performed to determine the kinetic parameters of the immobilized enzyme and compared to those obtained for the linker–modified and unmodified enzyme freely diffusing in solution.
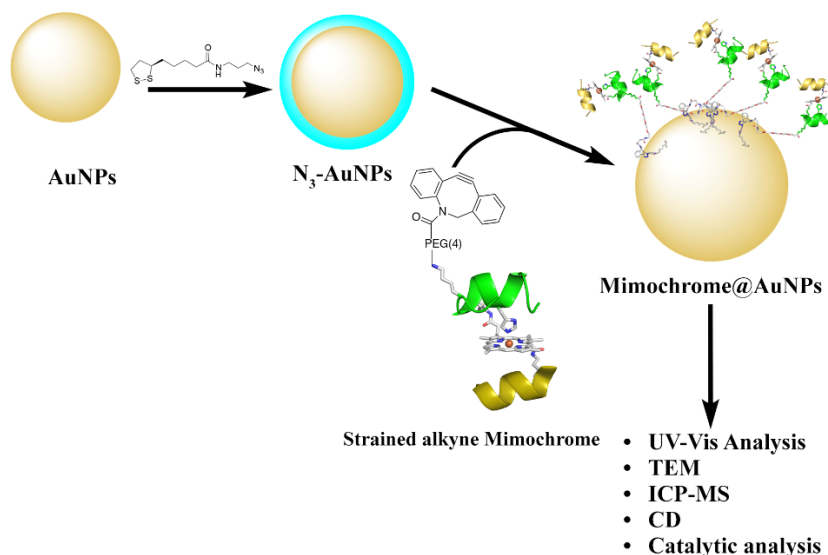
Figure 4.3. Overview on Mimochrome@AuNPs synthesis and characterization

4.2.2 Site–specific modification of FeMC6*a analogue with DIBAC–PEG(4)–NHS

Selective enzyme modification was achieved via chemoselective lysine acylation using NHS active ester [Nanda, J. S. and Lorsch, J. R. (2014)]. Specifically, FeMC6*a, was labeled with DIBAC–PEG(4)–NHS, that, in addition to NHS group, has a long spacer chain (PEG(4)) and a reactive group for click reaction (DIBAC) (Scheme 4.5).

The presence of four PEG units ensures a $\cong 20$ Å average distance between the enzyme and the AuNP surface, providing high conformational freedom to the enzyme. The distance between the enzyme and the surface can possibly create a solution–like environment, preserving FeMC6*a catalytic activity and reducing the possibility of AuNPs coalescence. The linker bears a DIBAC moiety as terminal group, free to react with N_3–moiety, displayed onto AuNPs, in the SPAAC reaction.

Scheme 4.5. FeMC6*a modification using DIBAC–containing linker.

As FeMC6*a bears only one amino group (Lys11 TD) free to react, the conjugation of DIBAC–PEG(4)–NHS produced a site–selective product. The chromatographic analysis of the reaction mixture (Figure 4.4) showed the depletion of FeMC6*a (R_t= 25.6 min) and the appearance of a new peak at R_t 30.9 min.
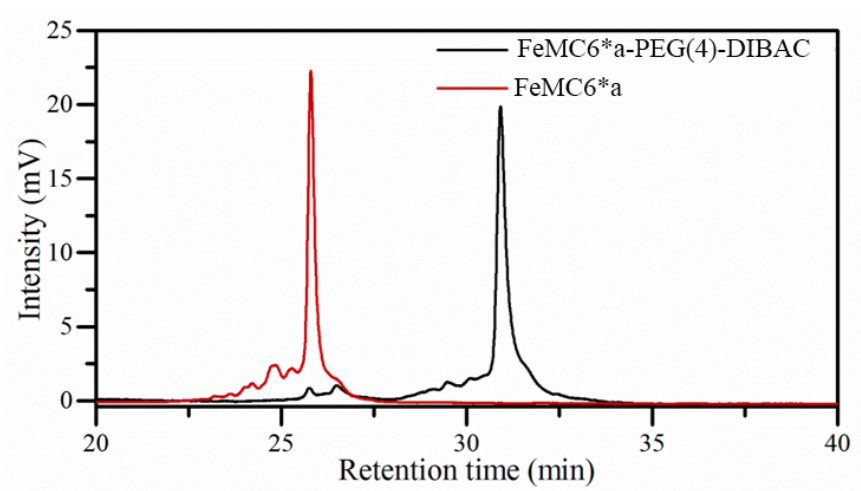
Figure 4.4. HPLC analysis of FeMC6*a–PEG(4)–DIBAC synthesis monitored at 0 min and overnight from the addition of click reagent (detected at λ=387 nm).

The UV–Vis profile of the product is consistent with FeMC6*a–PEG(4)–DIBAC, as the characteristic absorption bands of both iron–porphyrin (λ=387nm) and DIBAC (λ=310 nm) are present in the reaction product (Figure 4.5). The excess of DIBAC–PEG(4)–NHS was removed by three sequential precipitation cycles in methyl–*tert*–buthyl ether and redissolution in DMF. The product was finally resuspended in H_2O with 0.1% (*v/v*) TFA and lyophilized.
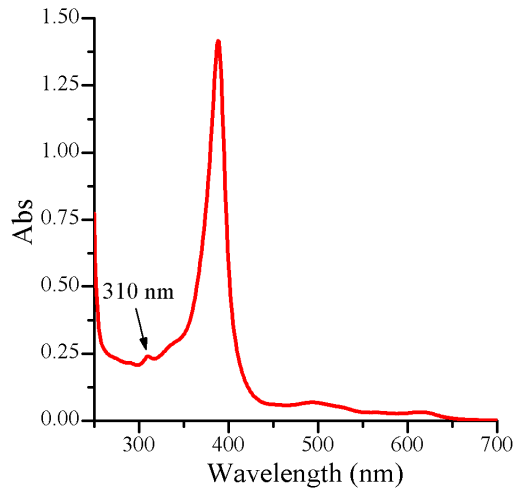
Figure 4.5. UV–Vis profile of FeMC6*a–PEG(4)–DIBAC.

4.2.3 Synthesis of N_3–AuNPs

Citrate–stabilized AuNPs were obtained following the Turkevich method [Turkevich, J. et al. (1951)].
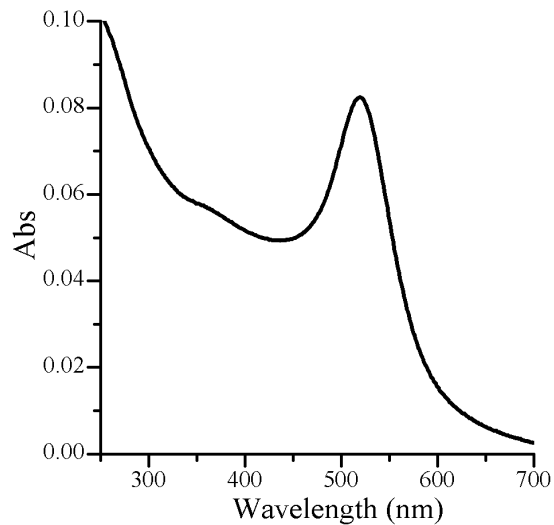
Figure 4.6. Characteristic SPRB of citrate–AuNPs.

The UV–Vis spectrum of the solution, after cooling, showed a characteristic SPRB maximum at 520 nm (Figure 4.6). As reported in the literature [Haiss, W. et al. (2007)], the ratio of the absorbance at the SPR band (A_{SPR}) to the absorbance at 450 nm (A_{450}) provides an indication of the AuNPs diameter. From the UV–Vis spectrum, the A_{SPR}/A_{450} ratio was calculated to be 1.63, thus suggesting the formation of AuNPs with a diameter of ca. 15 nm (See Table 4.2).

By ligand exchange reaction, a self–assembled monolayer (SAM) of thiols on AuNPs was grafted by adding a mixture of bifunctional linkers, namely lipoic acid and its derivative $LipN_3$ (in a 9:1 molar ratio, respectively) (Figure 4.7a). This allowed for obtaining azide–terminated AuNPs (N_3–AuNPs). The azide moiety on $LipN_3$ was used for enzyme conjugation via click chemistry [Kanaras, A. G. et al. (2002)] onto AuNPs, while the carboxylic groups of lipoic acid ensured the formation of negative charges on the surface, providing stability to the colloidal solution and avoiding AuNPs aggregation [Zhang, M. X. et al. (2010)].

Prior to ligand exchange reaction, the pH of citrate–stabilized AuNPs suspension was adjusted to 11 with a freshly prepared NaOH aqueous solution. Then, a 9:1 molar ratio mixture of lipoic and $lipN_3$ ligands was prepared in DMSO and added to the citrate stabilized AuNPs under stirring (0.4094 equivalents of ligands with respect to Au). Upon addition of the mixture, a shift in the SPRB of the gold nanoparticles, from 520 nm to 523 nm, was observed (Figure 4.7b, red line), confirming the effective ligand exchange reaction.
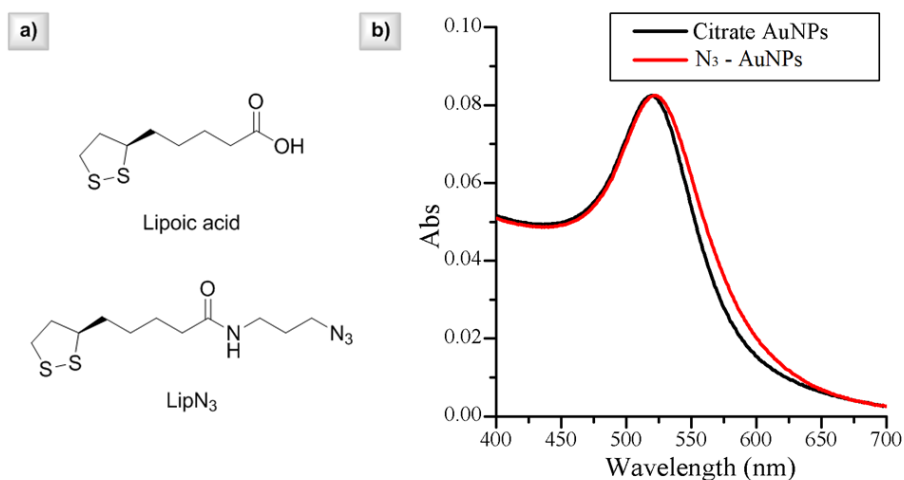
Figure 4.7.a) linkers structures b) UV–Vis spectra of citrate–stabilized AuNPs (black) and lipoic/lipoic azide (9:1) stabilized AuNPs (red).

The functionalized N_3–AuNPs were purified by centrifugation and resuspension in equal volume of fresh NaOH (pH=11).

Quantitation of the azide groups on N_3–AuNPs was carried out by UV–Vis spectroscopy, using DIBAC–PEG(4)–COOH as probe. Briefly, DIBAC-PEG(4)-COOH (86 µM) was added to the N_3–AuNPs suspension. After incubation, the residual amount of DIBAC-PEG(4)-COOH in soluzion was estimated by UV-Vis.
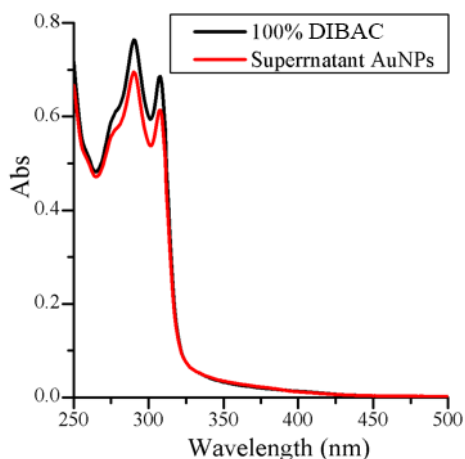
Figure 4.8. UV–Vis spectra of DIBAC in NaOH solution (black) and DIBAC in AuNPs supernatant (red).

The amount of DIBAC linked onto AuNPs surface was estimated to be 9.03 µM. From the concentration ratio of bound DIBAC and N_3–AuNPs, the number of azide groups exposed per AuNPs was estimated as 1580.

4.2.4 Synthesis of Lip@PEG(4)–FeMC6*a and its catalytic characterization

In order to assess whether the chemical modification of FeMC6*a with PEG(4)–DIBAC moiety and subsequent click reaction with $LipN_3$ influenced the catalytic performances of the enzyme, the SPAAC reaction with $LipN_3$ was carried out in solution (Figure 4.9).

The SPAAC reaction was performed in DMF under stirring, using 4 equivalents of $LipN_3$ with respect to modified enzyme. The reaction was followed through (Figure 4.10).

After synthesis and RP–HPLC purification, the catalytic activity of Lip@PEG(4)–FeMC6*a was investigated for oxidation of ABTS, using H_2O_2 as the oxidizing substrate.

Kinetic experiments were performed using fixed concentration of the enzyme (20nM) in 50 mM phosphate buffer (pH 6.5) 50% TFE (*v/v*), conditions in which FeMC6*a exhibits the highest catalytic performances [Caserta, G. et al. (2018)] (Figure 4.9). Fitting of the data points gave the catalytic parameters reported in Table 4.5.
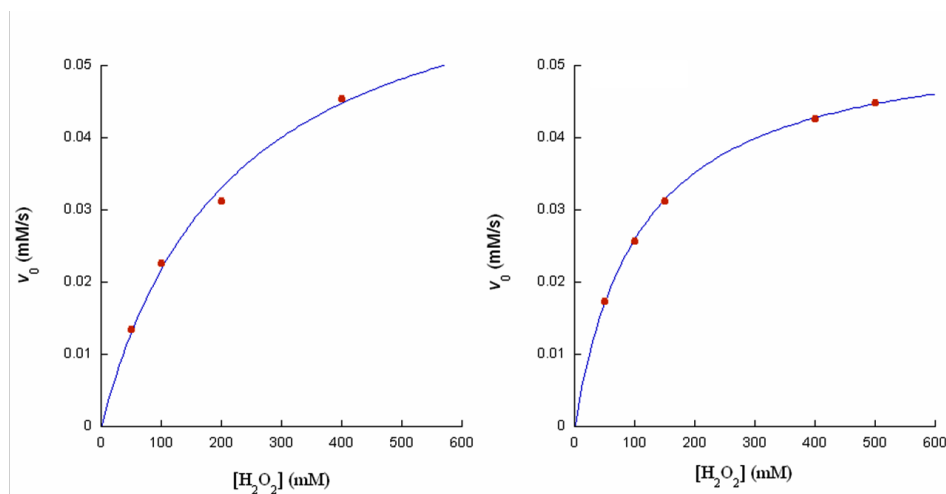
Figure 4.9. Kinetic studies for the oxidation of ABTS by (a) the free enzyme; (b) the site–specific modified enzyme. The graph shows the initial rates (v_0) (mM/s) of ABTS$^{\cdot+}$ formation at various concentration of H_2O_2.

Table 4.5. Catalytic parameters for FeMC6*a and FeMC6*a–PEG(4)@Lip.

	K_m [mM] H_2O_2	k_{cat} (s^{-1})	k_{cat}/K_m (mM^{-1} s^{-1})
FeMC6*a	$(1.1\pm0.2)\cdot10^2$	$(2.30\pm0.15)\cdot10^3$	22
FeMC6*a–PEG(4)@Lip	$(1.10\pm0.03)\cdot10^2$	$(2.70\pm0.02)\cdot10^3$	25

FeMC6*a and Lip@PEG(4)–FeMC6*a showed similar K_m and k_{cat} values, therefore suggesting that the chemical modification of the enzyme did not alter its catalytic performances.

4.2.5   **FeMC6*a@AuNPs synthesis**

In order to couple the enzyme to AuNPs, N_3–AuNPs were then allowed to react with FeMC6*a–PEG(4)–DIBAC. The SPAAC reaction was performed by adding a solution of FeMC6*a–PEG(4)–DIBAC in DMF to the N_3–AuNPs aqueous pH 11 suspension, under vigorous stirring until no further shifts in plasmon resonance band were observed. More specifically, 1500 equivalents of FeMC6*a–PEG(4)–DIBAC, with respect to AuNPs, were added. FeMC6*a@AuNPs were purified from the excess of free enzyme through cycles of centrifugation and resuspension. After each cycle, the supernatants containing the unbound enzyme were discarded and the pellet containing the conjugate was re–suspended in an equal volume of NaOH pH 11, in order to preserve stability of the colloidal solution.

The UV–Vis analysis of the mixture showed a 5 nm SPRB shift (Figure 4.10). Compared to N_3–AuNPs ($SPRB_{max}$=523 nm), the purified conjugate shows a maximum absorption of SPRB at 528 nm, which confirms the conjugation of FeMC6*a. Furthermore, the weak absorption band around 390 nm, consistent with heme absorption band (Figure 4.12, black line), provides a direct evidence of the successful FeMC6*a conjugation to AuNPs.
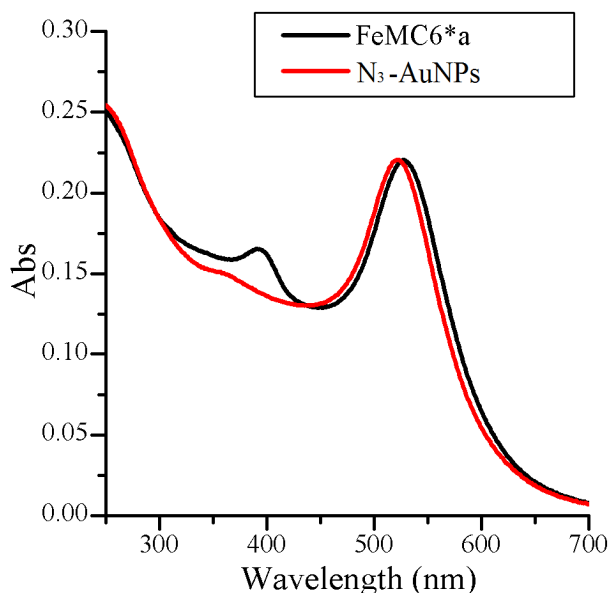
Figure 4.10. UV–Vis spectra of lipoic/lipN$_3$ (9:1) stabilized AuNPs (red) and FeMC6*a@AuNPs (black).

An excess of the enzyme can be adsorbed onto AuNPs surface through non–covalent interactions (ionic, hydrophobic, etc.), therefore FeMC6*a@AuNPs were finally washed with NaOH solution (pH=11) with 50 %(v/v) 2,2,2–trifluoroethanol (TFE) [Zambrano, G. et al. (2018)]. Finally, after centrifugation, the pellet was re–suspended in NaOH pH=11, yielding purified FeMC6*a@AuNPs.

4.2.6 Characterization of FeMC6*a@AuNPs conjugate

The morphology and size distribution of the nanoparticles were assessed by TEM analysis. Figure 4.11 shows TEM images with sharp high contrast due to AuNPs protein surrounding.
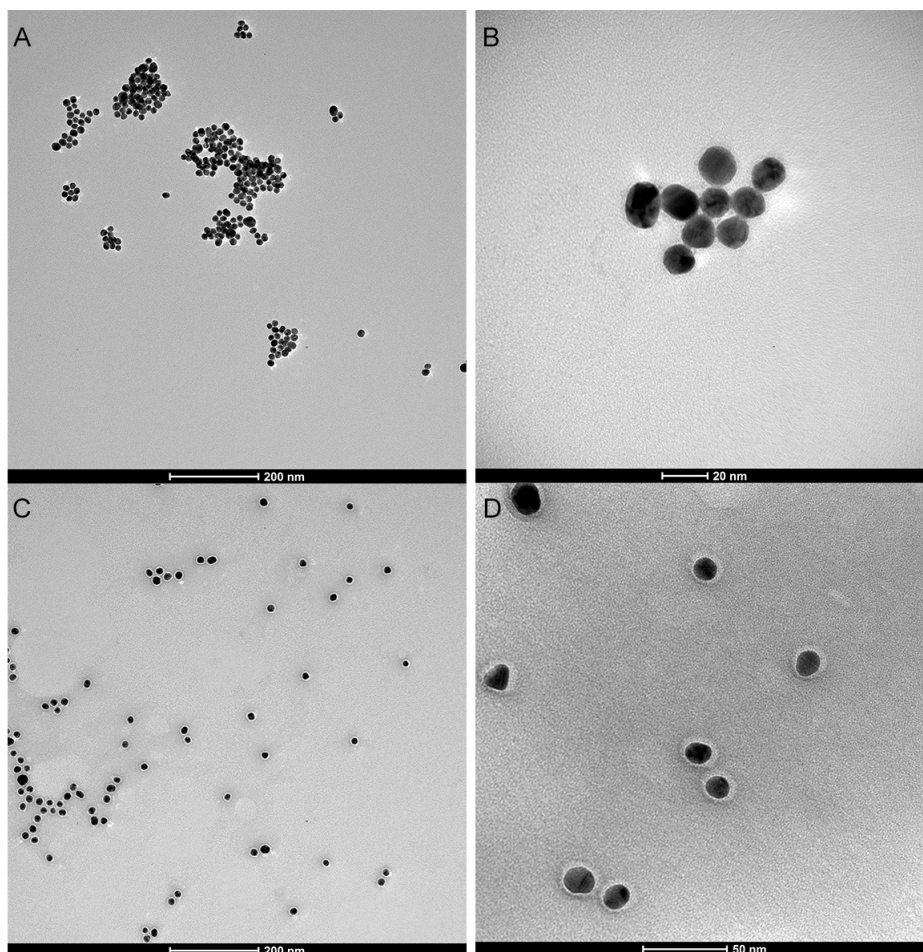
Figure 4.11. TEM images: (a–b) N$_3$–AuNPs; (c–d) FeMC6*a@AuNPs conjugate. The samples were stained with Uranyless® before observation.

The mean particle size and standard deviation were determined from nanoparticles statistic measurements using ImageJ software. The resulting citrate AuNPs had an average core diameter of 14.6±2.0 nm with a good monodispersity based on TEM analysis (Figure 4.12).
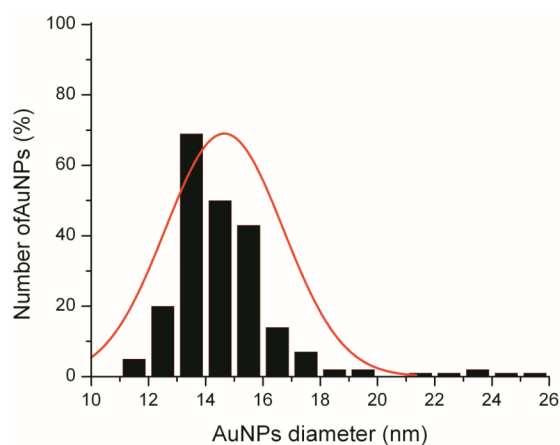
Figure 4.12. Histogram and gaussian fit (red line) of the experimentally measured AuNPs diameters based on TEM analysis.

Upon Uranyless[®] staining, a protein corona appeared around the gold core as a bright halo. The protein corona thickness was measured using ImageJ software, with an average thickness of 3.3±0.3 nm.
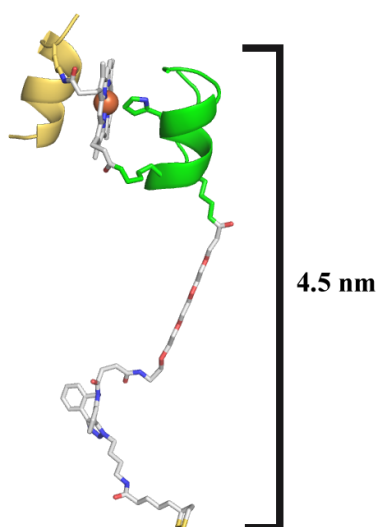
Figure 4.13. Model structure of Lip@PEG(4)–FeMC6*a

The protein corona thickness was rationalized by estimating the length of Lip@PEG(4)–FeMC6*a from its model structure. Figure 4.13 shows a 4.5 nm distance from the dithiolane moiety of Lip to FeMC6*a. Although no exact match between measured protein corona (3.3±0.3 nm) and Lip@PEG(4)–FeMC6*a length from model structure (4.5 nm) was found, the data suggest with good confidence that FeMC6*a arranges itself as a single layer over the AuNP surface, in contrast with what observed for MIMO@LA@AuNPs [Zambrano, G. et al. (2018)].

Quantitative determination of iron and gold content in the colloidal suspension was used to estimate experimentally the numer of FeMC6*a/AuNP. To this purpose, inductively coupled plasma–mass spectrometry (ICP–MS) analysis was carried out and the results obtained were used to determine the FeMC6*a/AuNP ratio. The concentrations of Au and Fe, obtained by ICP mass are show in Table 4.6.

Table 4.6. Concentration of Fe and Au calculated by ICP–MS.

	[Fe] (μM)	[Au] (μM)
N_3–AuNPs	/	539.68
FeMC6*a@AuNPs	0.91	373.95

As expected, in the N_3–AuNPs sample no relevant amounts of iron were detected. The total amount of Fe in the FeMC6*a@AuNPs sample was found to be 0.91 μM, corresponding to a 0.91 μM FeMC6*a concentration.

Given the average diameter of AuNPs and the concentration of gold and iron, the number of FeMC6*a per AuNP was calculated.

By considering r = 7.3 nm, as derived from TEM analysis, AuNPs concentration in FeMC6*a–AuNPs was assessed, using Equation 1 and Equation 2 by dividing

the gold atoms/volume unit (N_{Au}; measured by ICP–MS) for the number of gold atoms composing one AuNP (N^{Au}_{AuNP}). The concentration of AuNPs was estimated to be 3.60 nM.

$$N^{Au}_{AuNP} = \frac{4}{3}\pi r^3 \frac{\rho_{gold}}{AW_{gold}} A; \; (Equation \; 1)$$

$$[AuNPs] = \frac{N_{Au}}{N^{Au}_{AuNP}}; \; (Equation \; 2)$$

Therefore, the ratio between concentration of FeMC6*a and concentration of AuNPs gave the average number of bound FeMC6*a per AuNP (Equation 3), which was estimated to 253 (Table 4.7).

$$FeMC6*a/_{AuNP} = \frac{[FeMC6*a]}{[AuNPs]}; \; (Equation \; 3)$$

Table 4.7. Concentration of Fe and Au calculated by ICP–MS.

	[Fe] (µM)	[AuNPs] (nM)	FeMC6*a/AuNP
N$_3$–AuNPs	/	5.70	/
FeMC6*a@AuNPs	0.91	3.60	253

The maximum number (N_{max}) of FeMC6*a units that can be loaded onto AuNP were calculated from Equation 4 as reported by [Mattoussi, H. et al. (2000)]:

$$N_{max} = 0.65 \times \frac{R^3_{complex} - R^3_{AuNP}}{R^3_{protein}} \; (Equation \; 4)$$

where $R_{complex}$ is the AuNP–protein complex radius, R_{AuNP} (7.3 nm, as observed by TEM) is the gold nanoparticle radius including Lipoic-DIBAC-PEG(4) linker and Lys11 side chain (estimated as 3.6 nm from the model structure shown in

Figure 4.13), and $R_{protein}$ is the radius of the protein. The ratio is corrected by 0.65 as filling factor for hard sphere. $R_{complex}$ comprises the sum of R_{AuNP} and the diameter of the MIMO protein. Analogously as reported in [Zambrano, G. et al. (2018)], the radius of gyration (R_G) [Lobanov, M.Y. et al. (2008)] was used to calculate an average diameter of FeMC6*a (2 x R_G=1.8 nm), by taking into account all possible orientations. This calculation afforded an N_{max} of ≅670 FeMC6*a/AuNP. The experimental data (253 FeMC6*a/AuNP) are in good agreement with the calculated N_{max} of FeMC6*a that can be displayed on the AuNPs surface.

4.2.7 Conformational analysis of FeMC6*a@AuNPs

A conformational analysis was carried out to assess whether immobilization of FeMC6*a onto AuNPs affects its folding ability. CD spectra were collected at 25°C, from 260 to 195 nm, in 10 mM phosphate buffer (pH 6.5) 50% TFE (*v/v*), and mean residue ellipticities [θ] were reported as function of wavelength (Figure 4.14). CD spectrum of immobilized FeMC6*a confirms that helical structure is well preserved upon immobilization.
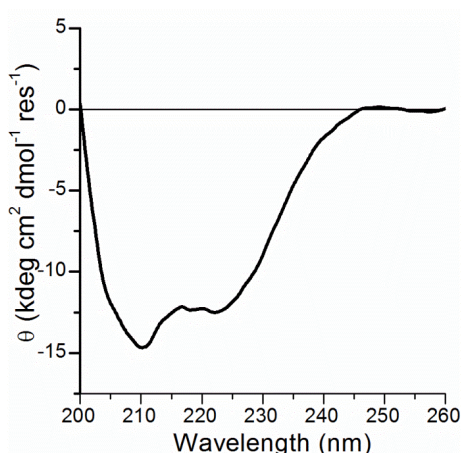
Figure 4.14. CD spectra of FeMC6*a@AuNPs.

4.2.8 **Catalytic characterization of FeMC6*a@AuNPs**

The activity of FeMC6*a@AuNPs conjugate was assayed for oxidation of ABTS, using H_2O_2 as the oxidizing substrate. To optimize the experimental condition for catalytic activity, the effects of 2,2,2–trifluoroehanol (TFE) concentration and pH on catalytic activity [Caserta, G. et al. (2018)] were firstly investigated using the following experimental conditions: 5 mM ABTS, 10 mM H_2O_2 at FeMC6*a concentration of 27.3 nM (based on ICP–MS measurments). Kinetic experiments at 50 %(*v/v*) TFE were performed in the pH range of 4.5 to 9.8 using 50 mM acetate, phosphate and carbonate buffer, respectively, recording the absorbance at 660 nm. Initial rates, determined by the slope of the progress curve at t=0, were plotted as function of pH. A bell–shaped curve was obtained reporting v_0 (mM/s) as function of pH and the maximum v_0 value is reached between pH 6 and 6.5 (Figure 4.15), similarly to freely diffusing FeMC6*a [Caserta, G. et al. (2018)].
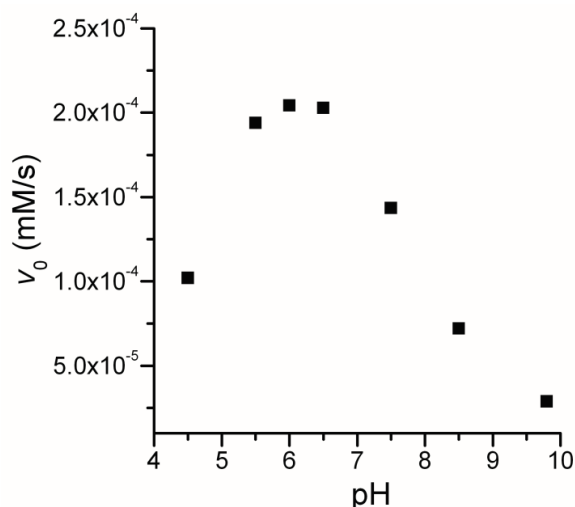
Figure 4.15. Initial rate of ABTS oxidation *vs* pH (pH range 4.5–9.8) for FeMC6*a@AuNPs.

TFE dependence of catalytic activity was explored at three different concentrations. Kinetic assays were performed in phosphate buffer 50 mM (pH=6) at 0%, 30%, 50%(v/v) TFE.

Table 4.8. Initial rate of ABTS Oxidation as function of %(v/v) TFE.

TFE	FeMC6*a@AuNPs
%(v/v)	v_0 (mM/s)
50	$2.2 \cdot 10^{-4}$
30	$6.2 \cdot 10^{-5}$
0	$1.0 \cdot 10^{-5}$

Experimental data confirm that the best performances for FeMC6*a@AuNPs are achieved at 50%(v/v) TFE, analogously to what observed in the freely diffusing state (Table 4.8).

Lastly, catalytic parameters such as k_{cat} and K_m for H_2O_2 and ABTS were determined. Catalytic assays were performed at fixed concentration of enzyme, in optimized experimental conditions (50mM phosphate buffer pH 6.5 and 50 %(v/v) TFE). Initial rates of reaction were determined by kinetic curves acquired at various concentrations of H_2O_2 in the 0–500 mM range, and ABTS in the 0–10 mM range. Catalytic parameters were determined by fitting v_0 values (Figure 4.16) with a two–substrates Michaelis–Menten equation (Section 4.4.12, Equation 4.6) using the concentration of FeMC6*a calculated by ICP–MS analysis (27.3 nM final concentration in the assay solution).
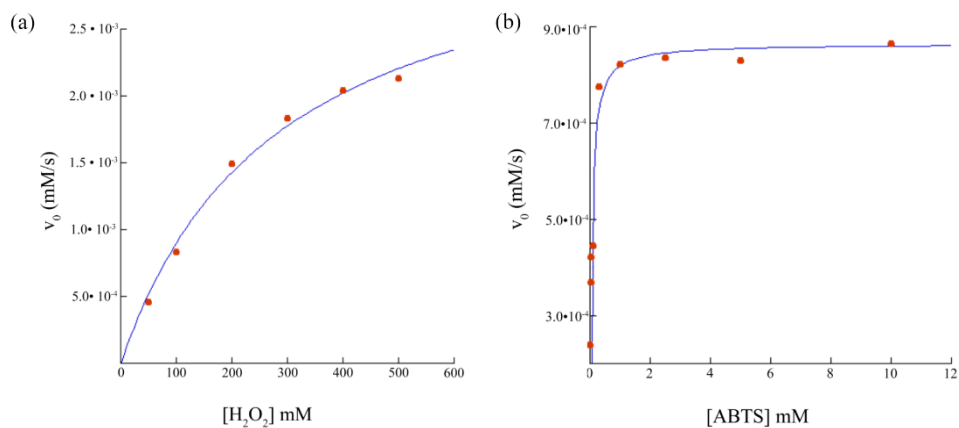
Figure 4.16. Kinetic studies for the oxidation of ABTS by FeMC6*a@AuNPs conjugate. The graph shows the initial rates (v_0) (mM/s) of ABTS$^{.+}$ formation at various concentration of ABTS (left) and H_2O_2 (right).

Table 4.9 reports the k_{cat} (turnover frequency) and K_m kinetic constants for the ABTS oxidation, for both the immobilized and freely diffusing enzyme modified by the linker.

Table 4.9. Catalytic parameters for FeMC6*a freely diffusing and immobilized onto AuNPs.

	K_m^{H2O2} (mM) 10^2	K_m^{ABTS} (mM) 10^{-2}	k_{cat} (s^{-1}) 10^{-2}	k_{cat}/K_m^{ABTS} ($mM^{-1}s^{-1}$) 10^{-3}	k_{cat}/K_m^{H2O2} ($mM^{-1}s^{-1}$)
FeMC6*a	9±1	4.4±0.5	58±3	64±8	13±2
FeMC6*a @AuNPs	0.193± 0.005	2.16±0.04	1.10±0.03	0.570± 0.001	0.509±0.003

Analysis of the data reveals a decrease in the catalytic performances of FeMC6*a upon immobilization. In particular, a decrease k_{cat} value along with an increase in the K_m^{ABTS} values was observed when comparing the suspension of

FeMC6*a@AuNPs to the freely diffusing enzyme.

The catalytic performances obtained for FeMC6*a@AuNPs were compared to those obtained for a previous AuNPs nano-bioconjugate, reported by [Zambrano, G. et al. (2018)]. The two studies used different analogues belonging to mimochrome family, and, as consequence, the performances of the two nano-bioconjugates were compared based on the ratio between catalytic efficiencies in freely-diffusing state and after immobilization.

Table 4.9. Comparison of the catalytic performances for ABTS oxidation for FeMC6*a and MIMO freely diffusing and immobilized onto AuNPs. [1] [Zambrano, G. et al. (2018)]

	k_{cat}/ K_m^{ABTS} $(mM^{-1} s^{-1})$ freely diffusing	k_{cat}/ K_m^{ABTS} $(mM^{-1} s^{-1})$ immobilized	Ratio (freely diffusing/ immobilized)
FeMC6*a	$64\pm8\cdot10^3$	570 ± 1	112
MIMO[1]	3473 ± 814	11.5	302

Although, in both cases the catalytic performances in ABTS oxidation are decreased upon immobilization, the comparison confirms the positive impact of the new immobilization strategy. In detail, the extent of decrease in performances in the bio-orthogonal conjugation protocol is less severe, being 112-fold compared to the 302-fold decrease in performances when the direct chemisorption approach is used. This comparison might suggest that distance from the AuNP surface is crucial for the preservation of the catalytic performances, both for accessibility of substrates and for higher conformational freedom of the enzyme, upon immobilization, however further experiments are required to ascertain this behavior.

4.3 **Conclusions and future perspectives**

The wide variety of applications of immobilized enzymes has led to the development of innovative strategies for biocatalysts loading onto solid matrices. In most cases, these processes cause loss of enzymatic activity resulting in decrease in catalytic performances. In this context, the current work has been focused on the functional and kinetic characterization of novel AuNPs–based nano–bioconjugates, resulting from immobilization of an artificial heme peroxidase onto AuNPs surface via strain promoted click chemistry approach.

This work successfully demonstrated that the site–specific modification of mimochromes can be carried out. The presence of the properly designed Lys11 (TD) allows the derivatization of FeMC6*a with linkers. The catalytic investigation on Lip@PEG(4)–FeMC6*a confirms a successful derivatization without loss of catalytic performances. Moreover, the TEM data of FeMC6*a@AuNPs confirms that the stability and dispersity of the AuNPs suspension was not altered by the FeMC6*a coating layer.

FeMC6*a@AuNPs was assayed towards oxidation of ABTS. Although it exhibits worse performances compared to the freely diffusing forms, a significant catalytic activity was still detected.

Two main factors may affect the catalytic performances of AuNPs–embedded enzyme: i) influence of the bioconjugate sizes on the substrates diffusion kinetics and ii) enzyme accumulation and overcrowding of the enzyme onto AuNPs. More specifically, the activity of the catalyst can be affected by the poor accessibility of substrates and/or by inhibition of enzyme during catalysis for steric hindrance. Further efforts will be devoted to fully understand and overcome the issues related with the decrease of catalytic performances. However, in comparison with previous mimochrome@AuNPs conjugates, with the proposed method a better preservation of the catalytic performances was

obtained, suggesting that distance between the enzyme and the AuNP surface is crucial for the catalytic activity. The overall results represent an improvement in the obtainment of catalytically active mimochrome@AuNPs nano-bioconjugates and pave the way to future applications in diagnostic and biosensing.

4.4 **Materials and methods**

All solvents, used in the synthesis and purification (water, acetonitrile, TFA, DMF, TFE, acetic acid and ether), were anhydrous and HPLC grade, and were supplied by Romil (Cambridge, UK). Solvents with a higher degree of purity were used in the preparation of solutions for UV–Vis investigations (Ups grade). Trisodium citrate dihydrate as well as $HAuCl_4$ solution (30% (w/w)), ABTS and lipoic acid were purchased from Sigma Aldrich (Taufkirchen, Germany). Phosphate salts (monobasic and dibasic) for buffers preparation, Uranyless® staining solution and H_2O_2 (30%, (v/v)) were provided by Fluka. All buffer solutions were made by using water with a HPLC purity grade (Romil); N,N–diisopropyletylamine was obtained from Applied Biosystem. HATU was aquired from NovaBiochem, and the click reagent DIBAC–PEG(4)–NHS from Jena Bioscience. All reagents were used without further purification.

HPLC and LC–MS analysis were performed using a Shimadzu LC–10ADvp system equipped with an SPDM10Avp diode–array detector. ESI–MS spectra were recorded on a Shimadzu LC–MS–2010EV system with ESI interface and Shimadzu LC–MS solution Workstation software for data processing. Preliminary purifications and desalting are performed by flash chromatography (ISOLERA ISO–1SW Biotage with diode array detector). Purifications were accomplished by preparative RP-HPLC with Shimadzu LC-8A connected to a SPD–20A Shimadzu UV-Vis spectrophotometric detector.

ESI–IT/TOF spectra were recorded on a Shimadzu LCMS–IT–TOF system with ESI interface and Shimadzu LC–MS solution Workstation software for the data. All analyses were performed with a Vydac C18 column (2.1 mm x 100 mm;5μm), eluted with an H_2O 0.05 % trifluoroacetic acid, TFA, (eluent A) and CH_3CN 0.05 % TFA (eluent B) linear gradient, from 10 to 95% (solvent B), over

37 minutes, at 0.2 mL min^{-1} flow rate. The optimized MS parameters were selected as followed: CDL (curved desolvation line) temperature 250°C; the block temperature 250 °C; the probe temperature 250 °C; detectorgain 1.6kV; probe voltage +4.5kV; CDL voltage –15V. Nitrogen served as nebulizer gas (flow rate: 1.5 L min^{-1}).

The UV–Vis analysis and kinetic experiments were recorded with a Cary 60 spectrophotometer (Varian, Palo Alto, CA, USA), equipped with a thermostatic cell compartment, using quartz cuvettes with 0.1 cm, 0.01 cm and 1 cm path lengths. Wavelength scans were performed at 25°C from 200 to 800 nm, with a 600 nm min^{-1} scan speed. All data was blank subtracted.

Circular Dichroism measurements were performed using a J–815 spectropolarimeter equipped with a thermostated cell holder (JASCO, Easton, MD, USA). CD spectra were collected using quartz cuvettes with 1 cm path lengths. at 25°C, from 260 to 200 nm with a 20 nm^{-1} scan speed. A quartz cell of 1 cm path length was used in all measurements. Nanoparticles and their derivatives were purified by centrifugation cycles through Sigma Refrigerated Centrifuge 2K15 with 12148–H or 12141–H rotors.

Electron microscopy characterization. Transmission electron microscopy (TEM) images have been obtained in bright field mode using a TEM TECNAI G2 20ST. Copper grid with carbon film (Agar Scientific Ltd., product S160, 200 mesh) were used.

Iron and gold content of bioconjugates was quantified by ICP–MS analysis, using Aurora Bruker M90 instrumentation (Bremen, Germany). Aqua regia digestion procedure (90°C, 45 min.) was adopted for organic component and gold degradation.

All the molecular graphics pictures were generated with PyMOL software (DeLano Scientific Ltd), and ChemDraw Ultra 12. Data analysis was made with Origin Pro 9.0 software (Origin Lab Corporation, Northampton, MA, USA),

ImageJ software (National Institutes of Health, available free of charge at Web site rsb.info.nih.gov/ij/) and Kaleidagraph software (version 4.1.1, Synergy Software, Reading, PA, USA).

4.4.1 Synthesis of N–(3–azidopropyl)–5–(1,2–dithiolan–3–yl)–pentanamide

The synthetic strategy consisted in two steps:

    1) Synthesis of 3–azidopropanamine

    2) Coupling reaction between 3–azidopropanamine and α–lipoic acid.

3–azidopropanamine was synthetized starting from 1,3–diazidopropane by hemi reduction with triphenylphosphine (Staudinger reduction), following the protocol developed by [Srinivasan, R. et al. (2009)]. The reaction was carried out in biphasic media in order to obtain the desired product, avoiding double reduction byproduct (Figure 4.17).
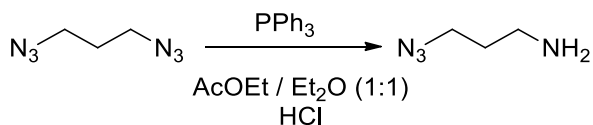
Figure 4.17. Staudinger reduction in biphasic media.

The procedure consisted into the addition of small portions of PPh$_3$ to 1,3–diazidopropane in a biphasic mixture made of ethyl acetate/diethyl ether 1:1 (*v/v*) and 5%(*v/v*) aqueous hydrochloric acid. In detail, 1,3–diazidopropane (1.5 mmol) was dissolved in Et$_2$O:EtOAc (1:1) (2mL) and the aqueous phase (5% HCl) (1.6 mL) was added under stirring. Then, small portions of triphenylphosphine (1 mmol) were added over 1 h. The reaction was kept for 1 h at 0°C and then left while stirring for 24 h at room temperature. The reaction was monitored via TLC using cyclohexane as eluent. Afterwards, the reaction mixture was transferred to a separatory funnel, the organic layer was discarded

and the aqueous layer was extracted twice with DCM (2 mL). The resulting aqueous phase was carefully basified with 6 M NaOH and then extracted with DCM (3 x 2 mL). The organic fractions were pulled together and dried over Na_2SO_4. Finally, the excess of solvent was evaporated to dryness, to yield pure 3– azidopropanamine (quantitative yield).

Coupling between 3–azidopropanamine and α–lipoic acid was achieved by using HATU as activating agent (Figure 4.18). A coupling reaction was carried out by condensing carboxylic group of α–lipoic acid and the amine group of 3–azidopropanamine. The first step of this condensation reaction is the activation of the carboxyl moiety, since the carboxyl acid is not sufficiently reactive and need to be transformed in an active ester. The reaction was performed using HATU (1–[Bis(dimethylamino)methylene]–1H–1,2,3–triazole[4,5–b]pyridinium 3–oxid hexafluorophosphate) as activating agent. The reaction was performed in basic conditions as HATU reacts with the carboxylate species.
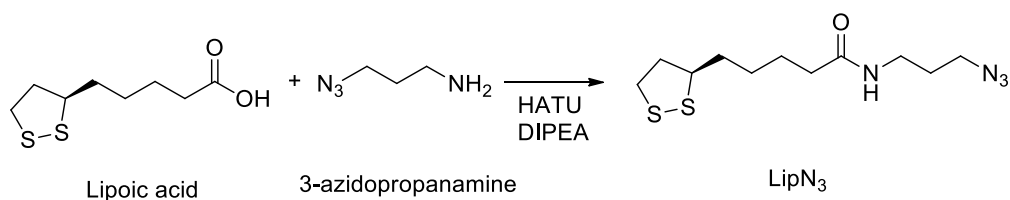
Figure 4.18. N–(3–azidopropyl)–5–(1,2–dithiolan–3–yl)pentanamide formation via coupling with HATU reaction.

The coupling reaction was carried out by dissolving 4 mg of 3–azidopropanamine (1 eq) and 4.2 mg of α– lipoic acid (2 eq) in 1.5 mL of DMF. The solution was basified to pH ≈ 9 with DIPEA and then 8.3 mg of HATU (1.1 eq) were added. Reaction mixture was left under stirring for 1 h and then RP–HPLC–MS analysis was performed to identify the products. The mobile phase

was made up of H_2O 0.1%(*v/v*) trifluoroacetic acid (TFA) (solvent A) and CH$_3$CN 0.1%(*v/v*) TFA (solvent B) linear gradient, from 5%(*v/v*) to 95%(*v/v*) (solvent B) over 56 min, at a 1 mL·min^{-1} flowrate. A Vydac C8 column (4.6 mm 150 mm; 5 µm), was used in the LC–MS analysis. The mass spectrum corresponds to the mass of (3–azidopropyl)–5–(1,2–dithiolan–3–yl)pentanamide as it showed the presence of main peak at *m/z* 289.05 (Figure 4.19). This value is in agreement with the expected mass value (theoretical mass: 288 Da). The reaction mixture was purified by preparative RP–HPLC on a C8 column. The collected fractions were analyzed through analytical RP–HPLC, to confirm the purity of the product. The desired product exhibits absorption at λ=333 nm, typical of disulfide containing compounds (Figure 4.20).
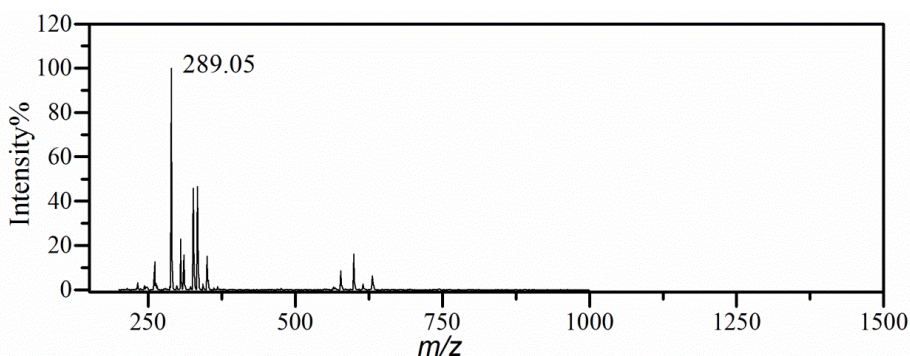
Figure 4.19. ESI–MS spectrum of LipN$_3$.
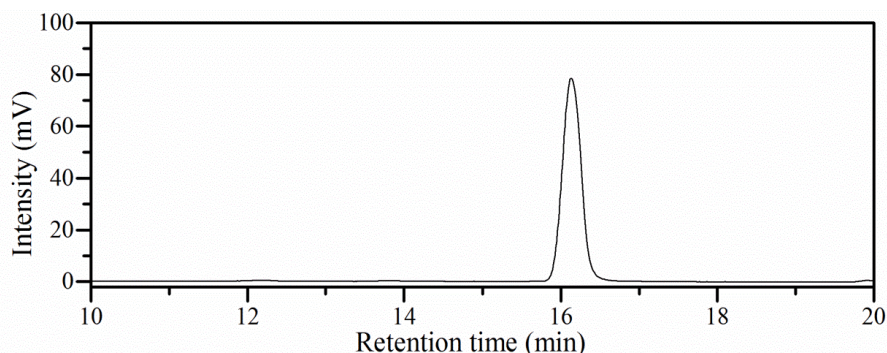
Figure 4.20. HPLC analysis of pure LipN$_3$ (detected at 333 nm).

4.4.2   Synthesis of FeMC6*a–PEG(4)–DIBAC

The coupling reaction between FeMC6*a and DIBAC–PEG(4)–NHS was performed under stirring in anhydrous DMF as solvent, using 3 equivalents of DIBAC–PEG(4)–NHS ($2.77 \cdot 10^{-6}$ mol, 20µl of a stock solution 100 mg/ml in DMF) with respect to FeMC6*a ($9.25 \cdot 10^{-7}$ mol, 3.20 mg dissolved in 320µl in DMF) in presence of DIPEA (11eq., 1.77 µl, pH$\approx$ 9). The reaction was left overnight at room temperature and was monitored by RP–HPLC using a C18 column (GRACE Vydac 218TP C18 5µ) eluted with H$_2$O 0.1% TFA (*v/v*) (solvent A) and acetonitrile 0.1% TFA (solvent B) in a linear gradient from 10 %(*v/v*) to 50%(*v/v*) of B in 30 min, with a flow rate of 1.0 mL·min^{-1}.

The RP–HPLC chromatogram confirmed the formation of the desired product, through retention time shift. The excess of unreacted DIBAC–PEG(4)–NHS was removed by three cycle of precipitation with methyl–tert–buthyl ether (MTBE). For each cycle, the reaction mixture (323µl) was slowly added to 1.5 mL of MTBE solution, that was kept at 0°C for 10 minutes. The mixture was then centrifuged at 4000 rpm, for 3 min. MTBE was removed and the procedure was repeated two more times, finally residual MTBE was removed by gentle N$_2$ flow. RP–HPLC analysis of the product confirms the purity of the product.

4.4.3 Synthesis of FeMC6*a–PEG(4)@Lip

Click reaction was performed between free FeMC6*a–PEG(4)–DIBAC and LipN$_3$ in DMF using 2.5 eq of LipN$_3$ (300µl of a stock solution 4.6 mM in DMSO) respect to FeMC6*a–PEG(4)–DIBAC.
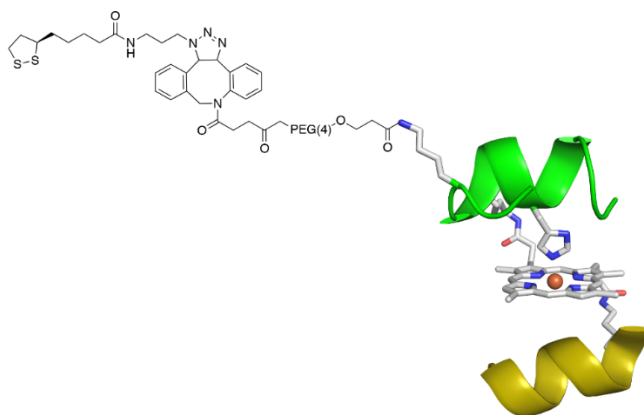
Figure 4.21. Molecular structure of Lip@PEG(4)–FeMC6*a.

The reaction was followed through RP–HPLC. RP–HPLC and mass analysis confirmed the formation of the desired product Lip@PEG(4)–FeMC6*a (Figure 4.21) (experimental *m/z* [M+3H$^+$]/3: 1438.6, [M+4H$^+$]/4: 1079.2 , [M+5H$^+$]/5: 863.6 were consistent with theoretical average mass (4313.7). (Figure 4.22)
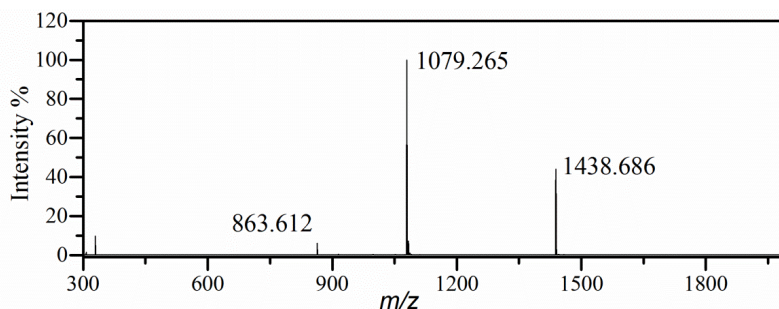
Figure 4.22. Mass spectrum of Lip@PEG(4)–FeMC6*a.

FeMC6*a–PEG(4)@Lip was purified by preparative RP–HPLC using using a Vydac C18 column (250mm x1cm) eluted from 0%(*v/v*) to 50%(*v/v*) over 50 minutes with a flow rate of 4.7 mL/min. A RP–HPLC analysis of the collected fractions confirmed the purity of the product.

4.4.4   Catalytic assay of site specific modified enzyme

All catalytic assays were performed at room temperature and under magnetic stirring, using quartz cuvettes with 1 cm path lengths. The experiments were followed using a Varian Cary 60 spectrophotometer, and ABTS as substrate. The change in absorbance of the ABTS$^{\bullet+}$ cation radical was followed at 660 nm (ε_{660} = 1.40·10^4 M^{-1} cm^{-1}). All reagents concentration was pre–determined spectrophotometrically by Lambert–Beer equation; using molar extinction coefficients at the maximum absorption wavelength (FeMC6*a, ε_{387} = 117000 M^{-1} cm^{-1}in 0.1% TFA) (ABTS, ε_{340} = 36600 M^{-1} cm^{-1}) (H$_2$O$_2$, ε_{240}= 39.4 M^{-1} cm^{-1}). A known volume of oxidant (H$_2$O$_2$) was added to the mixture while stirring. The acquisitions were carried out in the first 10 minutes of reaction. All the reactions were carried out using 5mM ABTS in phosphate buffer (50 mM, pH 6.5), in the presence of 50%(*v/v*) TFE. Initial rates were calculated by varying concentration of H$_2$O$_2$in the 0–500 mM range, and converted from Abs$_{660}$/min to mM/s through the ε value of ABTS$^{\bullet+}$ (14400 M^{-1}cm^{-1}). The experimental data were fitted through single–substrate Michaelis–Menten (**EQUATION 4.1**) and K$_m$ values for H$_2$O$_2$was calculated.

$$V = \frac{V_{max}[S]}{K_m + [S]} \qquad (\textbf{EQUATION 4.1})$$

This equation was inserted in Kaleidagraph software in the form of **EQUATION 4.2**

$$y = \frac{m_1 m_0}{m_1 + m_0}$$ (**EQUATION 4.2**)

4.4.5 Synthesis and functionalization of AuNPs

Citrate–stabilized gold nanoparticles (AuNPs) were prepared by Turkevich method. An aqueous solution of $HAuCl_4$ (1 mM, 25.5 mL) was brought to boil, and then kept at reflux under stirring for 10 min. Once the gold solution was vigorously refluxing, an aqueous solution of pre–heated sodium citrate (39 mM, 2.54 mL) was added quickly. The solution remained clear for about 10s and then the color of the solution turned ruby–red, indicating the formation of gold nanoparticles. The suspension was allowed to heat for additional 30 min with vigorous stirring. The suspension was then allowed to cool to room temperature. And characterized by UV–Vis spectroscopy. The UV–Vis spectra of the initial solution were recorded at 25°C using quartz cuvettes with a path length of 0.1 cm. Wavelength scans were performed from 800 to 200 nm, with a 600 nm min^{-1} scan speed. The UV–Vis spectra showed a sharp and characteristic plasmon absorption maximum around 520 nm. The functionalized AuNPs were stored in the dark at 4°C until further use.

4.4.5   Synthesis of N_3–AuNPs

The synthesis of N_3–AuNPs was carried out following a slightly modified method reported in [Zambrano, G. et al. (2018)]. For the ligand exchange reaction, 0.4094 equivalents of ligands with respect to Au were added to the AuNPs solution. The ligand mixture was prepared in a 9:1 molar ratio of α–lipoic acid: $LipN_3$ in DMSO. To 40 mL of AuNPs suspension (1 mM Au, assuming that all tetrachloroauric acid is converted to AuNPs), $1.64 \cdot 10^{-5}$ moles of ligands ($1.48 \cdot 10^{-5}$ mol of α–lipoic acid and $1.64 \cdot 10^{-6}$ mol of $LipN_3$) dissolved in 5.8 mL of DMSO were added. The concentration of ligands in the stock

solution was measured individually prior mixing using ε_{322}=124.36 M^{-1} s^{-1}. The progress of reaction was ascertained by UV–Vis and after 3h from ligands addition. After 3h, the reaction mixture was centrifuged and resuspended in an equal volume of NaOH pH 11, yielding purified N_3–AuNPs. The number of azide moieties displayed onto the AuNPs surface was estimated using DIBAC-PEG(4)-COOH as probe. Briefly, to a suspension of N_3–AuNPs at $5.70 \cdot 10^{-9}$ M concentration estimated from inductively coupled plasma mass spectrometry (ICP–MS) (See paragraph 4.2.2.6) in NaOH pH=11, DIBAC–PEG(4)–COOH (final concentration 86 μM) was added, and the mixture was incubated for 3 hours. Then, the solution was centrifuged at 10,000 rpm for 10 min at 4 °C, and the supernatant analyzed by UV–Vis spectroscopy. The amount of DIBAC–PEG(4)–COOH immobilized onto the AuNPs was determined by subtracting the unbound DIBAC–PEG(4)–COOH present in the supernatant from the total amount of reagent used, using as reference a DIBAC–PEG(4)–COOH standard solution (86 μM) (Figure 4.8).

4.4.6   Synthesis of FeMC6*a@AuNPs nanobioconjugate

Conjugation of FeMC6*a to AuNPs was achieved by SPAAC reaction. To 5 mL of this stock solution (AuNPs concentration $\cong$5.27 nM), 191μg of FeMC6*a– DIBAC, ($4.74 \cdot 10^{-4}$ mol) were added. The solution was incubated for 3h at room temperature in the dark, and the progress of the reaction was followed by UV– Vis analysis, evaluating the shift in the SPRB. UV–Vis spectra were recorded at 25°C using quartz cuvettes with a path length of 0.1 cm. Wavelength scans were performed from 200 to 800 nm, with a 600 nm min^{-1}scan speed. The UV–Vis spectra showed a sharp and characteristic plasmon absorption maximum at 530 nm, with a SPRB shift of 7 nm confirmed that conjugation occurred. To remove the excess of catalyst, the solution was centrifuged at 7500 rpm for 40 min at 10

°C. The supernatant was discarded and the remaining pellet was re–dispersed in a NaOH solution (pH 11). For each centrifugation cycle, , catalytic activity of the supernatant was tested by UV–Vis spectroscopy (from the 5th centrifugation cycle) to evaluate the residual amount of enzyme. Catalytic activity was assayed in a 50 mM phosphate buffer pH 6.5, 50% TFE (*v/v*), using a 5 mM ABTS and 10 mM H_2O_2. The kinetic curves were recorded under stirring (25°C) at λ=660 nm for 10min in a quartz cell with a 1 cm optical path length.

4.4.7 Trasmission electron microscopy analysis

The samples for TEM analysis were prepared by loading 5 µL drop for 60seconds of Citrate AuNPs, N_3–AuNPs, or FeMC6*a–AuNPs solutions onto carbon–coated copper grid (200 mesh) using cold loading station. Protein shell of FeMC6*a–AuNPs conjugates was visualized upon negative staining with Uranyless® solution. The samples were washed using H_2O Ups (35µl drop, 3 times,10s) and stained using Uranyless solution (35µl drop, 3 times, 10s). Last wash was performed with H_2O (35µl drop, 10s) and letting grids to air–dry at room temperature overnight. At least 150 independent measurements were taken at different locations of the TEM grid. By the experimental data the value of the mean radius of the AuNPs was obtained.

4.4.8 Circular dichroism of FeMC6*a@AuNPs

The samples for CD analysis were prepared by diluting FeMC6*a@AuNPs suspension 1:3 with phosphate buffer pH 6.5 50mM 50%(*v/v*) TFE and using quartz cuvettes with 1 cm path lengths. Mean residue ellipticities [θ] were calculated using the equation:

$$[\theta] = \frac{\theta_{obs}}{10 \cdot 1 \cdot C \cdot n}$$
(**EQUATION 4.3**)

in which θ_{obs} is the ellipticity measured in millidegrees, l is the path length of the cell in centimeters, C is the concentration in moles per liter, and n is the number of residues in the enzyme (23 residues).

4.4.9   Catalytic assays of FeMC6*a@AuNPs conjugate

All catalytic assays were performed at room temperature under magnetic stirring, using quartz cuvettes with 1 cm path lengths and using enzyme concentration 27.3 nM. All the catalytic experiments were followed using a Varian Cary 60 spectrophotometer, by using ABTS as substrate. The change in absorbance of the ABTS$^{\bullet+}$ cation radical was followed at 660 nm (ε_{660} = 1.44·10^4 M^{-1} cm^{-1}). Substrate and hydrogen peroxide stock solutions were freshly prepared, and their initial concentration was determined by UV–Vis spectroscopy (ABTS, ε_{340} = 36600 M^{-1} cm^{-1}) (H$_2$O$_2$, ε_{240}= 39.4 M^{-1} cm^{-1}). A known volume of oxidant (H$_2$O$_2$) was added to the mixture under stirring. The acquisitions were carried out in the first 10 minutes of reaction. Optimal experimental conditions were determined at 5mM ABTS, 10 mM H$_2$O$_2$ by varying TFE percentage (0%, 30%, 50% (v/v)) in phosphate buffer 50 mM pH 6.5, or by varing pH: 4.5, 5.5 (acetate buffer), 6.5, 6, 7.5, 8.5 (phosphate buffer), 9.8 (carbonate buffer) at 50% (v/v) TFE. Kinetic parameters were determined by varying H$_2$O$_2$ concentration at fixed ABTS concentrations, and viceversa. All the reactions were carried out in phosphate buffer (50 mM, pH 6.5), in the presence of 50% TFE (v/v). Initial rates were calculated by varying concentration of H$_2$O$_2$ in the 0–500 mM range, and ABTS in the 0–10 mM range. Initial rates were converted from Abs$_{660}$/min to mM/s through the ε_{660} value of ABTS$^{\bullet+}$(14400 M^{-1}cm^{-1}). The experimental data were first fitted through single–substrate Michaelis–Menten (**EQUATION 4.4**):

$$V = \frac{V_{max}[S]}{K_m + [S]}$$

(**EQUATION4.4**)

This equation was inserted in Kaleidagraph software in the form:

$$y = \frac{m_1 m_0}{m_1 + m_0}$$

(**EQUATION 4.5**)

In this first step K_m values for H_2O_2 and ABTS were calculated. The two set ofdata were then fitted using a two–substrates Michaelis–Menten equation:

$$y = \frac{[E]_0}{\frac{1}{k_{cat}} + \frac{K_{m(a)}}{k_{cat}[A]} + \frac{K_{m(b)}}{k_{cat}[B]}}$$

(**EQUATION 4.6**)

Where: $[E]_0$ is the enzyme concentration, which is supposed to be constant and not inactivated at the initial time(t_0); $k_{cat}$is the catalytic constant and denotes the maximum number of enzymatic reactions catalyzed per second; [A] and [B] represent the H_2O_2 and ABTS concentrations, respectively; $K_m(a)$ and $K_m(b)$ are the Michaelis–Menten constants for H_2O_2 and ABTS, respectively; the Michaelis–Menten constant is the substrate concentration at which reaction rate is half of V_{max} and representsthe enzyme apparent affinity for the substrate. The analysis of the experimental kinetic data by Michaelis–Menten fitting provides the following catalytic parameters:k_{cat}, K_m for H_2O_2 and ABTS,

from which it's possible to calculate k_{cat}/K_m that is the measure of the catalytic efficiency for both H_2O_2 and ABTS.

At fixed concentration of [A] (H_2O_2 in the experiment), previous equation becomes:

$$y = \frac{[E]_0 \cdot k_{cat}}{K_A + \frac{K_{m(b)}}{k_{cat}[B]}} ; \quad K_A = 1 + \frac{K_{m(a)}}{[A]}$$

(**EQUATION 4.7; 4.8**)

whereas at a fixed concentration of [B] (ABTS in the experiment) two–substrates Michaelis–Menten equation becomes:

$$y = \frac{[E]_0 \cdot k_{cat}}{K_B + \dfrac{K_{m(a)}}{k_{cat}[A]}} \; ; \; K_B = 1 + \frac{K_{m(b)}}{[B]}$$

(**EQUATION 4.9;**

4.10)

For each set of data, **EQUATION 4.11** on Kaleidagraph can be used:

$$y = \frac{m_0[E]_0}{m_4 m_0 + m_5}$$

(**EQUATION 4.11**)

Where:

$$m_0 = [S]_0 \; ; \quad m_4 = \frac{1 + \dfrac{K_{m(a)}}{[A]}}{k_{cat}} \; ; \quad m_5$$

(**EQUATION 4.12; 4.13;**

4.14)

$$= \frac{1 + \dfrac{K_{m(b)}}{[B]}}{k_{cat}}$$

Each set of data was fitted again with **EQUATION 4.6** that gave two values for m_5; therefore, K_m for each substrate was expressed as a function of m_5 and k_{cat}. In the final step, each set of data was fitted with the following:

$$y = \frac{([E]_0 \cdot m_1)}{1 + \dfrac{m_5^A m_1}{[A]} + \dfrac{m_5^B m_1}{m_0}}$$

(**EQUATION 4.15**)

For each set of data, **EQUATION 4.15** gave two coincident values for m_1, thus giving the k_{cat} value of ABTS oxidation for FeMC6*a–AuNPs. Considering the two values of m_5, calculated in the previous step, and the k_{cat} value, the two K_m for H_2O_2 and ABTS were calculated.

4.5. **References**

- J. M. Abad, S. F. Mertens, M. Pita, V. M. Fernández, D. J. Schiffrin "Functionalization of Thioctic Acid–Capped Gold Nanoparticles for Specific Immobilization of Histidine–Tagged Proteins" J. Am. Chem. Soc. 127 (2005), 15, 5689–5694.

- P. Agarwal, C. R. Bertozzi "Site–Specific Antibody–Drug Conjugates: The Nexus of Bioorthogonal Chemistry, Protein Engineering, and Drug Development" Bioconjugate Chem. 26 (2015), 2, 176–192.

- G. K. Ahirwal, C. K. Mitra "Gold nanoparticles based sandwich electrochemical immunosensor" Biosens Bioelectron. 25 (2010), 9, 2016–2020.

- S. A. Ansari, Q. Husain "Potential Applications of Enzymes Immobilized on/in Nano Materials: A Review" Biotechnol. Adv. 30 (2012), 3, 512–523.

- D. Astruc, F. Lu, J. R. Aranzaes "Nanoparticles as Recyclable Catalysts: The Frontier between Homogeneous and Heterogeneous Catalysis" Angew. Chem. Int. Ed. 44 (2005), 48, 7852–7872.

- R. Aufaure, J. Hardouin, N. Millot, L. Motte, Y. Lalatonne, E. Guenin "Tetrazine Click Chemistry for the Modification of 1–Hydroxy–1, 1–Methylenebisphosphonic Acids: Towards Bio–Orthogonal Functionalization of Gold Nanoparticles" Chem. Eur. J. 22 (2016), 45, 16022–16027.

- V. T. Bhat, P. A. Duspara, S. Seo, N. S. B. A. Bakar, M. F. Greaney "Visible Light Promoted Thiol–Ene Reactions Using Titanium Dioxide" Chem. Commun. 51 (2015), 21, 4383–4385.

- M. L. Blackman, M. Royzen, J. M. Fox "Tetrazine Ligation: Fast Bioconjugation Based on Inverse–Electron–Demand Diels– Alder Reactivity" J. Am. Chem. Soc. 130 (2008), 41, 13518–13519.

- M. Buhl, B. Vonhören, B. J. Ravoo "Immobilization of Enzymes via Microcontact Printing and Thiol–Ene Click Chemistry" Bioconjug. Chem. 26 (2015), 6, 1017–1020.

- G. Caserta, M. Chino, V. Firpo, G. Zambrano, L. Leone, D. D'Alonzo, F. Nastri, O. Maglio, V. Pavone, A. Lombardi "Enhancement of Peroxidase

Activity in Artificial MimochromeVI Catalysts through Rational Design" ChemBioChem. 19 (2018), 17, 1823–1826.

- M. C. Daniel, D. Astruc "Gold Nanoparticles: Assembly, Supramolecular Chemistry, Quantum–Size–Related Properties, and Applications toward Biology, Catalysis, and Nanotechnology" Chem. Rev. 104 (2004), 104, 293–346.

- S. De Carlo, J. R. Harris "Negative staining and cryo–negative staining of macromolecules and viruses for TEM" Micron 42 (2011), 117–131.

- N. K. Devaraj "The Future of Bioorthogonal Chemistry" ACS Cent. Sci. 4 (2018), 8, 952–959.

- Di Felice, R.; Selloni, A. "Adsorption Modes of Cysteine on Au (111): Thiolate, Amino–Thiolate, Disulfide" J. Chem. Phys. 120 (2004), 10, 4906–4914.

- N. Elahi, M. Kamali, M. H. Baghersad "Recent Biomedical Applications of Gold Nanoparticles: A Review" Talanta 184 (2018), 537–556.

- C. Garcia–Galan, Á. Berenguer–Murcia, R. Fernandez–Lafuente, R. C. Rodrigues "Potential of Different Enzyme Immobilization Strategies to Improve Enzyme Performance" Adv. Synth. Catal. 353 (2011), 16, 2885–2904.

- S. K. Ghosh, S. Nath, S. Kundu, K. Esumi, T. Pal, "Solvent and Ligand Effects on the Localized Surface Plasmon Resonance (LSPR) of Gold Colloids" J. Phys. Chem. B 108 (2004), 37, 13963–13971.

- W. Haiss, N. T. K. Thanh, J. Aveyard, D. G. Fernig "Determination of Size and Concentration of Gold Nanoparticles from UV−Vis Spectra" Anal. Chem. 79 (2007), 11, 4215–4221.

- G. Han, P. Ghosh, V. M. Rotello "Functionalized Gold Nanoparticles for Drug Delivery" Nanomedicine 2 (2007), 1, 113–123.

- X. Han, J. Goebl, Z. Lu, Y. Yin, "Role of Salt in the Spontaneous Assembly of Charged Gold Nanoparticles in Ethanol" Langmuir 27 (2011), 9, 5282–5289.

- S. Horikoshi, N. Serpone "Introduction to Nanoparticles. Microwaves in Nanoparticle Synthesis" Wiley-VCH Verlag GmbH & Co. KGaA (2013), pp. 1–24.

- J. C. Jewett, C. R. Bertozzi "Cu–Free Click Cycloaddition Reactions in Chemical Biology" Chem. Soc. Rev. 39 (2010), 4, 1272–1279.

- J. Jia, B. Wang, A. Wu, G. Cheng, Z. Li, S. Dong, "A Method to Construct a Third–Generation Horseradish Peroxidase Biosensor: Self–Assembling Gold Nanoparticles to Three–Dimensional Sol−Gel Network" Anal. Chem. 74 (2002), 9, 2217–2223.

- A. G. Kanaras, F. S. Kamounah, K. Schaumburg, J. K. Kiely, M. Brust "Thioalkylated tetraethylene glycol: a new ligand for water soluble monolayer protected gold clusters" Chem. Commun. 20 (2002), 2294–2295.

- A. Khan, R. Rashid, G. Murtaza, A. Zahra "Gold Nanoparticles: Synthesis and Applications in Drug Delivery" Trop. J. Pharm. Res. 13(2014), 7, 1169–1177.

- J. Kim, H. Jia, P. Wang "Challenges in Biocatalysis for Enzyme–Based Biofuel Cells" Biotechnol. Adv. 2006, 24 (2006), 3, 296–308

- O. Kirk, T. V. Borchert, C. C. Fuglsang "Industrial Enzyme Applications" Curr. Opin. Biotechnol. 13 (2002), 4, 345–351.

- K. M. Koeller, C. H. Wong "Enzymes for Chemical Synthesis" Nature 409 (2001), 6817, 232–240.

- H. C. Kolb, M. G. Finn, K. B. Sharpless "Click Chemistry: Diverse Chemical Function from a Few Good Reactions" Angew. Chem. Int. Ed. 40 (2001), 11, 2004–2021.

- U. Kreibig, M. Vollmer "Optical Properties of Metal Clusters" pp 13–201 (1995), Springer, Berlin.

- A. Kuzmin, A. Poloukhtine, M. A. Wolfert, V. V. Popik "Surface Functionalization Using Catalyst–Free Azide−Alkyne Cycloaddition" Bioconjug. Chem. 21 (2010), 11, 2076–2085.

- J. P. Lata, L. Gao, C. Mukai, R. Cohen, J. L. Nelson, L. Anguish, S. Coonrod, A. J. Travis "Effects of nanoparticle size on multilayer formation and kinetics of tethered enzymes" Bioconjug. Chem. 26 (2015), 1931–1938.

- S. Link, M. A. El–Sayed "Size and Temperature Dependence of the Plasmon Absorption of Colloidal Gold Nanoparticles" J. Phys. Chem. B 103 (1999), 21, 4212–4217.

- S. Link, M. B. Mohamed, M. A. El–Sayed "Gold Nanorods: Electrochemical Synthesis and Optical Properties" J. Phys. Chem. B 104 (2000), 564–570.

- Y. Liu, C. Wang, N. Cai, S. Long, F. Yu "Negatively Charged Gold Nanoparticles as an Intrinsic Peroxidase Mimic and Their Applications in the Oxidation of Dopamine" J. Mater. Sci. 49 (2014), 20, 7143–7150.

- L. M. Liz–Marzán "Tailoring Surface Plasmons through the Morphology and Assembly of Metal Nanoparticles" Langmuir 22 (2006), 1, 32–41.

- M. Y. Lobanov, N. S. Bogatyreva, O. V. Galzitskaya "Radius of gyration as an indicator of protein structure compactness" Mol. Biol. 42 (2008), 623–628.

- D. Lu, G. Pang "A novel tetrahydrocannabinol electrochemical nano immunosensor based on horseradish peroxidase and double–layer gold nanoparticles" Molecules 21 (2016), 1377.

- S. K. Mamidyala, M. G. Finn, "In Situ Click Chemistry: Probing the Binding Landscapes of Biological Molecules" Chem. Soc. Rev. 39 (2010), 4, 1252–1261.

- M. J. Männel, L. P. Kreuzer, C. Goldhahn, J. Schubert, M. J. Hart, M. Chanana, "Catalytically active protein coatings: Toward enzymatic cascade reactions at the intercolloidal level" ACS Catal. 7 (2017), 1664–1672.

- H. Mattoussi, J. M. Mauro, E. R. Goldman, G. P. Anderson, V. C. Sundar, F. V. Mikulec, M. G. Bawendi "Self–assembly of CdSe–ZnS quantum dot bioconjugates using an engineered recombinant protein" J. Am. Chem. Soc. 122 (2000), 12142–12150.

- M. M. Miller, A. A. Lazarides "Sensitivity of Metal Nanoparticle Surface Plasmon Resonance to the Dielectric Environment" J. Phys. Chem. B 109(2005), 46, 21556–21565.

- J. E. Moses, A. D. Moorhouse "The Growing Applications of Click Chemistry. Chem. Soc. Rev. 36 (2007), 8, 1249–1262.

- P. Mulvaney "Surface Plasmon Spectroscopy of Nanosized Metal Particles" Langmuir 12 (1996), 788–800.

- J. S. Nanda, J. R. Lorsch "Labeling a protein with fluorophores using NHS ester

derivitization" Methods Enzymol. 536 (2014), 87–94.

- F. Nastri, L. Lista, P. Ringhieri, R. Vitale, M. Faiella, C. Andreozzi, P. Travascio, O. Maglio, A. Lombardi, V. Pavone "A Heme–peptide metalloenzyme mimetic with natural peroxidase–like activity" Chem. Eur. J. 17 (2011), 4444–4453.

- Y. Ni, Y. Li, Z. Huang, K. He, J. Zhuang, W. Yang "Improved activity of immobilized horseradish peroxidase on gold nanoparticles in the presence of bovine serum albumin" J. Nanopart. Res. 2013, 15 (2013), 2038–2046.

- J. M. Palomo "Click Reactions in Protein Chemistry: From the Preparation of Semisynthetic Enzymes to New Click Enzymes" Org. Biomol. Chem. 10 (2012), 47, 9309–9318.

- K. E. Peceros, X. Xu, S. R. Bulcock, M. B. Cortie, "Dipole−Dipole Plasmon Interactions in Gold–on–Polystyrene Composites" J. Phys. Chem. B 109(2005), 46, 21516–21520.

- S. Peng, J. M. McMahon, G. C. Schatz, S. K. Gray, Y. Sun, "Reversing the Size–Dependence of Surface Plasmon Resonances" Proc. Natl. Acad. Sci. 107 (2010), 33, 14530–14534.

- L. A. Porter, D. Ji, S. L. Westcott, M. Graupe, R. S. Czernuszewicz, N. J. Halas, T. R. Lee "Gold and Silver Nanoparticles Functionalized by the Adsorption of Dialkyl Disulfides" Langmuir, 14 (1998), 26, 7378–7386.

- V.V. Rostovtsev, L. G. Green, V. V. Fokin, K. B. Sharpless "A Stepwise Huisgen Cycloaddition Process: Copper (I)–Catalyzed Regioselective "Ligation" of Azides and Terminal Alkynes" Angew. Chem. Int. Ed. 41 (2002), 14, 2596–2599.

- C. I. Schilling, N. Jung, M. Biskup, U. Schepers, S. Bräse "Bioconjugation via Azide–Staudinger Ligation: An Overview" Chem. Soc. Rev. 40 (2011), 9, 4840–4871.

- G. Schmid "Large clusters and colloids. Metals in the embryonic state" Chem. Rev. 92 (1992), 1709–1727.

- E. M. Sletten, C. R. Bertozzi "Bioorthogonal Chemistry: Fishing for Selectivity in a Sea of Functionality" Angew. Chem. Int. Ed Engl. 48 (2009), 38, 6974–

6998.

- R. Srinivasan, L. P. Tan, H. Wu, P. Y. Yang, K. A. Kalesh, S. Q. Yao "High–throughput synthesis of azide libraries suitable for direct "click" chemistry and in situ screening" Org. Biomol. Chem. 7 (2009), 1821– 1828.

- S. Tadepalli, Z. Wang, J. Slocik, R. R. Naik, S. Singamanen "Effect of size and curvature on the enzyme   activity of bionanoconjugates" Nanoscale 9 (2017), 15666–15672.

- D. Tang, J. Tang, B. Su, Q. Li, G. Chen "Electrochemical detection of hepatitis C virus with signal amplification using BamHI endonuclease and horseradish peroxidase–encapsulated nanogold hollow spheres" Chem. Commun. 47 (2011), 9477–9479.

- A. C. Templeton, J. J. Pietron, R. W. Murray, P. Mulvaney "Solvent refractive index and core charge influences on the surface plasmon absorbance of alkanethiolate monolayer–protected gold clusters" J. Phys. Chem. B 104 (2000), 564–570.

- J. Turkevich, P. C. Stevenson, J. Hillier "A study of the nucleation and growth processes in the synthesis of   colloidal gold" Discuss. Faraday Soc. 11 (1951), 55–75.

- R. Vitale, L. Lista, C. Cerrone, G. Caserta, M. Chino, O. Maglio, F. Nastri, V. Pavone, A. Lombardi "An artificial heme–enzyme with enhanced catalytic activity: Evolution, functional screening and structural characterization" Org. Biomol. Chem. 13 (2015), 4859–4868.

- S. A. Walper, K. B. Turner, I. L. Medintz "Enzymatic Bioconjugation of Nanoparticles: Developing Specificity and Control" Curr. Opin. Biotechnol. 34 (2015), 232–241.

- G. Zambrano, E. Ruggiero, A. Malafronte, M. Chino, O. Maglio, V. Pavone, F. Nastri, A. Lombardi "Artificial Heme Enzymes for the Construction of Gold–Based Biomaterials" Int. J. Mol. Sci. 19 (2018), 10, 2896.

- J. Zdarta, A. S. Meyer, T. Jesionowski, M. A. Pinelo "General Overview of Support Materials for Enzyme Immobilization: Characteristics, Properties,

Practical Utility" Catalysts 8 (2018) 2, 92.

- S. Zeng, K. T. Yong, I. Roy, X. Q. Dinh, X. Yu, F. A. Luan "Review on Functionalized Gold Nanoparticles for Biosensing Applications" Plasmonics 6 (2011), 3, 491–506.

- M. X. Zhang, B. H. Huang, X. Y. Sun, D. W. Pang, "Clickable Gold Nanoparticles as the Building Block of Nanobioprobes" Langmuir 26 (2010), 12, 10171–10176.

Chapter 5

Conclusions

Chapter 5

The research project reported in this PhD thesis has been focused on the catalytic evaluation and applications of recently developed miniaturized enzyme, FeMC6*a. Previous investigations over the performances of this enzyme highlighted its higher catalytic efficiency in ABTS oxidation, compared to natural HRP. The enhanced performances within a miniaturized scaffold (3.5 kDa) have encouraged us to expand its action range and seek for practical applications.

As natural peroxidases, FeMC6*a demonstrated to be endowed with high versatility in catalysis, being able to catalyze different reactions in either freely diffusing or when immobilized on different surfaces.

FeMC6*a confirmed itself as top performing catalyst in oxidative dehalogenation reactions using 2,4,6–trichlorophenol as model substrate. By comparing the catalytic performances with those obtained for other natural and *de novo* or engineered peroxidases, FeMC6*a holds the best performances ever observed for 2,4,6–trichlorophenol conversion to 2,6–benzoquinone possessing 1500–fold and 20–fold higher catalytic efficiency based on 2,4,6–trichlorophenol, compared to HRP and F43Y/H64D myoglobin, respectively. Preliminary investigations over catalysis in the presence of humic acids showed that FeMC6*a is able to deplete 2,4,6–trichlorophenol from solution, paving the way for future applications in bioremediation.

Further efforts were devoted to the investigation over the electrochemical behavior of FeMC6*a when immobilized onto glassy carbon electrodes. FeMC6*a showed a non–reversible behavior, which was then confirmed as oxygen reduction reaction activity (ORR). Experiments in the presence of halogenated alcohols (such as 2,2,2–trifluoroethanol, 2,2,2–trichloroethanol and 1,1,1,3,3,3–hexafluoroisopropanol) showed that the ORR is strictly dependent on the addition of these solvents. By measuring the helix content (by means of θ_{222}) obtained in the presence of different halogenated and non–halogenated

solvents, a clear relationship between θ_{222} and peak currents appeared, strongly suggesting a direct effect of folding on the ORR activity. These results encouraged for the development of the first folding–activated sensor for halogenated alcohols based on a synthetic enzyme, able to operate also in complex solvent mixtures. The easy setup of the sensor allows for miniaturization and integration in compact devices for FeMC6*a practical on–field application in halogenated alcohols sensing.

Furthermore, the presence of a single free lysine residue in mimochrome scaffold allows for site–selective immobilization. In particular, FeMC6*a was efficiently immobilized onto gold nanoparticles. The immobilization was achieved by means of strain promoted alkyne–azide cycloaddition linkage which afforded functional nano–bioconjugates. The conformational analysis of the nano–bioconjugate demonstrated that FeMC6*a retains its helical structure upon immobilization and morphological analysis confirmed that the dispersity of gold nanoparticles was not harmed by the enzyme coating layer. Although the catalytic performances were influenced by immobilization, these results confirmed that mimochrome scaffold can be easily tethered on gold surfaces retaining part of the peroxidase activity.

The overall results show that FeMC6*a recapitulates the activity of natural peroxidases and resembles, or in some cases overcomes them, in performances and possible uses.

The present work confirms the feasibility of practical applications of synthetic heme protein models afforded by miniaturization in the fields of bioremediation, sensing and nanomaterials.

This page was intentionally left blank

Chapter 6

Supplementary materials

6.1 HPs oxidation: Total Turnover Number (TTN)

Along with the results reported in Chapter 2, the exceedingly high activity of FeMC6*a in TCP conversion has led us to explore its activity towards a large set of HPs, varying both in halogen and degree of substitution.

The reaction progress for the oxidation of different HPs was monitored by GC–MS analysis, using chlorobenzene as internal standard. The degree of conversion, based on substrate consumption, and the corresponding TTN measured after 30 minutes are reported in Table 6.1.

Table 6.1. Conversion (%) and TTN for different HPs measured after 30 minutes

Substrate	Conversion (%)	TTN
4–fluorophenol[a]	93	371
4–chlorophenol[a]	76	303
4–bromophenol[a]	66	266
4–iodophenol[a]	52	206
2–chlorophenol[a]	73	293
2,4–dichlorophenol[b]	>99	2590
2,4,6–trifluorophenol[b]	>99	3942
2,4,6–trichlorophenol[b]	>99	3960
pentafluorophenol[a]	46	185
pentachlorophenol[a]	36	142

In all cases, chlorobenzene was used as internal standard. [a] Reaction conditions: [FeMC6*a] = $6.25 \cdot 10^{-6}$ M; [HP] = 2.5 mM; [H_2O_2] = 2.5 mM; phosphate buffer (50 mM) at pH 6.5 with 50 %(v/v) TFE. [b] Reaction conditions: [FeMC6*a] = $6.25 \cdot 10^{-8}$ M; [HP] = 0.25 mM; [H_2O_2] = 0.25 mM; phosphate buffer (50 mM) at pH 6.5 with 50 %(v/v) TFE.

All HPs show promising TTN values, although lower for pentasubstituted phenols. Interestingly, the highest turnover numbers are observed for ortho and para– di– or tri– substituted phenols. This behavior can be rationalized either owing to different affinities of HPs versus the catalyst, or as a consequence of different electronic properties of the substrates. Particularly, the electron–donating effect by resonance (mesomeric effect) by ortho– and para–subtituted

halogen atoms contribute to the stabilization of the putative carbocationic intermediate (Species **(2)** from Chapter 2, Figure 2.4) formed along reaction. A negative effect is instead observed when halogen substitution is in meta–position, as in this case only a pure inductive effect by the halogen atoms occurs. Another possible explanation can rely in the difference in halogen and symmetry of the molecule, which might also affect the affinity of the substrate for the enzyme. Future efforts will be devoted to elucidate the differences in affinity of HPs towards FeMC6*a.

6.1.1 **Methods**

Reaction progress was monitored by GC–MS, using chlorobenzene as internal standard. At different times, an aliquot of the reaction mixture (100 μl) was diluted with an equal volume of H_2O 0.1%(v/v) TFA and extracted with dichloromethane (200 μl).

The degree of conversion at different reaction times was determined based on substrate consumption, using Equation 1:

$$Conversion\ (\%) = \frac{\left(\frac{A_{sub}}{A_{I.Std.}}\right)_0 - \left(\frac{A_{sub}}{A_{I.Std.}}\right)_x}{\left(\frac{A_{sub}}{A_{I.Std.}}\right)_0} \cdot 100\ \ (Equation\ 1)$$

where A_{sub} and $A_{I.Std.}$ are peak areas of the substrate and the internal standard, respectively, in the GC–MS TIC chromatogram. The subscript 0 indicates the trace acquired prior to addition of peroxide, while the subscript x is a specific time during reaction.

6.2 Synthesis of mimochrome@AuNPs nano–bioconjugate using a direct chemisorption approach

Along with the results reported in Chapter 4, the activity of mimochrome was investigated when immobilized onto AuNPs by direct chemisorption. The phases of this study are reported in figure 6.1. This section was adapted with permission from [Zambrano, G. et al. (2018)]

6.2.1 Synthesis of thiolated mimochrome

In this study, a previous analogue belonging to mimochrome family was used, MC6 S6G, which will be referred as MIMO. The sequence of MIMO is reported in figure 6.1.
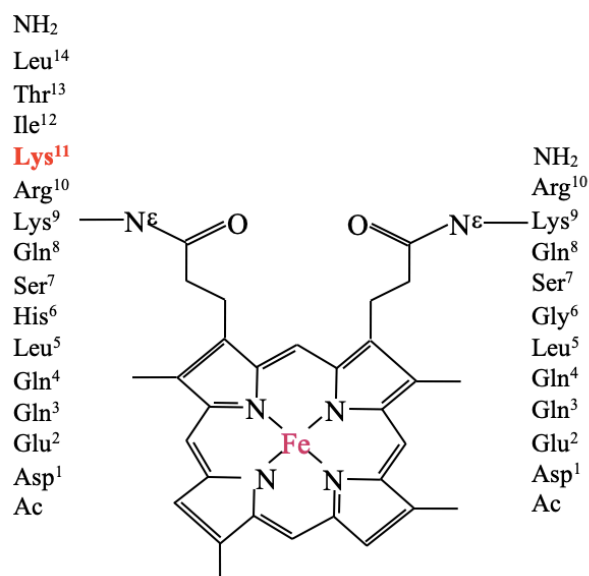
Figure 6.1. Schematic representation depicting MIMO chemical structure. The Lys11 residue conjugated to LA is highlighted in red. Adapted with permission from [Zambrano, G. et al. (2018)]

MIMO was synthesized analogously to FeMC6*a (reported in Chapter 1, paragraph 1.2), following a previously developed procedure [Nastri, F. et al. (2011); Vitale, R. et al. (2015)]. After metal insertion and purification using reverse phase–high performance liquid chromatography (RP–HPLC), it was conjugated to lipoic acid (LA) as reported in Figure 6.2.
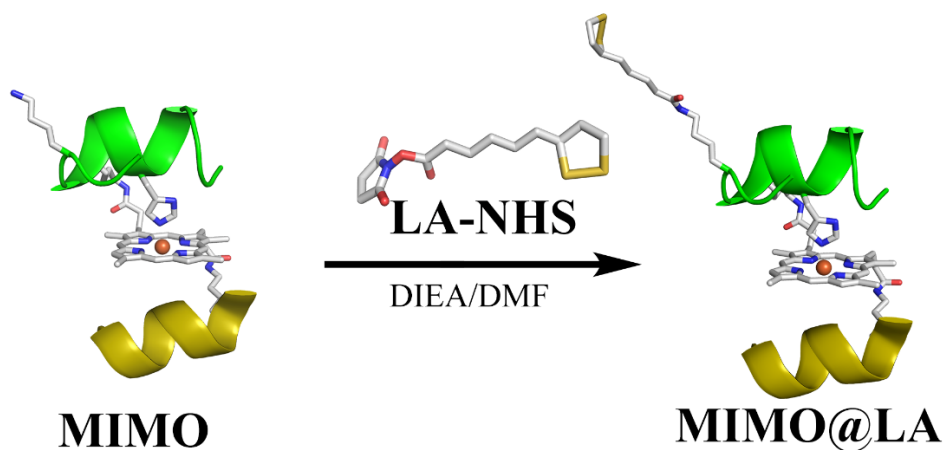
Figure 6.2. Synthesis of MIMO@LA

The presence of a single Lys residue (Lys 11 TD peptide) in one of the two peptide chains, exposed to the solvent, allows for site–selective conjugation of MIMO to activated carboxyl groups. To this aim, LA carboxylic group was activated as N–hydroxysuccinimidyl ester (LA–NHS) and coupled to MIMO via stable amide bond formation. The progress of reaction and identity of the product were ascertained by RP–HPLC and ESI–MS (Figure 6.3a-b).

(a)

(b)
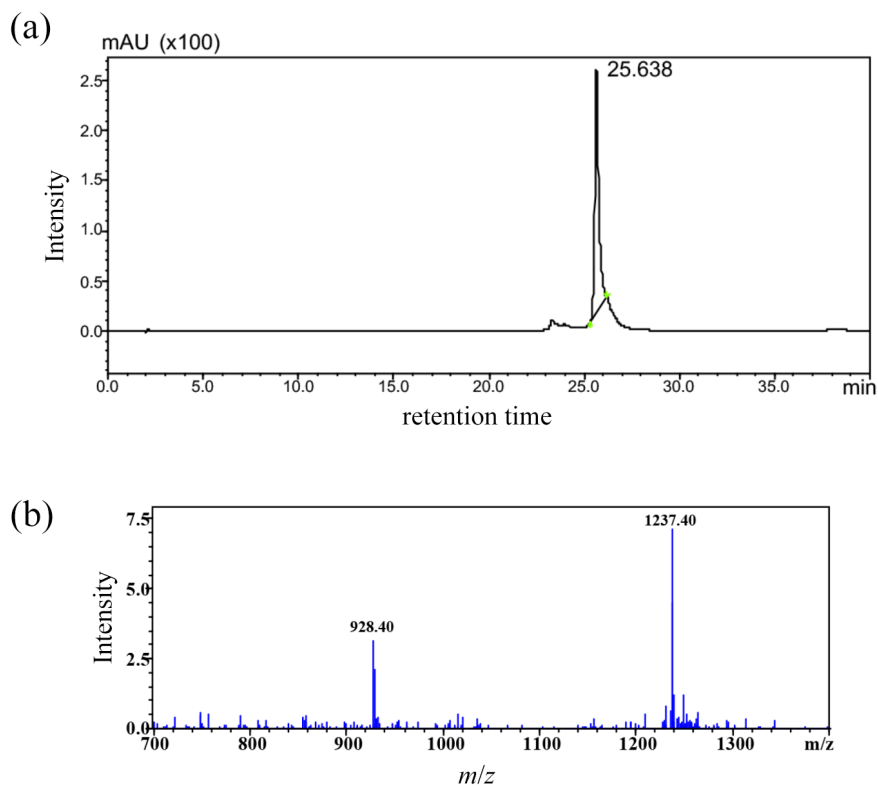
Figure 6.3. (a) LC–MS chromatogram of pure MIMO@LA. (b) ESI–MS spectrum of the peak at t_R=25.6 min.

The chromatographic profile confirms a nearly complete conversion of MIMO in MIMO@LA and mass analysis confirmed the formation of the desired product (experimental m/z $[M+3H]^{3+}$ 1237.4; $[M+4H]^{4+}$ 928.40 were consistent with the theoretical mass 3709.53 Da).

The reaction product was purified by RP–HPLC, thus yielding MIMO@LA (yield 34%).

6.2.2 **Synthesis of MIMO@LA@AuNPs**

Citrate stabilized AuNPs were prepared in situ accordingly to Turkevich method [Turkevich, J. et al. (1951)]. Briefly a 1 mM solution of tetrachloroauric acid ($HAuCl_4$) was brought to reflux and 10 minutes after vigorously boiling trisodium citrate (3.9 mM final concentration), was added to the mixture. Within 30 seconds from trisodium citrate addition, a color shift from pale yellow to a dark red was observed.

After cooling, citrate–stabilized AuNPs were functionalized with MIMO@LA and LA by ligand exchange reaction.

In order to avoid overcrowding of MIMO on the AuNPs surface, a mixture of LA and MIMO@LA in dimethylsulfoxide (DMSO) (with a 6:1 LA:MIMO@LA ratio) was added to AuNPs–citrate in water (pH 11). The mixture was left under vigorous stirring for three hours and purified by repeated cycles of centrifugation and resuspension in NaOH pH 11, until no catalytic activity was observed in the supernatants. To the resulting purified MIMO@LA@AuNPs, UV–Vis spectrum was acquired and compared to that acquired before ligand exchange reaction (Figure 6.4).
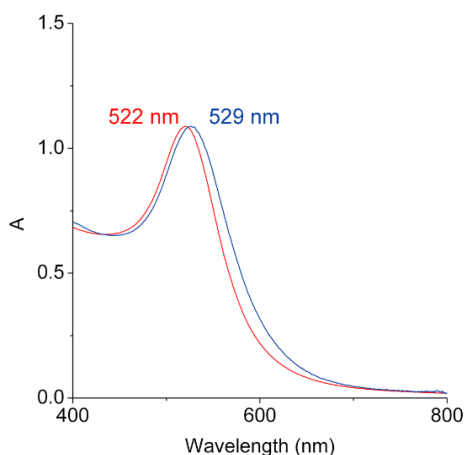
Figure 6.4. UV–Vis spectra before (red line) and after (blue line) LA:MIMO@LA addition

Figure 6.5 reports the superposition of the visible spectra of citrate–stabilized AuNPs (red line) and of the MIMO@LA@AuNPs bioconjugate (blue line). Citrate–stabilized AuNPs showed the characteristic Surface Plasmon Resonance (SPR) band with a maximum at 522 nm. The conjugation of MIMO@LA to AuNPs caused a red–shift of the SPRB from 522 to 529 nm without broadening of the band [Templeton, A.C. et al. (2000)], confirming that the MIMO coating layer did not alter the dispersity of AuNPs.

6.2.3 **TEM and ICP–MS analysis**

The morphology and size distribution of the nanoparticles were assessed by means of Transmission Electron Microscopy (TEM) analysis. The samples for TEM studies were prepared by evaporation of a drop of nanoparticle solution on carbon films supported on standard copper grids, and using a uranyl acetate staining solution [De Carlo, S. and Harris, J. R. (2011)].
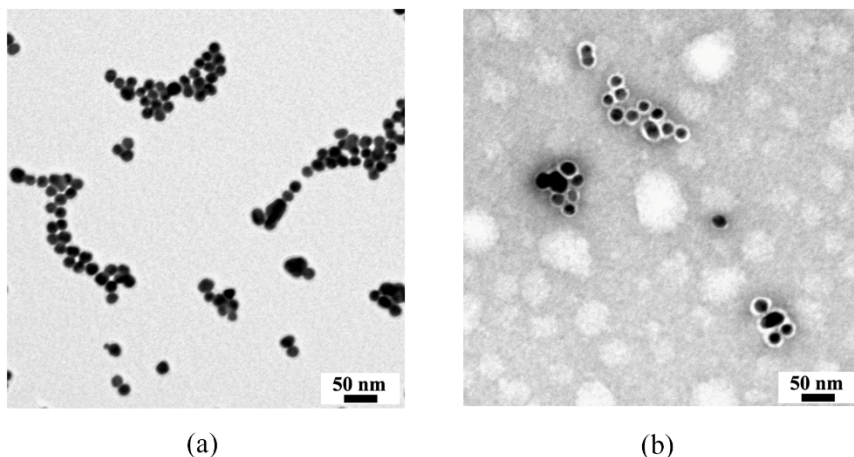
Figure 6.5. TEM images of (a) citrate stabilized AuNPs and (b) MIMO@LA@AuNPs

Figure 6.5 reports images acquired via Transmission Electron Microscopy (TEM) of citrate–stabilized AuNPs (Figure 6.5a) and MIMO@LA@AuNPs (Figure 6.5b).

The citrate– stabilized AuNPs appeared uniform in size and shape, with an average diameter of 16.0 ± 0.5 nm, as assessed by statistical analysis (data not shown). Figure 6.6b shows that, upon modification with MIMO@LA, the size of the AuNPs gold core is retained and that MIMO surrounds the gold surface as confirmed by the bright halo layer around the AuNPs [De Carlo, S. and Harris, J. R. (2011)]. An average diameter of 28.0 ± 0.5 nm was measured for the MIMO@LA@AuNPs conjugate, implying a protein shell thickness of 5.0 ± 0.5 nm.

The control over biomolecules loading is an essential feature in the development of an immobilization procedure, thus the degree of enzyme immobilization was prior assessed through the quantitative determination of iron content in the colloidal suspension. Quantification of the amount of

MIMO loaded per AuNP, was performed as described in Chapter 4, paragraph 4.2.2.6.

This allowed for the determination of the average number of MIMO@LA per AuNP. The concentration of MIMO from ICP–MS was determined as 10 µM, yielding a [MIMO]/[AuNPs] ratio of $\cong$1200 MIMO/AuNP.

6.2.4 Calculation of the maximum theoretical number (N_{max}) of MIMO/AuNP

The N_{max} of MIMO that can be loaded onto AuNP were calculated from Equation 2 as reported by [Mattoussi, H. et al. (2000)]:

$$N_{max} = 0.65 \times \frac{R_{complex}^3 - R_{AuNP}^3}{R_{protein}^3}; \quad (Equation\ 2)$$

where $R_{complex}$ is the AuNP–protein complex radius, R_{AuNP} (8 nm, as observed by TEM) is the gold nanoparticle radius including LA and Lys11 side chain (estimated as 2 nm in all–*trans* conformation), and $R_{protein}$ is the radius of the protein. The ratio is corrected by 0.65 as filling factor for hard sphere. $R_{complex}$ comprises the sum of R_{AuNP} and the diameter of the MIMO protein.

As observed in model structures MIMO molecule has a cylindrical shape, with dimensions of 1.6 nm in diameter and 2.6 nm in length, allowing for different orientation on AuNPs surface. Radius of gyration (R_G) was used to calculate an average diameter of MIMO, by taking into account all possible randomly oriented cylinder molecules with respect to the AuNP [Lobanov, M.Y. et al. (2008)]. R_G for MIMO was calculated (see section 4.4.13), and the value of $2 \times R_G$ (1.8 nm) was used for MIMO diameter in the calculation of $R_{complex}$.

This calculation afforded an N_{max} of $\cong 570$ MIMO/AuNP, which is nearly half of that measured by ICP–MS analysis ($\cong 1200$ MIMO/AuNP). Furthermore, the calculated MIMO diameter (1.8 nm) is almost half of protein shell thickness measured by TEM (5.0 ± 0.5 nm). Thus, these analyses suggest the formation of a MIMO double layer around each AuNP.

6.2.5 Catalytic characterization of MIMO@LA@AuNPs

A thorough catalytic characterization was performed onto MIMO@LA@AuNPs conjugate and the kinetic parameters of the enzyme in ABTS oxidation were determined by varying H_2O_2 concentration using fixed concentrations of ABTS and *vice versa*. The initial rates of ABTS oxidation (v_0) were plotted as a function of both substrate concentrations and fitted with a two substrate Michaelis–Menten equation (as reported in Section 4.4.12; Equation 4.6). Figure 6.6 shows that upon immobilization, the enzyme activity followed a typical Michaelis–Menten kinetics, as observed for the freely diffusing enzyme (Figure 6.7).
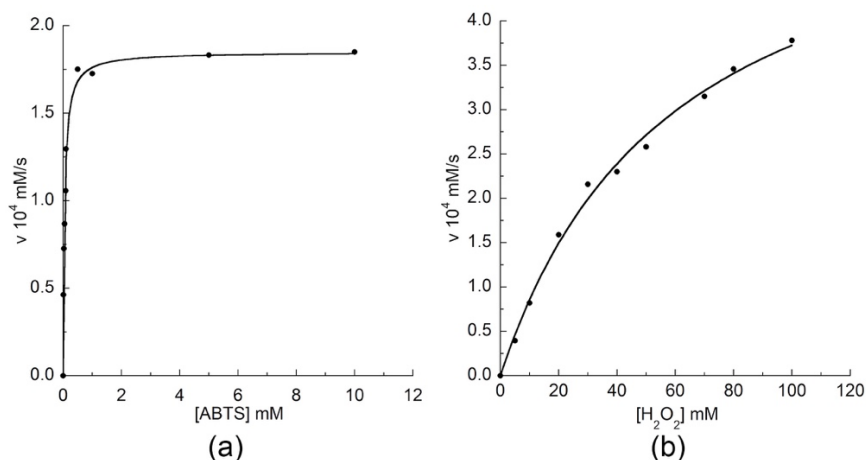
Figure 6.6. Two–substrate Michaelis–Menten plot obtained for MIMO@LA@AuNPs
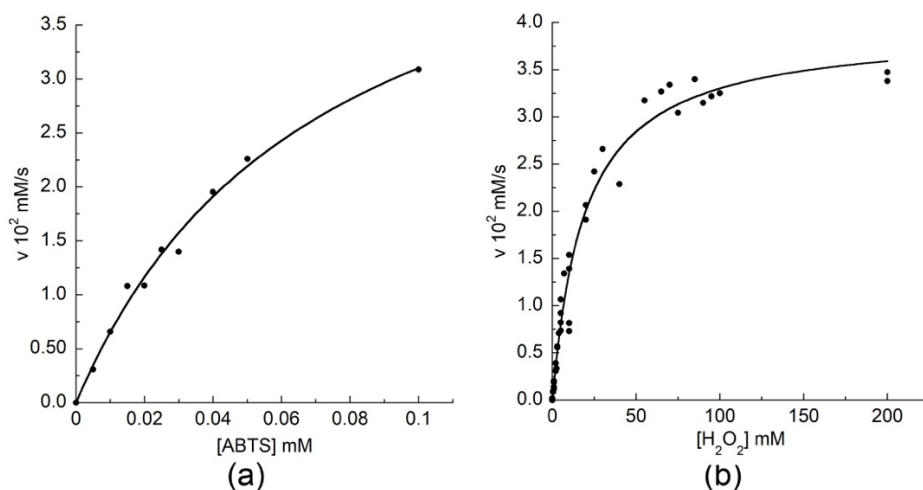
Figure 6.7. Two–substrate Michaelis–Menten plot obtained for freely diffusing MIMO

The kinetic parameters were then derived from the fitting and are shown in table 6.2.

Table 6.2 Comparison of kinetic parameters acquired for MIMO@LA@AuNPs and freely diffusing MIMO

Enzyme	K_m^{ABTS} $(10^{-5}$ M$)$	k_{cat} (s^{-1})	k_{cat}/K_m^{ABTS} $(mM^{-1}\,s^{-1})$
MIMO@LA@AuNPs	14.7 ± 0.1	1.7 ± 0.1	11.0 ± 0.7
MIMO	12 ± 2	468 ± 27	3743 ± 814

The analysis of the catalytic parameters confirms that peroxidase activity is retained upon immobilization, with only a small variation on the K_m^{ABTS} value. However, once grafted on AuNPs, MIMO performances are strongly influenced showing lower k_{cat} and k_{cat}/K_m^{ABTS} values.

This finding is not new, as reduced catalytic performances were also reported for other enzymes, such as HRP [Männel, M. J. et al. (2017); Ni, Y.

et al. (2013); Tadepalli, S. et al. (2017)]. Also, the enzyme multilayer can strongly affect the catalytic performances of the inner layers by the poor accessibility of substrates and/or by inhibition of enzyme conformational changes during catalysis due to steric hindrance [Lata, J. P. et al. (2015)].

To address this issue, a different batch of MIMO@LA@AuNPs was prepared and finally washed with NaOH pH 11 with 50 %(v/v) TFE in order to remove non–covalently bound MIMO from AuNPs surface. TFE shows remarkable solvation properties for MIMO, as confirmed by subsequent ICP–MS analysis, which gave a conjugation ratio of $\cong$470 MIMO/AuNP, close to the theoretical maximum of $\cong$570 MIMO/AuNP. The catalytic characterization was repeated on the TFE–washed MIMO@LA@AuNP and interestingly, performances were enhanced compared to those prepared without TFE washing step (Table 6.3).

Table 6.3 Kinetic parameters of TFE washed MIMO@LA@AuNPs compared to freely diffusing and non–washed MIMO@LA@AuNPs

Enzyme	K_m^{ABTS} $(10^{-5}$ M$)$	k_{cat} (s^{-1})	k_{cat}/K_m^{ABTS} $(mM^{-1}\,s^{-1})$
MIMO@LA@AuNPs	14.7 ± 0.1	1.7 ± 0.1	11 ± 0.7
MIMO@LA@AuNPs wash TFE	25.5 ± 6	15.2 ± 2	59.6 ± 20
MIMO	12.5 ± 2	468 ± 27	3743 ± 814

The TFE washing step positively impacted the k_{cat} value, as it is 10–fold increased compared to MIMO@LA@AuNPs without TFE washing and only 30–fold decreased compared to the freely diffusing MIMO. These data strongly suggest that multilayer formation negatively influences catalyst performances. Nevertheless, other factors inducing reduced catalytic performances should also be taken into account such as the AuNP diameter,

length of the linker and overcrowding on the AuNP surface, which might affect the catalyst active structure and limit diffusion of the substrates to the active site.

6.3 Methods

6.3.1 Synthesis of MIMO@LA

MIMO@LA was synthesized by adding lipoic acid activated as NHS ester to a solution of MIMO in anhydrous dimethylformammide (DMF), adjusted to pH $\cong 9$ with DIEA. More specifically, 15.0 mg of MIMO (3.88 μmol, 1.29 mM) were allowed to react with 10 equivalents (11.7 mg, 38.8 μmol, 12.9 mM) of N–hydroxysuccinimidyl lipoate in DMF (3.0 mL), in the presence of 4 equivalents of DIEA, for 16 hours. After completion, MIMO@LA was purified by RP–HPLC, and purity and the identity of the product was determined by RP–HPLC–ESI–MS. The chromatographic profile of the reaction product showed the presence of a main peak at retention time 25.6 min. ESI–MS mass analysis confirmed the identity of the desired MIMO@LA (experimental mass 3709.2 Da, theoretical mass 3709.53 Da), obtained with a 34.0% yield.

6.3.2 Synthesis of MIMO@LA@AuNPs

Conjugation of MIMO to AuNPs was obtained by direct chemisorption of MIMO@LA onto citrate–AuNPs following the procedure reported by [Onoda, A. et al. (2010)]. Prior addition of MIMO@LA, the pH of the stock citrate–AuNPs suspension was adjusted to 11 with the dropwise addition of 1 M NaOH. To 2.8 mL of this stock solution (AuNPs concentration $\cong 8$ nM), a mixture of MIMO@LA (0.600 mg, $1.62 \times 10{-}4$ mmol, in 400 μL) and LA (0.204 mg, $9.93 \times 10{-}4$ mmol, in 13.6 μL of 15 mg/mL solution) in DMSO (LA:MIMO@LA ratio 6:1) was added. The solution was incubated at room

temperature in the dark, and the proceeding of the reaction was followed by UV–Vis analysis, evaluating the shift in the SPR band upon MIMO@LA conjugation. After 3 h, the solution was centrifuged at 12,000 rpm for 25 min at 4°C. The excess MIMO@LA and lipoic acid was removed by centrifugation cycles, in which the supernatant was decanted and the remaining pellet was re–dispersed in fresh NaOH solution (pH 11). This procedure was repeated three times to obtain purified MIMO@LA@AuNPs. The pellet was then resuspended in NaOH solution (pH 11), and promptly used for subsequent experiments.

6.3.3 R_G calculation

The radius of gyration (R_G) for MIMO molecule was calculated on the model structure, by using the following equation:

$$R_G = \sqrt{\frac{1}{N} \sum_{i=1}^{N} (\vec{x_i} - \vec{x})^2}$$

where $x\, i$ is the position of the atom i in the model structure, x is the position of the centroid of the molecule, and N is the total number of non–hydrogen atoms. Calculation afforded a value of 9.03 Å (0.903 nm) for MIMO R_G value.

6.4 **References**

- S. De Carlo, J. R. Harris "Negative staining and cryo–negative staining of macromolecules and viruses for TEM" Micron 42 (2011), 117–131.

- J. P. Lata, L. Gao, C. Mukai, R. Cohen, J. L. Nelson, L. Anguish, S. Coonrod, A. J. Travis "Effects of nanoparticle size on multilayer formation and kinetics of tethered enzymes" Bioconjug. Chem. 26 (2015), 1931–1938.

- M. Y. Lobanov, N. S. Bogatyreva, O. V. Galzitskaya "Radius of gyration as an indicator of protein structure compactness" Mol. Biol. 42 (2008), 623–628.

- M. J. Männel, L. P. Kreuzer, C. Goldhahn, J. Schubert, M. J. Hart, M. Chanana, "Catalytically active protein coatings: Toward enzymatic cascade reactions at the intercolloidal level" ACS Catal. 7 (2017), 1664–1672.

- H. Mattoussi, J. M. Mauro, E. R. Goldman, G. P. Anderson, V. C. Sundar, F. V. Mikulec, M. G. Bawendi "Self–assembly of CdSe–ZnS quantum dot bioconjugates using an engineered recombinant protein" J. Am. Chem. Soc. 122 (2000), 12142–12150.

- F. Nastri, L. Lista, P. Ringhieri, R. Vitale, M. Faiella, C. Andreozzi, P. Travascio, O. Maglio, A. Lombardi, V. Pavone "A Heme–peptide metalloenzyme mimetic with natural peroxidase–like activity" Chem. Eur. J. 17 (2011), 4444–4453.

- Y. Ni, Y. Li, Z. Huang, K. He, J. Zhuang, W. Yang "Improved activity of immobilized horseradish peroxidase on gold nanoparticles in the presence of bovine serum albumin" J. Nanopart. Res. 2013, 15 (2013), 2038–2046.

- A. Onoda, Y. Ueya, T. Sakamoto, T. Uematsua, T. Hayashi "Supramolecular hemoproteins-gold nanoparticle conjugates" Chem. Commun. 46 (2010), 9107-9109.

- S. Tadepalli, Z. Wang, J. Slocik, R. R. Naik, S. Singamanen "Effect of size and curvature on the enzyme activity of bionanoconjugates" Nanoscale 9 (2017), 15666–15672.

- A. C. Templeton, J. J. Pietron, R. W. Murray, P. Mulvaney "Solvent refractive index and core charge influences on the surface plasmon absorbance of alkanethiolate monolayer–protected gold clusters" J. Phys. Chem. B 104 (2000), 564–570.

- J. Turkevich, P. C. Stevenson, J. Hillier "A study of the nucleation and growth

processes in the synthesis of colloidal gold" Discuss. Faraday Soc. 11 (1951), 55–75.

- Vitale, L. Lista, C. Cerrone, G. Caserta, M. Chino, O. Maglio, F. Nastri, V. Pavone, A. Lombardi "An artificial heme–enzyme with enhanced catalytic activity: Evolution, functional screening and structural characterization" Org. Biomol. Chem. 13 (2015), 4859–4868.